



HAL
open science

Development of novel diagnostic techniques to measure heat release rate perturbations in flames

Jingxuan Li

► **To cite this version:**

Jingxuan Li. Development of novel diagnostic techniques to measure heat release rate perturbations in flames. Other. Ecole Centrale Paris, 2012. English. NNT : 2012ECAP0012 . tel-00997413

HAL Id: tel-00997413

<https://theses.hal.science/tel-00997413>

Submitted on 28 May 2014

HAL is a multi-disciplinary open access archive for the deposit and dissemination of scientific research documents, whether they are published or not. The documents may come from teaching and research institutions in France or abroad, or from public or private research centers.

L'archive ouverte pluridisciplinaire **HAL**, est destinée au dépôt et à la diffusion de documents scientifiques de niveau recherche, publiés ou non, émanant des établissements d'enseignement et de recherche français ou étrangers, des laboratoires publics ou privés.



Ecole Centrale Paris

THESE

présentée par

Jingxuan LI

pour l'obtention du

GRADE de DOCTEUR

Formation doctorale : Energétique

Laboratoire d'accueil : Laboratoire d'Énergétique Moléculaire
et Macroscopique, Combustion (EM2C)
du CNRS et de l'ECP

Development of novel diagnostic techniques to measure heat release rate perturbations in flames

Soutenance le 30 Janvier 2012

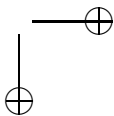
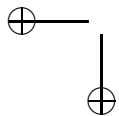
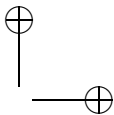
Composition du jury :

Mme	Baillet	F.	Rapporteur
	Mounaïm-Rousselle	C.	
MM.	Blanc-Benon	P.	Rapporteur
	Giuliani	F.	
	Richecoeur	F.	
	Schuller	T.	Directeur de thèse

Ecole Centrale des Arts et Manufactures
Grand Établissement sous tutelle
du Ministère de l'Éducation Nationale
Grande Voie des Vignes
92295 Châtenay-Malabry Cedex
Tél : 33 (1) 41 13 10 00
Télex : 634 991 F EC PARIS

**Laboratoire d'Énergétique
Moléculaire et Macroscopique,
Combustion (E.M2.C.)**
UPR 288, CNRS et Ecole Centrale Paris
Tél : 33 (1) 41 13 10 31
Fax : 33 (1) 47 02 80 35

2012ECAP00121



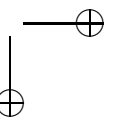
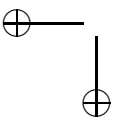
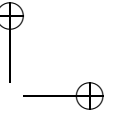
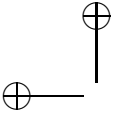
Résumé

Les fluctuations du taux de dégagement de chaleur sont souvent responsables d'intensification des flux thermiques aux parois, de vibrations et d'émissions sonores qui peuvent éventuellement dégénérer en instabilités thermo-acoustiques auto-entretenues. Ces phénomènes instationnaires dégradent les performances des foyers, provoquent un vieillissement prématuré de certains éléments de la chambre de combustion, voire des dégâts plus importants sur l'installation. Ces perturbations sont cependant difficiles à mesurer dans les foyers car il n'existe pas de diagnostic qui permette d'accéder directement au taux de dégagement de chaleur. L'objectif de ce travail est d'explorer deux alternatives aux solutions existantes pour accéder aux fluctuations du taux de dégagement de chaleur avec une bonne résolution temporelle. Ces nouvelles méthodes sont testées dans des configurations génériques parfaitement prémélangées pour des écoulements laminaires. La première méthode est une technique acoustique, qui repose sur la détermination du temps de vol d'ondes ultrasonores qui traversent l'écoulement. Les fluctuations du temps de vol de ces ondes sont utilisées pour détecter des perturbations de la largeur des gaz brûlés le long du chemin acoustique. Cette information permet de reconstituer les fluctuations du taux de dégagement de chaleur dans des flammes prémélangées. Les premières validations de cette méthode sont présentées pour des flammes en l'absence de perturbation externe lorsqu'elles présentent une instabilité de type Kelvin-Helmholtz pilotée par les phénomènes de flottabilité du panache des gaz brûlés. Des mesures sont ensuite conduites pour des flammes soumises à des modulations harmoniques de l'écoulement. Les données obtenues dans ces configurations sont comparées à des mesures optiques ainsi qu'à des prévisions analytiques. La seconde méthode est une technique optique utilisant un système d'interférométrie laser Doppler permettant de déterminer les fluctuations de densité intégrées le long du chemin optique. On montre dans un premier temps que les perturbations de densité sont principalement causées par des fluctuations du taux de dégagement de chaleur lorsque les flammes sont confinées. Un lien est établi pour reconstituer les perturbations du taux de dégagement de chaleur exploitant le signal de l'interféromètre. La technique est validée pour des flammes pulsées pour différentes richesses et débits. Les données obtenues sont comparées à des mesures reposant sur la chimiluminescence de la flamme. Un bon accord est obtenu

pour des modulations harmoniques de l'écoulement à différentes fréquences et niveaux de perturbation. Ce travail permet de valider le principe de ces deux techniques pour détecter les perturbations du taux de dégagement de chaleur lorsque l'accès optique à la zone de combustion est réduit et lorsque des informations quantitatives résolues temporellement sont nécessaires.

Abstract

Heat release rate disturbances are the sources of additional thermal stresses, direct and indirect combustion noise and undesirable vibrations. In extreme cases, these perturbations may even cause destructive combustion instabilities. These quantities are difficult to measure in practical burners. The objective of this work is to develop two alternative diagnostics to measure heat release rate fluctuations in unsteady flames. These techniques are validated in generic configurations for perfectly premixed laminar flames. The first method is an acoustic technique, which is based on the measurement of the travel time of ultrasonic waves through the flames. Fluctuations of the sound propagation time transmission through unsteady flames are used to estimate perturbations in the burned gases width along the acoustic path. This information is then used to reconstruct heat release rate fluctuations. This technique is validated in the cases of unstable laminar premixed flames driven by buoyancy forces and for flames submitted to harmonic flow velocity modulations. Analytical expressions are derived linking fluctuations in heat release rate and disturbances of the sound travel time. Measurements made with this acoustic technique are compared with optical detections based on the flame chemiluminescence and with predictions from an analytical model. Good agreements are obtained between these different methods validating the proposed technique. The second method envisaged is an optical technique based on a Laser Interferometric Vibrometer used to measure integrated density perturbations along the optical path of a laser beam. It is shown that density disturbances along this path result mainly from heat release rate fluctuations when the flames are confined. A link is established to reconstruct heat release rate disturbances from the signal of the interferometer. The technique is validated in the case of pulsated laminar premixed flames. Measurements are compared to line-of-sight integrated chemiluminescence emission measurements. A good agreement is obtained for harmonic flow modulations at different forcing frequencies and perturbation levels for flames operating at different flow conditions. This work validates the principle of this alternative technique for detecting heat release rate perturbations.



Contents

Résumé	iii
Abstract	v
Introduction	1
Motivation	1
Objective	5
Literature review	5
Thesis outline	11
I Acoustical diagnostic	15
1 Experimental setup	17
1.1 Experimental configuration	17
1.2 Characterization of the acoustic excitation	23
1.3 Characterization of the flame response to flow disturbances	26
1.4 Ultrasonic transducer and receiver	29
1.5 Conclusion	35
2 Principle of the acoustic method	37
2.1 Background	37
2.2 Model of sound travel time	38
2.3 Detection of sound travel time	42
2.4 Experimental detection system	49
2.5 Conclusion	56
3 Determination of heat release rate disturbances in the absence of external forcing	57
3.1 Theoretical analysis	57
3.2 Experimental configuration	60
3.3 Validation without flame	60
3.4 Validation with flame	62

viii	CONTENTS	
	3.5 Conclusion	68
4	Determination of heat release rate disturbances in pulsated flames	71
	4.1 Theoretical analysis	71
	4.2 Experimental configuration	77
	4.3 Experimental validation	78
	4.4 Conclusion	83
II	Optical diagnostic	87
5	Probing reacting flows with a Laser Interferometric Vibrometer	89
	5.1 Laser Interferometric Vibrometry	89
	5.2 Analysis without combustion	95
	5.3 Analysis with combustion	99
	5.4 Conclusion	106
6	Determination of flame front wrinkling	109
	6.1 Introduction	109
	6.2 Experimental configuration	111
	6.3 Processing of chemiluminescence images	114
	6.4 Results and discussion	119
	6.5 Conclusion	125
7	Determination of line-of-sight integrated heat release rate disturbances	127
	7.1 Introduction	127
	7.2 Experimental configuration	129
	7.3 Results and discussion	133
	7.4 Conclusion	143
	Conclusion	145
A	Examination of effects of ultrasonic waves on flames	149
	A.1 Experimental configuration	150
	A.2 Results and discussion	150
	A.3 Conclusion	154
	References	165

Nomenclature

Roman Symbols

A	Element area [m ²].
B	Chirp frequency bandwidth [Hz].
c	Speed of sound [m·s ⁻¹].
c^*	Equivalent speed of sound ($c^* = c_u c_b / (c_b - c_u)$) [m·s ⁻¹].
D	Diameter [m].
\mathcal{E}	Signal envelope [-].
E_r	Error coefficient [-].
f	Frequency [Hz].
f_i	Initial frequency of chirp signal [Hz].
f_m	Modulation frequency [Hz].
g	Gravitational acceleration [m·s ⁻²].
G	Gladstone-Dale coefficient [m ³ ·kg ⁻¹].
H	Height [m].
\mathcal{H}	Hilbert transform.
I	Light-emission intensity [V].
K	Calibration factor of mass flow rate controller [-].
L	Length [m].
L_f	Characteristic length of the burned gases [m].
\dot{m}	Mass flow rate [kg·s ⁻¹].
n	Refractive index [-].
p	Pressure [Pa].
P	Average power of the signal [-].
\dot{q}	Heat release rate per unit volume [W·m ⁻³].
Δq	Heat value per unit mass of mixture [J·kg ⁻¹].
$\langle \dot{q}' \rangle_L$	Line-of-sight integrated heat release rate perturbations [W·m ⁻²].
\dot{Q}	Heat release rate [W].
r_i	Local flame front radius [m].
r_o	Local position of the interface between burned gases and ambient air [m].
R	Radius [m].

x

NOMENCLATURE

R_{ti}	Cross-correlation between signals S_t and S_i .
S_L	Laminar burning velocity [$\text{m}\cdot\text{s}^{-1}$].
S_m	Chirp signal.
S_i	Incident signal.
S_t	Transmitted signal.
t	Time [s].
t_r	Repetition time of the chirp signal [s].
Δt	Sound travel time [s].
T	Temperature [K].
\mathcal{T}_r	Transfer function between heat release rate and sound travel time [-].
v	Velocity [$\text{m}\cdot\text{s}^{-1}$].
V	Volume [m^3].
\dot{V}	Volume flow rate [$\text{m}^3\cdot\text{s}^{-1}$].
W	Molecular weight [$\text{g}\cdot\text{mol}^{-1}$].

Greek Symbols

α	Half angle of flame cone [rad].
β	Amplitude of the chirp signal [-].
γ	Ratio of specific heat capacity [-].
Γ	Dimensionless flame parameter [-].
λ_0	Wavelength of the laser beam in the vacuum [m].
λ	Laser beam wavelength in the medium of refractive index n ($\lambda = \lambda_0/n$) [m].
μ	Slope of frequency modulation [$\text{Hz}\cdot\text{s}^{-1}$].
ν	Kinematic viscosity [$\text{m}^2\cdot\text{s}^{-1}$].
ξ	Volumetric expansion ratio ($\xi = T_b/T_u$) [-].
ϖ	Coefficient between L_f and V_b for fixed flow operating conditions and experimental arrangement [-].
ρ	Gas density [$\text{kg}\cdot\text{m}^{-3}$].
$\langle \rho' \rangle_L$	Integrated density perturbations along the geometrical path L [$\text{kg}\cdot\text{m}^{-2}$].
τ	Time duration of chirp signal [s].
ϕ	Equivalence ratio [-].
φ	Signal phase [rad].
ω	Angular frequency [$\text{rad}\cdot\text{s}^{-1}$].
ω^*	Reduced angular frequency [-].

NOMENCLATURE

xi

Superscript

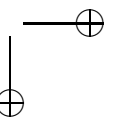
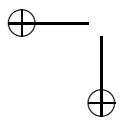
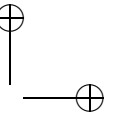
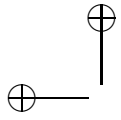
-	Mean component.
'	Fluctuating component.

Subscript

<i>b</i>	Burned gases.
<i>m</i>	Modulation.
<i>rms</i>	Root mean square value.
<i>u</i>	Unburned gases.

Abbreviation

<i>CCD</i>	Charged coupled device.
<i>ICCD</i>	Intensified charged coupled device.
<i>LIF</i>	Laser Induced Fluorescence.
<i>LIV</i>	Laser Interferometric Vibrometer (Vibrometry).
<i>M</i>	Microphone.
<i>PM</i>	Photomultiplier.
<i>PSD</i>	Power spectral density.
<i>SNR</i>	Signal to noise ratio [-].



Introduction

Motivation

The problem of determining unsteady heat release rate disturbances is considered experimentally and theoretically in this work. The development of techniques enabling measurements of heat release rate disturbances is an active field of investigation with several fundamental and technological applications such as improvement of knowledges on flame dynamics, combustion noise, combustion instabilities and turbulent combustion, or applications to combustion control to monitor the operating point of a system, reduce pollutant emissions and detect stability limits.

Heat release rate denotes the energy release per unit time during the chemical conversion of reactants to combustion products (Poinsot and Veynante 2005). The heat change associated with a chemical reaction depends on the initial and final thermodynamic states and the way combustion takes place. For an isobaric process, the net change in enthalpy is equal to the heat of reaction which is negative for exothermic process. The heating value is then a positive number equal to the enthalpy of combustion but with the opposite sign. There are many possible heating values for a fuel, depending on the phase of water formed in the products, the phase of the injected fuel, and the conditions under which combustion takes place (Kuo 2005). Since it is not a fundamental property of a fuel and cannot be calculated from the basic material properties, it is then generally defined by considering a chemical system of N species reacting through M reactions. For species k , the mass reaction rate $\dot{\omega}_k$ per unit volume corresponds to the sum of rates $\dot{\omega}_{kj}$ produced by the M reactions:

$$\dot{\omega}_k = \sum_{j=1}^M \dot{\omega}_{kj} \quad (1)$$

The volumetric heat release per unit time due to combustion \dot{q} is then given

by:

$$\dot{q} = - \sum_{k=1}^N \Delta h_{f,k}^0 \dot{\omega}_k \quad (2)$$

where $\Delta h_{f,k}^0$ denotes the enthalpy of formation per unit mass for each species k at the reference temperature T_0 , usually taken equal to the standard temperature $T_0 = 298.15$ K. The last expression is useful for thermo-chemical calculations (Kuo 2005) or numerical simulations (Poinsot and Veynante 2005) of multi-species reacting flow. For practical applications, it is however interesting to define this quantity by examining the fuel or oxidant consumption rates. One common method known as oxygen consumption calorimetry (Janssens 1991) is based on the assumption that many gases, liquids, and solids release a constant amount of energy for each unit mass of consumed oxygen (Iqbal and Salley 2004). On another hand, the energy cost is directly proportional to the fuel consumption rate. It is then often useful to work with the heating value ($-\Delta h_f^0$), i.e. the heat released by the combustion of one kilogram of fuel. Therefore, the fuel mass consumption rate $\dot{\omega}_f$ or the fuel mass burning rate are often used to estimate the heat release rate:

$$\dot{Q} = \int_V \Delta h_f^0 \dot{\omega}_f dV \quad (3)$$

In premixed systems, it is also possible to define a consumption speed S_c associated to the combustion wave. The heat release rate is then given by (Lefebvre and Ballal 2010):

$$\dot{Q} = \int Y_f \rho_u S_c \Delta h_f^0 dA \quad (4)$$

where Y_f , ρ_u and A denote the fuel mass fraction and flame surface area. Any disturbances in the four components may cause heat release rate disturbances.

Flow perturbations in the fresh reactants region may originate from disturbances of the fuel and air injection supplies (Hathout et al. 2000; Lieuwen 2001) or may result from intrinsic flow instabilities like for example those associated with precessing vortices of swirled stabilized flows (Selle et al. 2006; Stöhr et al. 2011). These mechanisms are sensitive to pressure changes. For example, pressure perturbations at the burner inlet may generate a differential response of the fuel or air supply resulting in flow rate or mixture composition perturbations. Pressure oscillations may also synchronize naturally disorganized unstable flows as shown for modulated shear layers (Crow and Champagne 1971) and generate large coherent structures (Poinsot et al. 1987; Yu et al. 1991). Acoustic disturbances contribute directly and indirectly to the formation of flame wrinkles that are convected along the flame front and modify the flame surface area due to an unbalance between the local flame consumption speed and flow velocity (Baillot et al. 1992; Ducruix et al. 2000;

Lieuwen and Yang 2005). Perturbations at the flame anchoring point are also convected along the flame front and produce additional wrinkles (Petersen and Emmons 1961; Kornilov et al. 2007). Including effects of turbulence, there are thus many sources of heat release rate disturbances in a reacting flow.

Monitoring and controlling heat release rate disturbances is an important issue in practical combustion chambers because these perturbations are the sources of unsteady thermal stress, direct and indirect combustion noise when entropy waves are accelerated by the mean flow (Candel et al. 2009). They may promote self-sustained thermoacoustic instabilities causing potential severe damages and early aging of components of the combustion chamber (Candel 2002; Lieuwen and Yang 2005). These three aspects are described below separately.

Combustion noise

It was in the early 1960s, following the successful introduction of jet engine into commercial airline service, that noise became an issue in the conceptual and detailed design of aircrafts (Smith 2004). Jet noise, being the main contribution to the engine noise, efforts have mainly focused in the last 50 years on this component. Important progress has been achieved with the introduction of large bypass flow (Gabriel 2006), and further reduction can be achieved with special devices at the outlet of nozzle, for example “chevron nozzle” (see for example Callender et al. (2005)), to enhance the mixing of the jet flow with surrounding air. Focus has then been turned to control sources of noise generated in the

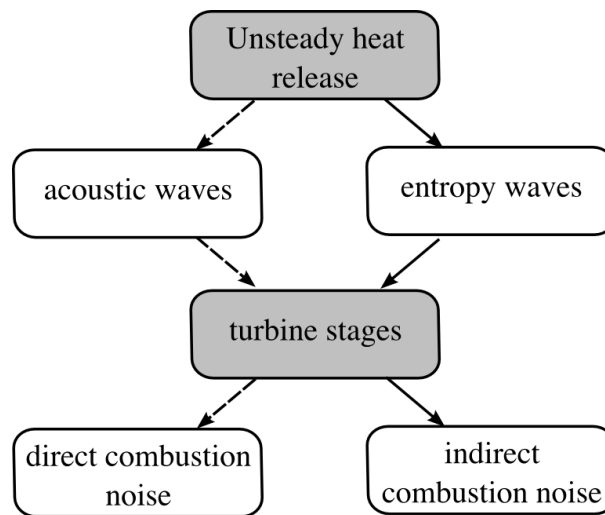


Figure 1 : Schematic of the two main mechanisms for combustion noise generation in jet engines: dashed lines indicate the chain of direct noise, solid lines indicate the chain of indirect noise. Adapted from Leyko et al. (2009).

combustion chamber when other noise sources became a concern. Heat release rate perturbations produce sound waves by two different mechanisms leading to combustion noise emission (Mahan and Karchemer 1991; Candel et al. 2009). This is schematically illustrated in Fig. 1:

- (i) Direct combustion noise arises when an unsteady volume of gas expands at a constant pressure as it gets energy from the combustion. The resulting unsteady expansion of the surrounding gas produces a sound wave that propagates outside of the boundary of the flame. The heat release rate is the only contribution to this mechanism and determines the intensity and frequency of the sound produced (Bragg 1963). The radiated sound power covers a broad spectrum of frequencies from around 100 to 2000 Hz, reaching a blunt peak between 300 and 500 Hz (Strahle 1978). Sound waves propagate downstream or upstream through the turbo stages and can reach the far field after distortion by the mean flow, diffraction and reflection by the solid walls with the diffuser, distributor, turbine or compressor blades (Leyko et al. 2009).
- (ii) Indirect combustion noise is mainly produced by the unsteady flow of the hot combustion products accelerated through the turbine and exhaust nozzle. Entropy waves generated during the combustion, propagate downstream and interact with the accelerating mean flow constituting additional noise sources (Marble and Candel 1977; Howe 1998). Resulting acoustic waves propagate to the far field through the turbine stages in the similar way as for direct combustion noise.

Combustion instability

Turbulent flames generate sound waves with a broad frequency bandwidth (Mahan and Karchemer 1991). These acoustic waves propagate inside the combustion chamber, are reflected by the walls, interact with the combustion chamber boundaries and return back to the combustion zone with a time delay that depends on the size of the combustion chamber, disturbances of speed of sound and impedances at the boundaries of the combustion chamber. These pressure oscillations generate in turn perturbations of the flow field by modifying the local flowrate, reactant compositions or thermodynamics properties in the flame region producing heat release rate disturbances (Candel 2002; Ducruix et al. 2003). When these disturbances are synchronized, they amplify leading to an increase of acoustic energy in the system and a resonance is generally observed at specific tones. This feedback loop is described in Fig. 2. These self-sustained instabilities are generally not desirable because they may lead to an early aging of combustion chamber or in extreme cases to severe structural damages.

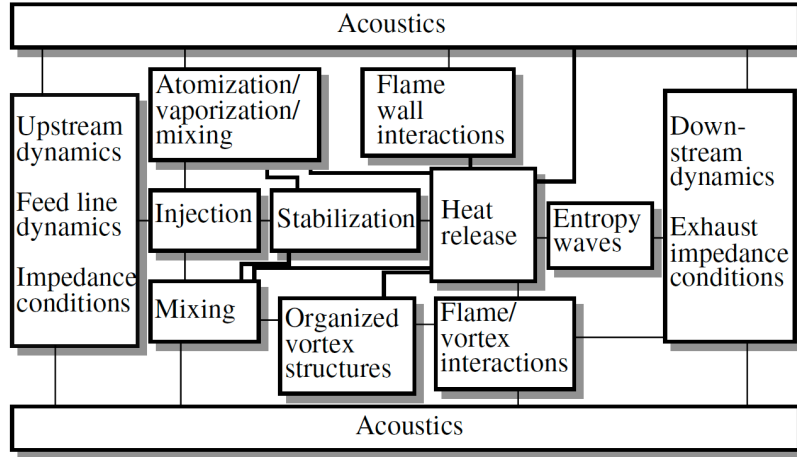


Figure 2 : *Basic interactions leading to combustion instabilities. Adapted from Candel (2002).*

Thermal fatigue

The walls of the combustion chamber are generally very close to the flame region. These components reach high temperatures although they are generally cooled by small perforations with a colder bias flow (Kiameh 2002). During self-sustained instabilities, the periodic motion of the flame may cause a periodic heat transfer between the hot products and some components of the chamber leading to an additional thermal stress (Lieuwen and Yang 2005; Lefebvre and Ballal 2010). These repeated cycles generate thermal fatigue which may reduce the life of the system. The periodic oscillation of the hot flow at the combustion chamber outlet impinging on the turbine blades may also be responsible of thermal fatigue (Boyce et al. 2006).

Objective

As described above, disturbances in heat release rate may be significant in the combustion chamber and are generally undesirable. It is therefore important to control these disturbances and have reliable tools to estimate their contribution to the total heat release rate. The objective of this work is to develop two new diagnostics to measure heat release rate fluctuations in perturbed flames. The first one is an acoustic technique, which is based on the measurement of the travel time of ultrasonic waves crossing through unsteady flames. Fluctuations of the sound propagation time is used to estimate perturbations in the burned gases width along the acoustic path. This information is then used to reconstruct heat release rate fluctuations. The second method is an opti-

cal technique based on a Laser Interferometric Vibrometer used to measure integrated density perturbations along the optical path of a laser beam. It is shown that these disturbances result mainly from heat release rate fluctuations. These new alternative techniques complete the set of diagnostics already available to estimate heat release rate disturbances which are briefly reviewed below.

Literature review

Techniques based on chemiluminescence emission and Laser Induced Fluorescence (LIF) are first reviewed, followed by a discussion on the use of ultrasonic waves to probe flows and the interaction between acoustic waves and flames. Finally, the use of Laser Interferometric Vibrometry is briefly examined.

Chemiluminescence

A widely used technique to estimate heat release rate is to collect the chemiluminescence emission from the flame. Chemiluminescence from hydrocarbon flames results from naturally excited intermediate radicals, such as OH^* , CH^* or C_2^* , formed within the flame front and emitting a photon during the transition to a lower energy state. These radicals are often considered as good markers of heat release rate (Gaydon 1957). Recording the natural emission from the flame is the simplest technique yielding time-resolved information and is often used to estimate perturbations in heat release rate by collecting the total emission from the flame (see for example Hurle et al. (1968), Price et al. (1969), Ducruix et al. (2000)) or by local point measurements (Kojima et al. 2000; Hardalupas and Orain 2004). This has for example been validated in the case of laminar premixed flames submitted to flow modulations in the absence of mixture composition inhomogeneities, where fluctuations in the chemiluminescence emission intensity were shown to be proportional to flame surface area disturbances (Schuller et al. 2002b). Spectral selection of OH^* or CH^* emissions is generally preferred for hydrocarbon flames but it is also possible to use other chemiluminescent species, such as C_2^* or CO_2^* (Samaniengo et al. 1995; Najm et al. 1998; Docquier et al. 2000). In more complex configurations, different additional phenomena modify this relation and effects of the turbulence intensity, flame strain rate, flame front curvature, local mixture composition, temperature and pressure must be included to obtain quantitative estimates of the heat release rate (Docquier et al. 2000; Higgins et al. 2001; Ikeda et al. 2002; Hardalupas and Orain 2004; Ayoola et al. 2006; Nori and Seitzman 2009; Lauer and Sattelmayer 2010). Measurements are then often limited to flame images for qualitative analysis except in a few studies where the signal is calibrated using specific post-processing procedures (see for example Palies et al.

(2010), Lauer et al. (2011)). One problem is that the chemiluminescence emission yields an information integrated in the line-of-sight and it is difficult to obtain spatially resolved data. The signal is also more difficult to interpret in non perfectly premixed systems (Balachandran et al. 2005b; Kim et al. 2010).

Laser Induced Fluorescence

One possibility to improve spatial resolution is to use Laser Induced Fluorescence (LIF) by stimulating certain electronic transitions from the radicals present in the flow with a laser sheet intersecting the flame front. OH LIF is widely used since the OH peak mole fraction occurs in the burned gases just behind the reaction zone and the gradients of the fluorescence signal are found to correlate well with the position of the local flame front in turbulent flames (see for example Knikker et al. (2002), Sadanandan et al. (2008)). The CH fluorescence signal is a better tracer of the reaction zone due to its relatively short lifetime and its abundance over a narrow region in the flame zone (Nguyen and Paul 1996; Donbar et al. 2000), even though large deviations with heat release rate were highlighted for diluted flames during transient phenomena (Vagelopoulos and Frank 2005). Time resolved data are more difficult to obtain due to the limited repetition rates and energy delivered per pulse from the lasers, although OH and CH planar measurements at a few kHz were recently reported to characterize transient phenomena in complex turbulent reacting flows (see for example Tanahashi et al. (2008), Boxx et al. (2009), Stöhr et al. (2011)). While these techniques enable to locate the flame front, quantitative estimates of spatially resolved data for the heat release rate are still challenging. It is generally admitted that the intermediate radical HCO correlates well with heat release rate but the stimulation of an electronic transition with a detectable fluorescence signal raises several difficulties (Jeffries et al. 1991). The concentration of HCO can however be estimated by the product of the OH and CH₂O radical concentrations formed around the flame, whose fluorescences are easier to obtain. This has motivated a series of studies based on LIF measurements at different excitation wavelengths to estimate the local distribution of heat release rate in flow configurations of increasing complexity (Najm et al. 1998; Paul and Najm 1998; Fayoux et al. 2005; Balachandran et al. 2005a; Ayoola et al. 2006). This type of simultaneous measurements in unsteady flows remain however heavy to implement and require high power well-tuned laser beams at different wavelengths and specific optics.

Other optical alternatives

An alternative is based on the link between heat release rate fluctuations \dot{q}' and density perturbations ρ' in unsteady flames (Candel et al. 2009):

$$\frac{\partial \rho'}{\partial t} = -\frac{\gamma - 1}{\bar{c}^2} \dot{q}' \quad (5)$$

where \bar{c} represents the local speed of sound and γ denotes the specific heat capacities ratio. This link will be detailed in chapter 7. It indicates an indirect access to the heat release rate perturbations by the knowledge of density. Density fluctuations can for example be probed by the spectroscopic techniques. Raman Scattering (Kojima and Nguyen 2005) and Coherent Anti-Stokes Raman Spectroscopy (CARS) (Magre and Bouchardy 2000) can provide precise and spatially resolved data. These two methods are based on the inelastic scattering of light and are however limited to the time resolved measurement because the intensity of the inelastic scattered light is too weak (Fouad 2011). Rayleigh Scattering is another possibility. This technique is based on elastic scattering of light by particles or molecules with a diameter much smaller than the wavelength of the light (Miles et al. 2001; Rausch et al. 2011). The scattered energy is proportional to the number density of the measured gas. This technique is influenced by the unwanted light from the Mie scattering by particles and the background noise due to laser light scattered by solid surface (Ötügen 1997). Interferometry is a very sensitive technique and provides line-of-sight integrated density fluctuations along the optical path of the light. This technique is used in this work to estimate heat release rate fluctuations and will be described later in this chapter.

Acoustic techniques

Flames submitted to acoustic disturbances behave as low-pass filters and are only sensitive to the velocity component of sound waves (Ducruix et al. 2003). Low frequency pressure disturbances are transmitted through a flame without distortion. The cut-off frequency of the flame response is reached when the velocity perturbation wavelength is of the order of the flame length $\lambda \sim L$, which is typically limited to about 2 kHz for most typical applications. In the intermediate range of frequencies, sound waves are scattered by the strong jump in density across the flame (Cho 2009) and by turbulent wrinkles which develop along the flame for frequencies ranging from about 1 to 20 kHz. The incoherent scattered sound power first increases exponentially with frequency and then saturates to a certain level when compared to the coherent sound power incident on the flame (Lieuwen et al. 2002). When the wavelength is of the order of the flame thickness, pressure perturbations may then strongly interact with the preheat zone $\lambda \sim \delta$ and consequently modify the local reaction rate (Peters and Ludford 1983; McIntosh 1991; Ledder and Kapila 1991). This occurs only

at very high frequencies of about 100 kHz for typical hydrocarbon-air flames, except when flames are submitted to high accelerations at very high forcing levels (Durox et al. 1997a; Durox et al. 1998; Baillot et al. 1999; Wangher et al. 2008).

Acoustic waves propagating through, or scattered by, a turbulent flow carry structural information about the flow inhomogeneities and turbulence. To take advantage of this property, Chernov (1960) describes acoustic wave propagation in a randomly inhomogeneous medium with the ray theory. This theory is valid for acoustic wavelengths λ much smaller than the characteristic dimension l of the medium: $\lambda \ll l$ and for a linear propagation distance L satisfying $\sqrt{\lambda L} \ll l$. Those conditions are usually satisfied for laboratory scale experiments using ultrasonic waves. For larger propagation distances, the diffraction theory has to be considered. Investigations have been conducted to characterize inhomogeneous flows either by evaluating the travel time variations of an acoustic wave through the medium or by establishing correlations between acoustic waves and turbulence (see for example Blanc-Benon et al. (1991), Iooss et al. (2000)). The transit time can be used to measure flow rates based on the apparent difference of speed of sound in the flow direction and in the opposite direction (Radkevich et al. 1987). Effect of turbulence may cause uncertainties that were numerically examined by Iooss et al. (2002). Similar sensor configurations were also used to probe grid-generated turbulence in wind tunnels (Andreeva and Durgin 2004; Andreeva and Durgin 2011). A link between fluctuations of the

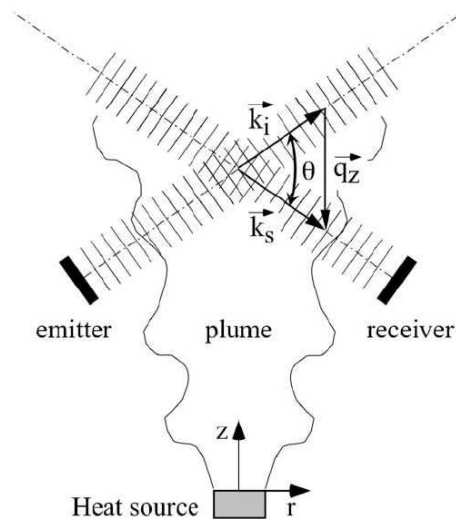


Figure 3 : Hot plume probed by ultrasonic waves. Adapted from Elicer-Cortes et al. (2006).

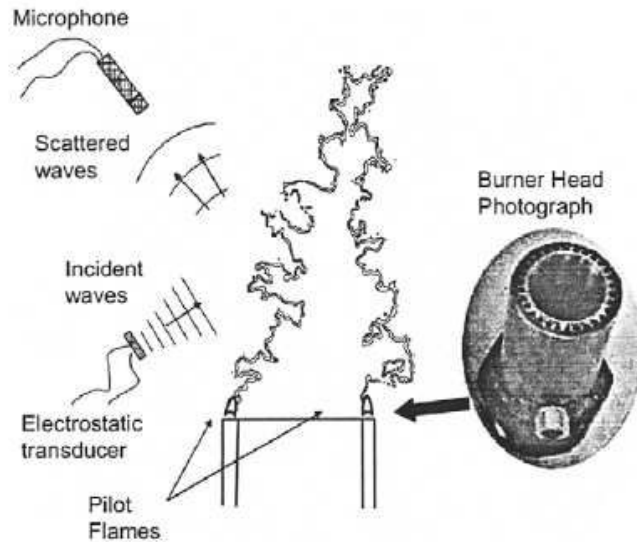


Figure 4 : *Turbulent flame probed by ultrasonic waves. Adapted from Lieuwen et al. (2002).*

speed of sound and turbulent velocity perturbations can be constructed based on spatial correlations of the propagation times in the turbulent flow. Static information on turbulence can then be obtained based on these measurements.

The information carried by the scattered field of ultrasonic waves impinging a flow was already used to analyze vorticity production in turbulent jets and swirling jets (Baerg and Schwarz 1966; Fabrikant 1983; Oljaca et al. 1998; Poulain et al. 2004) as well as to detect temperature fluctuations in inert turbulent flows (Contreras and Lund 1990; Elicer-Cortes et al. 2004; Elicer-Cortes et al. 2006). In the case of reacting flows, these investigations were limited yet to the examination of the scattered sound field by the flame as a function of the geometric properties of the reaction front and the characteristics of turbulence (Lieuwen et al. 2002). Examples of these configurations are shown in Figs. 3 and 4. It is shown in these references that density perturbations and flame front wrinkles induced by turbulence result in Doppler shifted scattered waves, the coherent scattered signal being significantly damped compared to the incident coherent ultrasonic pressure disturbances. For confined flames, influence of turbulent on the acoustic modes of a rocket model combustor was also highlighted by Richecoeur et al. (2009).

Another possibility to easily obtain time resolved information in flows featuring large density modifications, such as reacting flows, is to use optical interferom-

eters.

Laser Interferometric Vibrometry

A light beam propagating through a medium with inhomogeneous properties experiences some distortion due to the change of refractive index along the optical path (Shakher and Nirala 1999). The refractive index being a function of flow density, this yields a way to estimate density disturbances integrated along the optical path. Two phenomena can be exploited. Identification of changes in an observation plane due to the deflection of light is the principle used by shadowgraph and schlieren techniques (Settles 2001). Identification of changes in the phase of light beams with different optical paths is used to develop interferometers (Menkirch 1981).

The principle of interferometry can be explained using the Mach-Zehnder interferometer presented in Fig. 5. A parallel light beam is divided into two beams by a beam splitter. The first beam, named the object beam, passes through a beam splitter and the probed flow, is reflected by the mirror at the top, is reflected by the bottom beam splitter and is recorded by a detector. The second beam, considered as the reference beam, is reflected by the beam splitter at the top and then by the bottom, passes through the bottom beam splitter, is combined with the object beam and is recorded by the same detector. The phase difference between these two beams is obtained by the interferogram between the two light beams at the position of the detector. This technique is often used in reacting flows to estimate the temperature distribution (Qi et al.

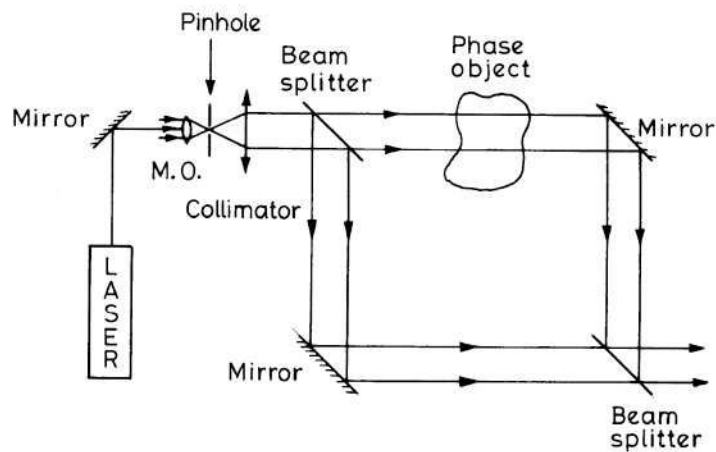


Figure 5 : Schematic of Mach-Zehnder interferometry. Adapted from Shakher and Nirala (1999).

2008; Ahmadi et al. 2011). Holography images can also be exploited (Xiao et al. 2000; Zhang and Zhou 2007).

A Laser Interferometric Vibrometer (LIV) corresponds to a compact design of the principle shown in Fig. 5 except that the object beam is not reflected by a mirror but by a vibrating surface. The resulting vibration of the interferogram pattern at the detector location is therefore proportional to the displacement of the object being investigated. This technique is widely used to analyze surface vibration (Graebner et al. 2000; Kokkonen and Kaivola 2008; Schott 2010) until recently some researchers used it to visualize the sound field produced in the vicinity of music instruments (Olsson and Tatar 2006; Gren et al. 2006). This technique has also been envisaged to determine density and density fluctuations in turbulent non reacting flows (Mayrhofer and Woisetschläger 2001; Woisetschläger et al. 2003; Hampel and Woisetschläger 2006; Köberl et al. 2010) as well as in perturbed reacting flows (Giuliani et al. 2007; Giuliani et al. 2010b). However, this technique has not been successfully used yet to determine heat release rate perturbations in unsteady flames.

Thesis outline

The manuscript is organized in two parts. The first one including chapters 1 to 4 is concerned with the description and validation of the acoustic diagnostic to measure heat release rate perturbations.

The experimental setup used in this work is presented in chapter 1. A cylindrical burner fed by a methane-air mixture enable to stabilize laminar conical premixed flames which are submitted to flow perturbations to generate heat release rate disturbances. A hot-wire is placed at the burner outlet to control the flow velocity perturbations. The methods used to image the flames and characterize their motion and response to flow perturbation are then described. This comprises a Photodiode (PM), a Charged Coupled Device (CCD) camera, an Intensified Charged Coupled Device (ICCD) camera and a color Schlieren system. The material for the acoustic characterization is described at the end of this chapter. The main elements are an ultrasonic wave emitter or a tweeter and two microphones for the generation and measurements of sound travel times.

The acoustic method developed to infer heat release rate disturbances is described in chapter 2. This technique examines the transmission of ultrasonic waves and considers disturbances in the sound travel time $\Delta t'$ between an emitter and a receiver as an indicator of perturbations in the burned gases width. To detect small differences in the sound travel time, a pulsed compression tech-

nique with a linear frequency modulation associated with a matching filter are used. The generation and post-processing of these signals are described in this chapter. Effects of main parameters on the precision of this detection technique are examined theoretically and experimentally. Performances in non reacting and reacting flow are then examined in chapters 3 and 4.

In chapter 3, laminar premixed conical flames featuring a “flickering” instability at the flame tip are investigated. This “flickering” phenomenon produces small heat release perturbations with typical frequencies around 10 to 20 Hz at ground level gravity and provides a generic configuration to validate the acoustic method for heat release rate reconstruction in the absence of external forcing device. A theoretical link between the rate of change of the sound travel time $d\Delta t/dt$ of ultrasonic waves crossing the flame and heat release rate fluctuations \dot{Q}' is established. Experimental results are compared to theoretical estimates and measurements obtained with an optical technique based on the chemiluminescence emission.

The flames investigated in chapter 4 are partially confined by a quartz tube placed on the top to eliminate buoyancy effects, and are submitted to upstream flow velocity modulations. A new link between resulting heat release rate fluctuations \dot{Q}' and the corresponding perturbations in the propagation time of ultrasonic waves $\Delta t'$ is established in these configurations. This link takes the form of a transfer function which depends on the flow operating conditions, flame aspect ratio and frequency. Results deduced from acoustic measurements are compared to theoretical estimates and data obtained with an optical technique.

The second part of this manuscript including chapters 5 to 7 is devoted to the use of a Laser Interferometric Vibrometer to measure disturbances in the flame front motion and heat release rate perturbations for flames submitted to harmonic flow modulations.

In chapter 5, the Laser Interferometric Vibrometer (LIV) used in this study is briefly described. This technique is then used to detect sound waves produced at the burner outlet in the absence of combustion. Density fluctuations in a hot jet and pulsated flames are then also examined.

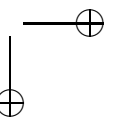
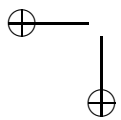
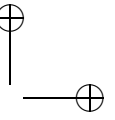
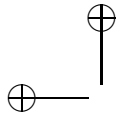
LIV is used to detect flame front wrinkles in chapter 6. Disturbances in the flame front position are shown to be proportional to line-of-sight integrated density perturbations when density disturbances in the burned gases and fresh mixture can be neglected. Validations are conducted on laminar premixed conical flames submitted to flow velocity modulations at different working condi-

tions. Results deduced with LIV are compared with flame front measurements obtained from chemiluminescence images of the flame motion.

In chapter 7, it is shown that density perturbations along the optical path passing through confined flames are mainly due to heat release rate disturbances. This property enables to use LIV to estimate integrated heat release rate disturbances in the line-of-sight. Predictions are validated in the case of pulsated laminar premixed flames at different working conditions. Measurements are compared to line-of-sight integrated chemiluminescence emission data collected with a CCD camera.

Part I

Acoustical diagnostic



Chapter 1

Experimental setup

A cylindrical burner fed by a methane-air mixture is used to produce laminar conical premixed flames which are submitted to flow perturbations to generate heat release rate disturbances. The experimental setup and burner are first described. The second part of this chapter is devoted to the diagnostics used to estimate heat release rate disturbances. Measurements of the flow velocity with a hot-wire are presented in section 1.2. The methods used to image the flames and characterize their motions are described in section 1.3. This comprises a Photodiode (PM), a Charged Coupled Device (CCD) camera, an Intensified Charged Coupled Device (ICCD) camera and a color Schlieren system. Finally, the material for the acoustic characterization is described at the end of the chapter. The main elements are an ultrasonic wave emitter or a tweeter and two microphones for the measurements of sound travel time. The response of these different components is also described.

1.1 Experimental configuration

A global schematic of the system used to generate the flow is presented in Fig. 1.1. Methane and air supplied from external high pressure tanks are mixed in the premixer to feed the burner. The convergent exit of the burner enables to produce a uniform flow profile and to stabilize premixed conical flames anchored on the burner rim. Mass flow controllers located on the air and combustible feeding lines enable to control the mass flow rate. A loudspeaker fixed at the base of the burner is used to modulate the flow velocity at the burner exit and to perturb the shape of the flame. The different components of the experimental setup are detailed separately below.

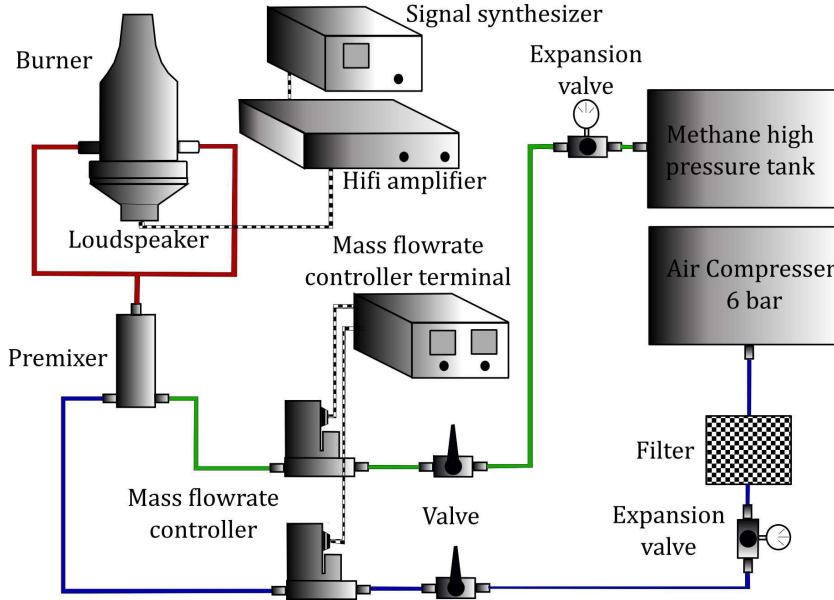


Figure 1.1 : Schematic of the experimental setup. The solid line indicates the fuel supply chain and the lines with stripes denote the different electrical connections.

1.1.1 Burner

The different flows investigated in this work are produced by a cylindrical burner detailed in Fig. 1.2. The burner is $H = 235$ mm in height and comprises two sections:

- (i) The upper part of the burner enables to stabilize laminar conical flames with a radius $R_o = 10$ mm. A unit with a convergent shape enables to produce a flat mean velocity profile at the burner exit. The shape of this unit is defined by the equation:

$$\frac{R(H)}{R_i} = \left[1 - \frac{\left[1 - \left(\frac{R_i}{R_o} \right)^2 \right] \left[1 - \left(\frac{H_c - H}{H_c} \right)^2 \right]^2}{\left[1 + \frac{(H_c - H)^2}{3H^2} \right]^3} \right]^{-\frac{1}{2}} \quad (1.1)$$

where $R_i = 32$ mm is the unit inlet radius and $H_c = 58$ mm the height of this unit. The evolution of the burner radius is plotted in Fig. 1.3. The flow at the burner exit was characterized by Laser Doppler Anemometry (LDA) by Duchaine (2010). For one typical operating regime considered in this work corresponding to a flow velocity $\bar{v}_u = 1.6$ m·s⁻¹ at the burner exit, the profile of the axial velocity component is plotted in Fig. 1.4 as a function of the radial distance with respect to the burner axis. The velocity profile is flat and uniform except in the boundary layer near the burner edges.

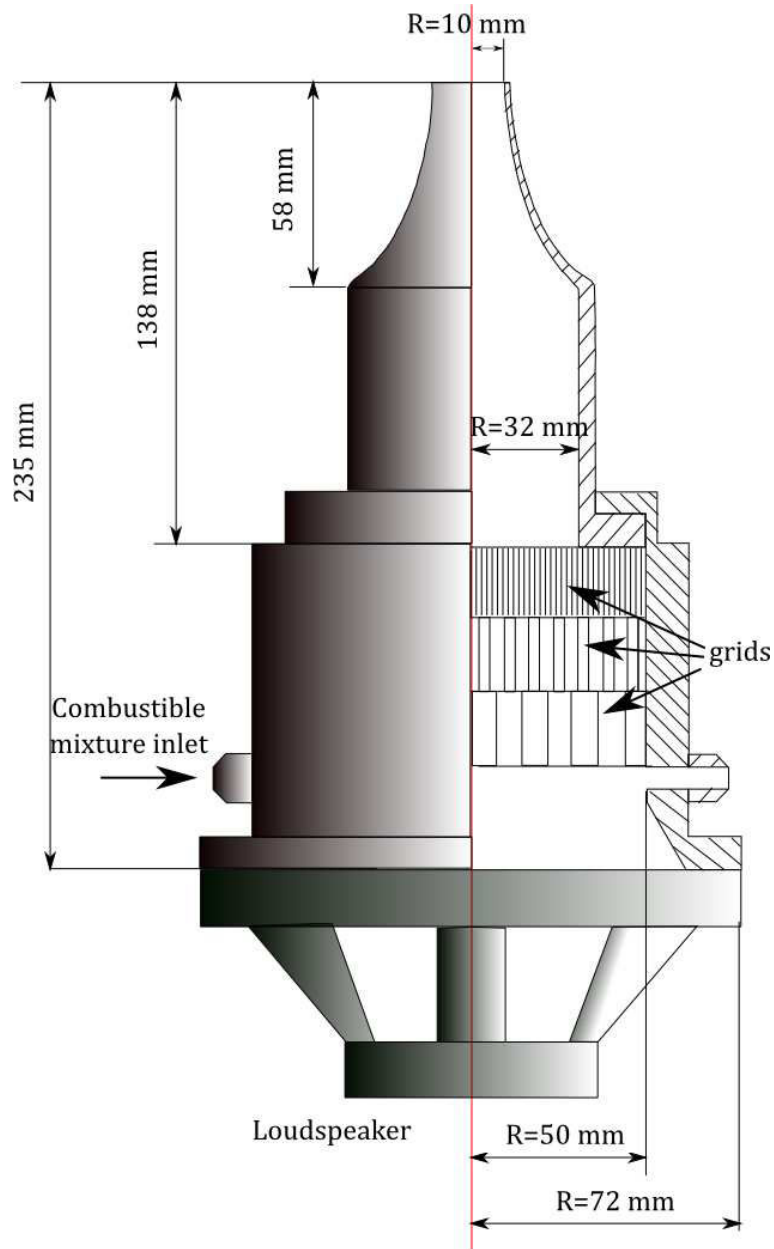


Figure 1.2 : Schematic of the burner.

- (ii) The bottom part of the burner features a cylindrical piece with a larger inner radius $R_b = 50$ mm used to reorganize the flow from the feeding pipes supplying the combustible mixture and to support the upper part of the burner. Three grids with different hole sizes are set in the burner to break the largest flow structures, parallelize the flow in the vertical

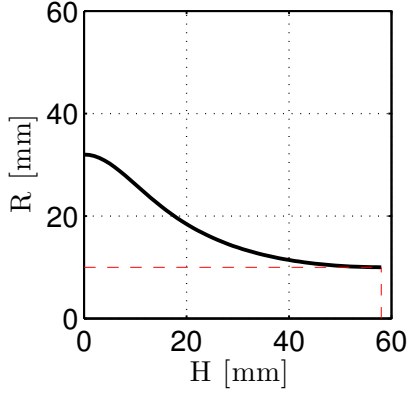


Figure 1.3 : Evolution of the radius of the convergent unit of the burner with the height.

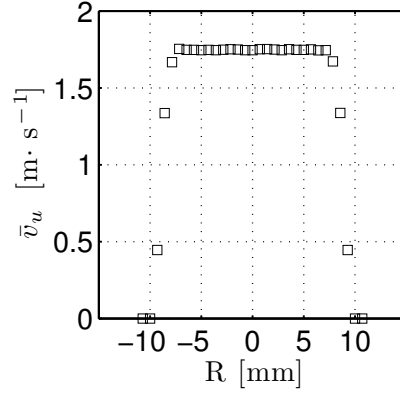


Figure 1.4 : Profile of axial velocity of the steady flow measured by LDA at height $z = 3.5$ mm above the burner outlet.

direction with a honeycomb structure, and dissipate the smallest disturbances with a refined grid. The bottom part of the burner is equipped with a loudspeaker to modulate the flow.

1.1.2 Fuel supply and control system

A methane-air mixture serves as combustible in all experiments presented in this work. Air is supplied from the laboratory network at a fixed pressure of 6 bar. Methane is stocked in high pressure tanks regulated at 5 bar by two successive expansions. Two valves located on the air and methane feeding pipes enable to open and close the fluids supply. Two mass flow rate controllers regulate the flow rate of air and methane. The mass flow rate in each line is given by:

$$\dot{m} = \rho(T_0, p_0) \frac{K}{K_{ref}} \dot{V}_{ref}(T_0, p_0) \quad (1.2)$$

where $\rho(T_0, p_0)$ is the density of the gas at the normal conditions $T_0 = 273.15$ K, $p_0 = 101325$ Pa, $\dot{V}_{ref}(T_0, p_0)$ denotes the volume flow rate of the reference gas for which the system was calibrated and K/K_{ref} indicates a calibration factor given by the mass flow controller manufacturer at the normal conditions. The parameters for the two mass flow rate controllers are listed in the table 1.1.

In normal thermodynamic conditions, there is no reaction between air and methane. Therefore, the volume of the mixture is the summation of the volume

Table 1.1 : Parameters of the two mass flow rate controllers, the subscript ($_{max}$) corresponds to the maximum operating condition of the mass flow rate controller.

Operating gas	$\rho(T_0, p_0)$ [kg·m ⁻³]	$\dot{V}_{ref,max}(T_0, p_0)$ [NL·h ⁻¹]	K/K_{ref} [-]
air	1.275	4000	1.001
CH ₄	0.717	300	0.754

of the two components. The flow velocity at the burner exit is given by:

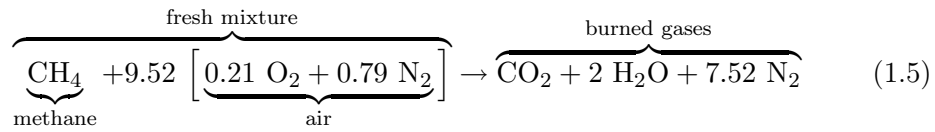
$$\begin{aligned}
 v_{u,c} &= \frac{\dot{V}_{air} + \dot{V}_{CH_4}}{\pi R_o^2} \\
 &= \frac{1}{\pi R_o^2} \frac{p_0 T_a}{p_a T_0} \left[\frac{K_{air}}{K_{ref,air}} \dot{V}_{ref,air}(T_0, p_0) + \frac{K_{CH_4}}{K_{ref,CH_4}} \dot{V}_{ref,CH_4}(T_0, p_0) \right] \quad (1.3)
 \end{aligned}$$

where the subscript ($_a$) indicates ambient conditions (T_a, p_a) and the subscript ($_o$) denotes the normal conditions (T_0, p_0).

The equivalence ratio of the combustible mixture is given by:

$$\phi = \frac{\alpha}{\alpha_s} \quad (1.4)$$

where $\alpha = \dot{m}_{CH_4}/\dot{m}_{air}$ is the fuel-air ratio which is equal to α_s for a stoichiometric mixture. This quantity can be obtained from the reaction equation (1.5):



For a stoichiometric methane-air mixture, one obtains:

$$\alpha_s = \frac{W_{CH_4}}{W_{air}} \times \frac{1}{9.52} = 0.058 \quad (1.6)$$

where $W_{CH_4} = 16 \text{ g}\cdot\text{mol}^{-1}$ and $W_{air} = 29 \text{ g}\cdot\text{mol}^{-1}$ are the molecular weight of methane and air.

Therefore, the equivalence ratio of the methane-air mixture supplied in the burner is given by:

$$\phi = 9.52 \frac{\dot{V}_{CH_4}}{\dot{V}_{air}} = 9.52 \frac{K_{CH_4}}{K_{ref,CH_4}} \frac{K_{ref,air}}{K_{air}} \frac{\dot{V}_{ref,CH_4}(T_0, p_0)}{\dot{V}_{ref,air}(T_0, p_0)} \quad (1.7)$$

Table 1.2 : *Flow modulation system characteristics.*

Equipment	Manufacturer	Type	Characteristics
Wave generator	Thurlbry Thandar instruments	TGA 1242	Frequency range: 0.1 mHz - 16 MHz Frequency resolution: 0.1 mHz
Hifi amplifier	JCB	XPP 7000	Maximum power: 245 W/ 8 ohms
Loudspeaker	Swanspeaker	M5N	Impedance: 8 ohms Maximum power: 70 W Frequency response: 5 Hz - 5 kHz Sensitivity: 87 dB·W ⁻¹
Analog to digital converter	National Instruments	BNC 2090 PCI-MIO-16E-4	2 outputs Output scanning rate: 500k Samples/s Maximum output voltage: 5 V

The flow rate can be adjusted from the terminal of the flow rate controllers, with an accuracy of 2% of the full scale, to reproduce the conditions needed for the experiments at a certain flow velocity and equivalence ratio. The two streams after the mass flow rate controllers are then mixed in a long chamber placed far from the burner.

1.1.3 Flow modulation system

The loudspeaker placed at the base of the burner generates an acoustic excitation to modulate the flow velocity at the burner outlet. The loudspeaker is powered by a Hifi amplifier driven by a wave synthesizer or a LABVIEW program. The digital signal from the LABVIEW program is converted to an analog signal by an analog to digital (A/D) converter integrated in the computer. Using this actuation chain, it is possible to modulate the flame over a wide range of frequencies and amplitudes.

Figure 1.5 shows the harmonic signal generated by the synthesizer and the corresponding velocity signal v_u at the burner outlet measured by a hot-wire when the flow is modulated at 50 Hz. The figure on the left shows that the flow velocity induced by the acoustic excitation describes a pure harmonic waveform like the forcing signal from the wave generator. This is also confirmed in the right figure by the power spectra of the signals featuring a unique peak at 50 Hz.

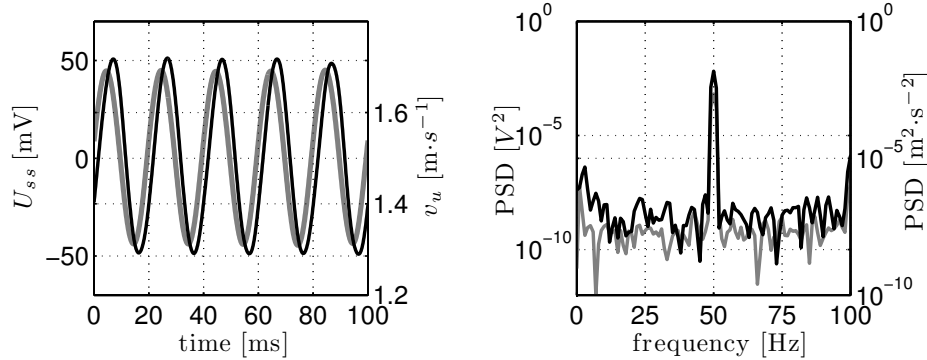


Figure 1.5 : Example of harmonic signal generated by the signal synthesizer U_{ss} (black solid line) and the velocity v_u (gray solid line) measured by the hot-wire anemometer at the exit of the burner (left figure). Power spectra of these two signals (right figure). Modulation frequency $f = 50$ Hz.

1.2 Characterization of the acoustic excitation

The acoustic excitation induced by the loudspeaker fixed at the base of the burner is monitored by a hot-wire anemometer. Laser Doppler Anemometry is generally preferred in this configuration because it does not disturb the flow and has been used to control the flow velocity in many similar experiments (Bourehla and Bailot 1998; Ducruix et al. 2000; Birbaud et al. 2006; Duchaine 2010). In this work, a hot-wire anemometer with a tiny wire located at the center of the burner outlet is used to control the velocity perturbations imposed to the flow. This technique was for example also used by other groups (Sugimoto and Matsui 1982; Kornilov 2006). The shortage is that the holder has a thickness of a few millimeters and introduces flow perturbations downstream the probe that may modify the measurements. However, the signal is only used as a reference to fix the modulation level for the different operating conditions explored.

The probe consists of a tungsten wire of about $10 \mu\text{m}$ which is located close to the exit of the burner and is well aligned with the axis of the burner. The cut-off frequency of the anemometer is about 7 kHz which is at least one order of magnitude larger than the largest acoustic excitation frequency examined in this work. Therefore, this system is well suited to measure relatively low frequency velocity perturbations generated by the loudspeaker.

1.2.1 Calibration

The link between the voltage output from the hot-wire anemometer E_a and the measured axial velocity v_u can be expressed using King’s law:

$$v_u^n = C_1 E_a + C_0 \quad (1.8)$$

where $n = 0.405$ is prescribed by the manufacturer (DANTEC Mini CTA). The coefficients C_0 and C_1 can be obtained from a calibration in the absence of modulation. This procedure is realized by progressively increasing the methane/air flow mixture velocity by steps of $0.2 \text{ m}\cdot\text{s}^{-1}$ to cover the range of flowrates explored in this work. The evolution of the hot-wire voltage output \bar{E}_a with $\bar{v}_{u,c}^{0.405}$ is plotted in Fig. 1.6. The coefficients are calculated using a linear regression of the experimental data yielding $C_1 = 3.545 \text{ [m}\cdot\text{s}^{-1}\cdot\text{V}^{-1]}^{0.405}$ and $C_0 = -4.082 \text{ [m}\cdot\text{s}^{-1}]^{0.405}$.

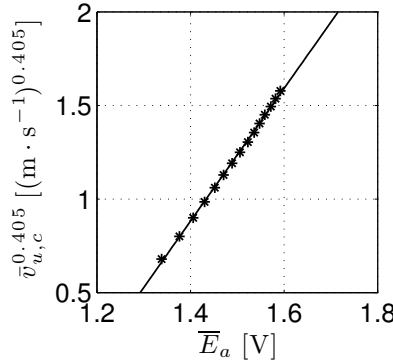


Figure 1.6 : Plots of $\bar{v}_{u,c}^{0.405}$ versus the hot-wire anemometer voltage output \bar{E}_a , where $\bar{v}_{u,c}$ denotes the predicted flow velocity from the mass flowrate controller. The markers * represent the measurements and the solid line denotes the linear regression based on these data.

1.2.2 Control of the velocity forcing level

The signal synthesizer (wave generator or LABVIEW program) is connected to the Hifi amplifier and is operated with a certain gain kept constant. The resulting velocity signal is measured by the hot-wire anemometer in the absence of flame at the burner exit. The transfer function between the forcing signal U_{ss} from the synthesizer output and the velocity signal v_u is determined. Results are first plotted in Fig. 1.8 for the root mean square value of the velocity signal $v_{u,rms}$ and its phase lag with respect to the forcing signal $U_{ss,rms}$ for increasing perturbation levels. The velocity modulation level increases linearly with the

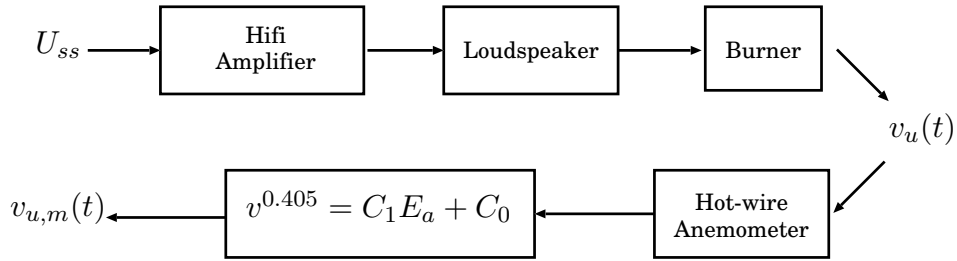


Figure 1.7 : Chain of the signals from the synthesizer voltage output U_{ss} to the axial velocity measured by hot-wire anemometry $v_{u,m}(t)$ at the burner exit.

excitation but the slope and the phase lag with respect to the forcing signal is a function of frequency. Figure 1.9 shows the evolution of the gain and phase difference with frequency for three operating conditions characterized by dif-

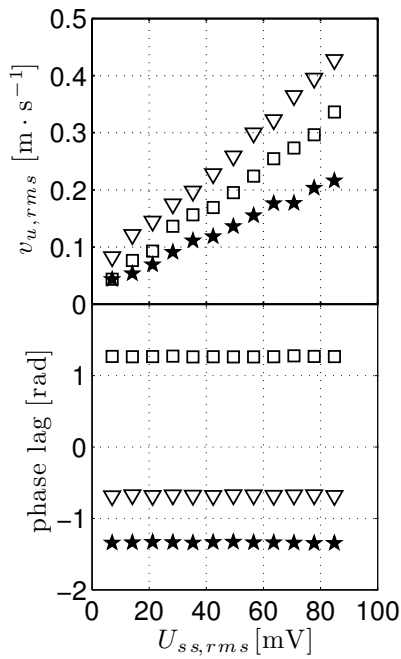


Figure 1.8 : Plots of the root mean square value of the velocity signal $v_{u,rms}$ (top figure) and its phase lag (bottom figure) with respect to the forcing signal $U_{ss,rms}$ for increasing perturbation levels. Results at three modulation frequencies are presented: 20 Hz (\star), 50 Hz (∇) and 80 Hz (\square).

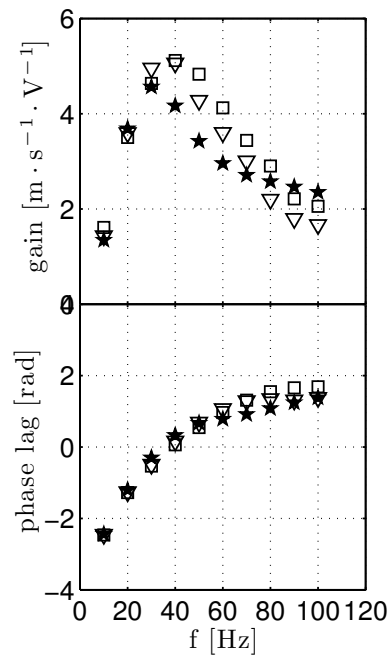


Figure 1.9 : Evolution of the gain $=v_{u,rms}/U_{ss,rms}$ (top figure) and phase lag (bottom figure) with modulation frequency f for three different operating conditions characterized by velocity \bar{v}_u : $1.1 \text{ m} \cdot \text{s}^{-1}$ (\star), $1.5 \text{ m} \cdot \text{s}^{-1}$ (∇) and $1.9 \text{ m} \cdot \text{s}^{-1}$ (\square).

ferent flow velocities analyzed in this work. The gain and the phase lag of the three cases explored are nearly the same indicating that the transfer function is weakly dependent on the mean flow velocity.

1.3 Characterization of the flame response to flow disturbances

Disturbances of the flame induced by external flow modulation or flow instabilities are characterized in this work by measuring the resulting heat release rate perturbations and flame front deformations. Recording the chemiluminescence emission from the reaction zone is used as a reference technique to measure the heat release rate.

The chemiluminescence can be evaluated with a photodiode (PM) or by directly imaging the flame with a camera (CCD and ICCD). The PM records the global emission from the flame over a large solid angle and gives time resolved data. Cameras yield a spatial distribution of luminosity intensity at a certain repetition rate limited to the framing and recording rates from the CCD and ICCD devices.

The unsteady flow investigated being laminar, phase conditioned average images can be recorded using a camera operating a relatively low framing rate. Two methods are used in this work to obtain phase resolved data of the flame motion. The first method is based on the stroboscopic effect. The flame modulation frequency is tuned close, but not exactly equal, to an integer ratio of the framing rate. The tiny unbalance between the modulation frequency and the framing rate enables to scan the flame motion with the CCD camera at low speed by stroboscopic effect. In the second method, the camera is triggered by the forcing signal driving the loudspeaker and this enables to take synchronized snapshots of the flame at a given phase with the ICCD camera. This latter technique enables to increase the contrast by accumulation of the images recorded at the same phase of the excitation cycle.

When the flame front is disturbed, the burned gases surrounding the flame are also pulsating. This results in the displacement of the interface between the burned gases and ambient air. The position of this interface is important for acoustic measurements as will be shown in the next chapter. Due to the strong density gradients near the flame front and the interface between burned gases and ambient air, a color Schlieren system is also used to highlight these different fluid layers in the experiments.

Table 1.3 : *Characterization of the flame shape and heat release rate.*

Equipment	Manufacturer	Type	Characteristics
Photodiode Instrumentation Amplifier	Hamamatsu	H5784-6 C7196	Spectral bandwidth: 185 - 650 nm Frequency response: 0 - 20 kHz Gain: 0 -160 dB Gain/control voltage: 110dB · V ⁻¹
CCD Camera	Pulnix	TMC-6	Spectral bandwidth: ≈ 350 - 1000 nm Frame rate: 50 frames·s ⁻¹ Store rate: 1 frames·s ⁻¹ CCD size: 768×494 pixels Shutter speed: 1/10000 - 1/60 s
ICCD Camera Controller	Princeton	PI-MAX 1 ST-133	CCD size: 512×512 pixels

1.3.1 Photodiode (PM)

A photodiode (Hamamatsu H5784-6) working with a spectral bandwidth covering 185 to 650 nm and featuring a cut-off frequency (20 kHz) much larger than the largest modulation frequency investigated in this study, enables to record the chemiluminescence intensity from the main naturally excited radicals OH*(≈310 nm), CH*(≈431 nm) and C₂*(≈516 nm) present in the flame reaction zone. A module (C7169) supplies the power to the sensor. It enables to change the gain of the output voltage from the sensor. No optical filter is used in this work and the light intensity is collected over the wavelength bandwidth of the sensor. For the laminar premixed flames considered here, it is possible to estimate the heat release rate \dot{Q} by examining the chemiluminescence intensity I of these radicals present in the reaction zone (Price et al. 1969; Schuller et al. 2002b) :

$$\dot{Q} = kI \quad (1.9)$$

The coefficient k is a function of the experimental apparatus and mixture composition. It can be determined by a calibration procedure presented later in this manuscript.

1.3.2 Charged coupled device camera

A charged coupled device (CCD) camera, Pulnix, TMC-6, is employed to record the light intensity from the flame and track the flame motion. The spectral bandwidth of the CCD covers 350 nm - 1000 nm. The chemiluminescence from CH* and C₂* radicals from the flame can be recorded but the OH* UV emission is filtered by the optics and the CCD array. This camera works with a fixed frame rate equal to 50 frames per second. This rate enables to record 10 phases

in 1 period for a flame modulated with a frequency 50.1 Hz. The exposure time, which can be adjusted by the shutter speed, determines the number of photons impacting onto the CCD. The CCD has a matrix of 768×494 square pixels and the spatial resolution can be changed using a zoom on the objective.

1.3.3 Intensified charged coupled device camera

It is necessary to reduce the exposure time of the camera to obtain phase resolved data of the flame motion modulated at high frequency. Meanwhile, the signal-to-noise ratio SNR is also reduced. An intensified charged coupled device camera (Princeton Instruments, PI-MAX 1) with a ST-133 controller is used to address this problem. With an image intensifier mounted in front of the CCD and a very fast gating rate, the ICCD camera enables to record the flame motion with a small integration time to obtain phase resolved images at high forcing frequencies. It has a matrix of 512×512 square pixels and the spatial resolution can be adjusted with an objective equipped with a zoom. The ICCD camera can be operated in a gate mode. The gate opens when it is triggered by

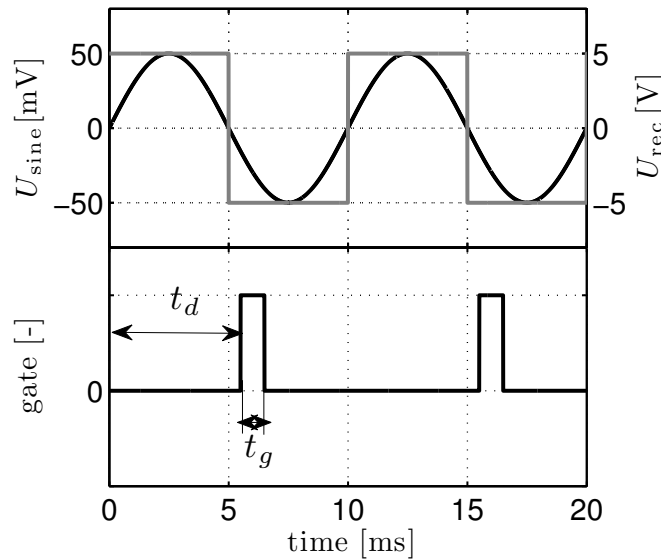


Figure 1.10 : Schematic of the external trigger TTL signal (upper figure) and the gating of the ICCD camera (bottom figure). The black line in the upper figure indicates the signal sent to the loudspeaker and the gray one is the synchronized TTL signal used to trigger the ICCD camera. The solid line at the bottom is a schematic of the camera gating system where t_g is the width of the gate and t_d denotes the time delay of the gate.

the external TTL signal from the signal synthesizer which is presented in the upper part in Fig. 1.10. The accumulation of the images at a given phase and the “scan” of a complete forcing period can be realized by changing the values of the gate width t_g and the time delay of the exposure t_d .

1.3.4 Color Schlieren technique

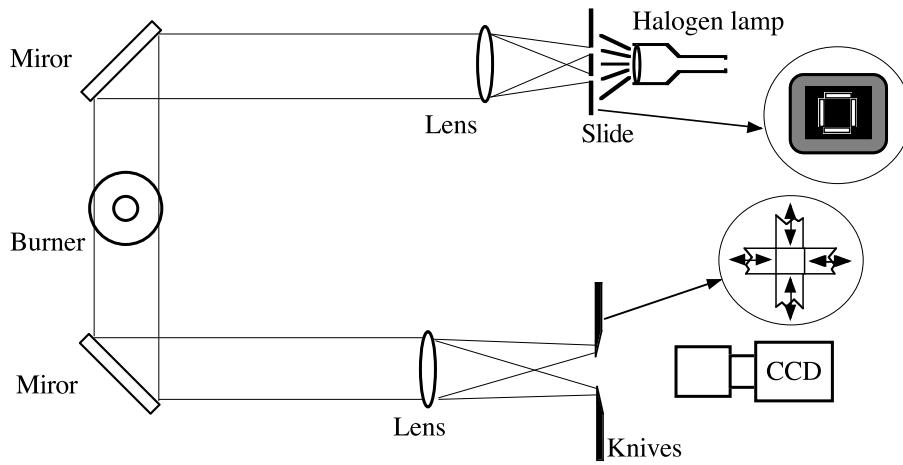


Figure 1.11 : Schematic of the color Schlieren apparatus.

A color Schlieren technique, highlighting density gradients by light deflection, is used to visualize the flame together with the burned gases surrounding the flame front (Durox et al. 1998; Durox and Ducruix 2000). A schematic representation of this color Schlieren arrangement is shown in Fig. 1.11. A parallel light beam is created with a Halogen lamp associated with a slide located at the primary focal point of a converging lens. The slide has four narrow slots configured with different color filters. Two plane mirrors are used to rotate the parallel light beam with an angle of 90° to reduce the space required for this system. The flame is placed in the optical path of the parallel light beam and part of the light is deflected. After crossing the reactive flow, the parallel beam is refocused with a second converging lens. A device with four knife-edges is placed at the object focal plane of the second lens to cut off part of the transmitted light. The light that is deflected toward or away from the knife edges produces a shadow pattern characterizing the density gradients of the flame and burned gases. These knife-edges can be adjusted to highlight the horizontal or vertical density gradients. A CCD camera is placed downstream the four knife-edges to record the Schlieren images. One example is shown in Fig. 1.12, where red and green filters separate the light deflected in different horizontal directions and highlight the flame front (inner luminous area) from the limit of the hot

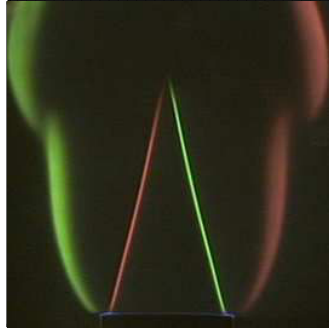


Figure 1.12 : *Color Schlieren image of a conical methane-air premixed flame ($\phi = 0.90$, $v_u = 1.50 \text{ m} \cdot \text{s}^{-1}$).*

plume surrounding the flame (outer luminous area).

1.4 Ultrasonic transducer and receiver

The LABVIEW program connected to an internal digital to analog converter is used to generate the forcing signals with a very large sampling rate. This signal is amplified in the Hifi amplifier to drive a tweeter. This tweeter has a wide working bandwidth enabling to produce ultrasonic waves. These sound waves propagate in air and cross the flame. They are recorded by two microphones located before and after the reaction zone. These devices have a wide frequency bandwidth. The acoustic pressure is converted to electrical signals which are recorded by the analog to digital convector and processed in the LABVIEW program.

The response of these devices to high frequency waves generated by the signal synthesizer is examined in the next sections using the setup described in Fig. 1.13. The distance between the microphone and the tweeter is characterized by L_{LM} .

1.4.1 Response to harmonic excitation

Tests are firstly done to validate the response of the tweeter and microphones to harmonic excitation. The tweeter is driven by the wave generator with a pure tone. Signals measured by the microphone are sampled with a frequency $f_s = 2^{20}$ Hz over one second. Tests are done for different modulation frequencies and distances L_{LM} . The frequency is swept from 5 to 50 kHz by steps of 1 kHz while the distance increases from 0 to 500 mm by steps of 10 mm.

Table 1.4 : *Ultrasonic wave generation and reception system characteristics.*

Equipment	Manufacturer	Type	Characteristics
Tweeter	Fostex	FT17H	Impedance: 8 ohms Maximum power: 30 W Sensitivity: 98.5 dB·W ⁻¹ Frequency range: 5 -50000 Hz Core diameter: 42 mm
Hifi amplifier	JCB	XPP 7000	Maximum power: 245 W/ 8 ohms
Microphone	Brüel & Kjaer	4938	Pressure field 1/4 inch Sensitivity: 1.6 mV·Pa ⁻¹ Response: 4 - 70000 Hz Dynamic range: 30 - 172 dB Temperature: -40 - 300 °C
Preamplifier		2670	1/4 inch Phase linearity: ≤ ±1° below 100 kHz Signal attenuation: ≤ 0.4 dB
Nexus conditioner			
A/D converter	National Instruments	BNC 2090 PCI-6111 S	2 outputs Output scanning rate: 5 M Samples/s Maximum output voltage: 5 V

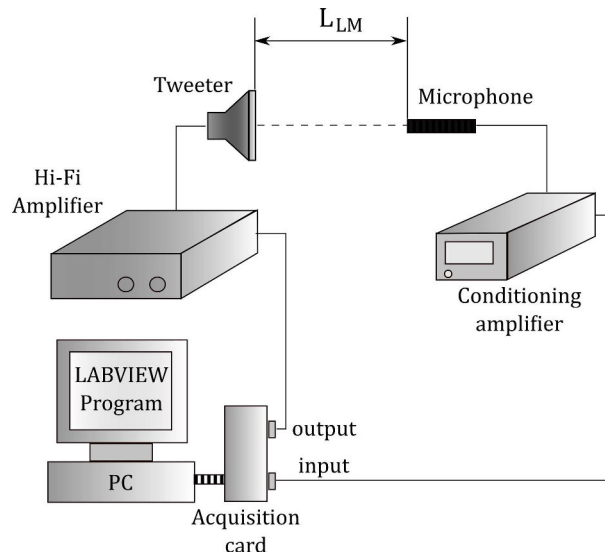


Figure 1.13 : *Schematic of the configuration used to test the response of the tweeter. The microphone is located at a distance L_{LM} .*

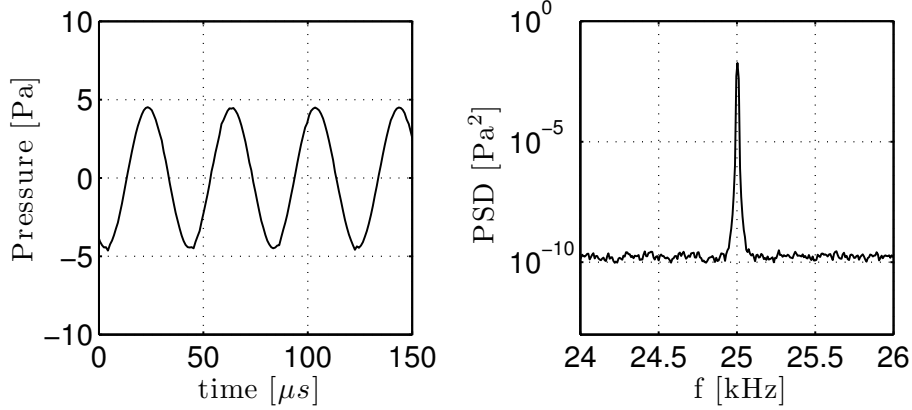


Figure 1.14 : Sound pressure time trace (left figure) and power spectrum (right figure) of the signal generated by the tweeter modulated at 25 kHz and recorded by the microphone. The distance between the tweeter and microphone is $L_{LM} = 100$ mm.

One example presented in Fig. 1.14 shows that the tweeter features a response with a pure tone when it is driven by a harmonic signal. Its response to excitation is defined by $R_{pU} = p_{m,rms}/U_{ss,rms}$, where p_m is the signal measured by the microphone and U_{ss} is the voltage output signal from the synthesizer. The root mean square value (rms) is used to calculate the response. Figure 1.15 plots the response R_{pU} with forcing frequency for increasing distances L_{LM} . The response is not flat and varies with the modulation frequency at a given distance L_{LM} . This is attributed to the different mechanical and electrical devices in the signal generation and reception chains. It can also be noted that the level of response decreases with the distance L_{LM} .

The amplitude of the pressure waves produced by the tweeter decreases exponentially as a function of the distance from the tweeter L_{LM} (Shung 2005):

$$R_{pU}(f, L_{LM}) = R_{pU}(f, 0) \exp(-\alpha_d L_{LM}) \quad (1.10)$$

where $R_{pU}(f, 0)$ is the response at $L_{LM} = 0$ and α_d is the rate of decrease. Figure 1.16 shows this evolution with the distance L_{LM} at two modulation frequencies 25 kHz and 45 kHz. The solid lines in this figure correspond to theoretical predictions from Eq. (1.10). The rate of decrease at these two frequencies is equal to $\alpha = 3.4 \text{ m}^{-1}$ in both cases for distances larger than $L_{LM} \geq 100$ mm. To increase the signal to noise ratio in reacting flow conditions, the distance between the tweeter and the microphone L_{LM} should not be too far. In this work it was fixed to $L_{LM} = 300$ mm.

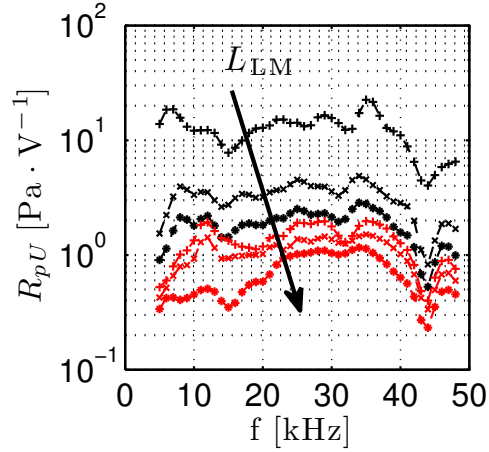


Figure 1.15 : Evolution of the response R_{pU} with the modulation frequency measured at different locations downstream the tweeter. The frequency varies from 5 to 50 kHz and the distance L_{LM} is increased from 0 to 500 mm by steps of 100 mm.

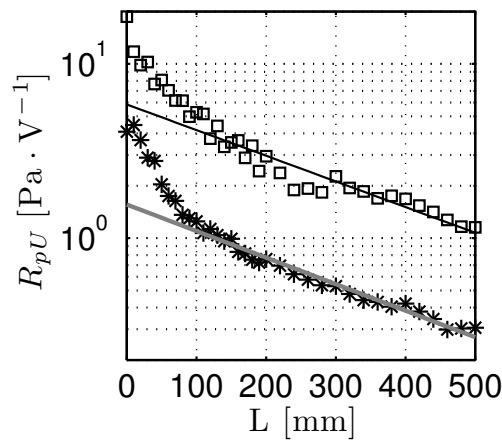


Figure 1.16 : Plot of the response R_{pU} versus the distance between the tweeter and microphone L_{LM} for two modulation frequencies 25 kHz (\square) and 45 kHz (*). The solid lines correspond to the theoretical predictions from Eq. (1.10).

1.4.2 Response to linear frequency modulation excitation

The type of forcing signal employed for acoustic measurements proposed in this work corresponds to sequences of short pulses with linear frequency modulations denoted by “chirp”. It is therefore necessary to check the response of the tweeter to this kind of signal. These experiments are conducted with the LAB-

VIEW program to generate short chirp sequences. Therefore, it is necessary to check if this system can produce this kind of excitation without too much distortion.

The configuration used to test the response of the tweeter is the same as that shown in Fig. 1.13. The LABVIEW program coupled to a National Instrument analog/digital converter can generate and record signals simultaneously. The signal used to drive the tweeter is recorded together with that measured by the microphone. These two signals are sampled at the same frequency $f_s = 2^{20}$ Hz. Figure 1.17 shows one example where the frequency of the forcing signal is linearly modulated from 5 to 50 kHz during a period of 2 ms with a constant amplitude in the LABVIEW program. The sound pressure recorded by the microphone is slightly distorted as indicated in the right part of the figure. This is because the response of the tweeter and microphone changes with frequency.

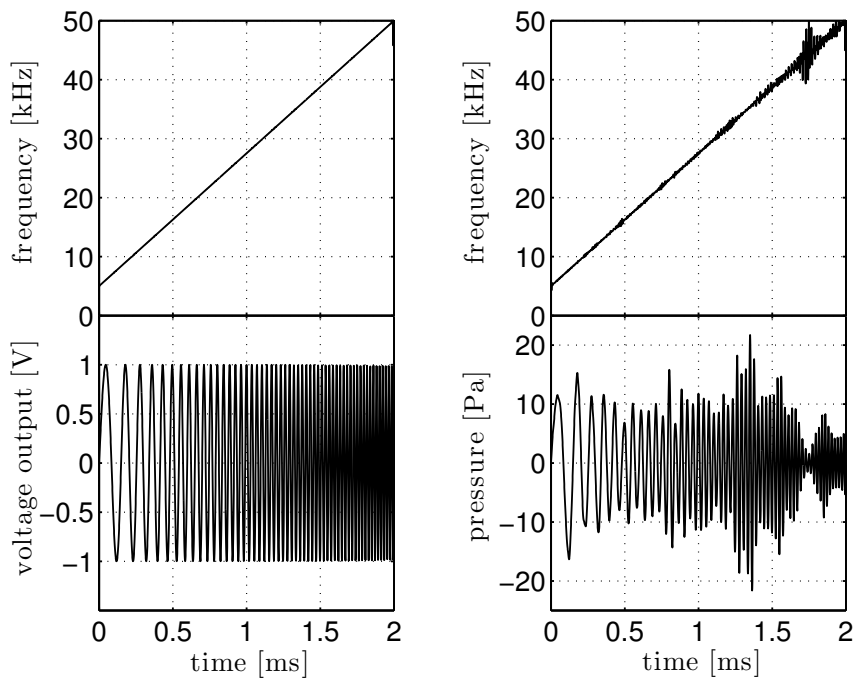


Figure 1.17 : Evolution of the instantaneous frequency (upper graph) and amplitude (bottom graph) with time of the forcing signal generated by the signal synthesizer (left figure) and the pressure signal measured by the microphone (right figure). The frequency of the forcing signal is linearly modulated from 5 to 50 kHz during a period of 2 ms with a constant amplitude in the LABVIEW program. The distance between the microphone and the tweeter is equal to $L_{LM}=10$ mm.

To determine the response of the tweeter to the frequency-modulated forcing signal, a time-frequency analysis is conducted to analyze the evolution of the signal frequency with time. First, an analytical signal is constructed by the following procedure. For any real valued signal $s(t)$, one associates a complex valued signal $s_a(t)$ defined as:

$$s_a(t) = s(t) + j\mathcal{H}(s(t)) \quad (1.11)$$

where $\mathcal{H}(s(t))$ is the Hilbert transform of $s(t)$ (Oppenheim and Schaffer 1975). The original real signal $s(t)$ is simply the real part of this analytical representation. This imaginary component $\mathcal{H}(s(t))$ corresponds to signal which is rotated by 90° in the complex plane with the same magnitude and frequency content as the real signal.

For a harmonic excitation, the corresponding analytic signal can be rewritten as:

$$s_a(t) = A(t) \exp[j2\pi f(t)] \quad (1.12)$$

where $A(t)$ indicates the instantaneous amplitude and $f(t)$ denotes the instantaneous frequency. These components can be extracted from the analytical representation by calculating:

$$A(t) = |s_a(t)| \quad (1.13)$$

$$f(t) = \frac{1}{2\pi} \frac{d \arg s_a(t)}{dt} \quad (1.14)$$

The upper figures in Fig. 1.17 show the evolution of the instantaneous frequency with time of the forcing signal from the signal synthesizer output voltage (left figure) and the pressure signal measured by the microphone (right figure). The output voltage of the digital-to-analog convertor driven by LABVIEW features the expected response with a linear frequency increase from 5 to 50 kHz (left figure, top graph) and a constant amplitude (left figure, bottom graph) over the entire frequency range. The resulting signal measured by the microphone also shows a linear frequency increase but with some distortion above 40 kHz (right figure, upper graph). The amplitude remains roughly constant for frequencies lower than 30 kHz, with a slight amplification from 30 to 40 kHz and then a rapid decrease with frequency for higher frequencies. The distortion is induced by the weaker response of the tweeter at high frequency. The choice of the operating frequency bandwidth for the forcing signal used in this work will be optimized to avoid too much distortion in the results presented in next chapters.

1.5 Conclusion

An experimental platform used to validate the proposed techniques was first described. It comprises mainly a cylindrical burner to stabilize laminar conical premixed flames. With a convergent exit, the burner can produce a flat and uniform axial velocity profile at the exit. The mean flow velocity is modulated by a loudspeaker configured at the base. The perturbation levels of the axial flow velocity at different frequencies and flow operating conditions were calibrated by a hot-wire placed at the burner exit. Four different techniques (a photodiode, a CCD camera, an ICCD camera and a four color Schlieren system) used to image the flame and to characterize the flame motion were then presented. Finally, the responses of the main elements of the acoustic technique, an ultrasonic wave emitter and two microphones with large bandwidth responses, were examined experimentally. These devices enable to generate and record short “chirp” sequences used as the probing signals of the acoustic technique which will be presented in the next chapter.

Chapter 2

Principle of the acoustic method

Ultrasonic waves barely perturb with flames. This property is used in this work to probe unsteady laminar flames. Fluctuations of the sound propagation time transmission through unsteady flames is used in this chapter to estimate perturbations in the burned gases width. This information is then used in the next two chapters to reconstruct the corresponding heat release rate disturbances. To detect small differences in the sound travel time, a pulsed compression technique with a linear frequency modulation associated with a matching filter are employed. The generation and post-processing of these signals are described in this chapter. Effects of the main parameters on the precision of this detection technique are examined theoretically and experimentally. The performance of the matching filter is examined when the compressed pulses are embedded with white noise. A pre-processing analysis which aims at improving the precision of the matching filter is proposed at the end of this chapter.

2.1 Background

Ultrasonic waves are widely used as a real-time probe in sonars, radars and medical imaging technologies (Stergiopoulos 2000). The waves from an antenna (emitter) are transmitted to the space, reflected by the object being investigated and then recorded by a sensor. A matching filter is generally applied to the incident signal and the echo signal to extract the propagation time of the ultrasonic waves. The resulting information can then be used for example to reconstruct the distance between the antenna and the object investigated. This principle is used here to estimate perturbations in the width of gases characterized by a different speed of sound the between emitter and receiver.

2.2 Model of sound travel time

Consider the case of a plane sound wave traveling through a homogeneous gas at a fixed temperature and composition characterized by a speed of sound c_u and over a distance L . The propagation time Δt_0 is given by:

$$\Delta t_0 = \frac{L}{c_u} \tag{2.1}$$

When sound waves cross a different medium, the speed of sound in this region is modified and the propagation time is in turn also altered. This configuration is shown in Fig. 2.1, where acoustic waves emitted by a tweeter propagate through two different media. The second gas is characterized by a speed of sound c_b and extends over a length L_f along the acoustic path. The first gas now occupies a length $L - L_f$. In this configuration, Eq. (2.1) is modified and the propagation time Δt between the emitter to the receiver separated by a distance L is now given by:

$$\Delta t = \frac{L - L_f}{c_u} + \frac{L_f}{c_b} = \Delta t_0 - \frac{L_f}{c^*} \tag{2.2}$$

where $c^* = c_b c_u / (c_b - c_u)$ is an equivalent speed of sound.

Consider now perturbations in the distance L_f .

- (i) This may for example take place in unconfined configurations for flames stabilized on the rim of a burner because of shear flow instabilities. This configuration is envisaged in Fig. 2.2 where the acoustic path crosses the burned gases characterized by a speed of sound c_b which are surrounded by fresh air with a speed of sound c_u . Buoyancy effects are known to induce a low frequency oscillation of the flame plume due to a shear layer instability between the hot combustion products and surrounding ambient air (Kostiuk and Cheng 1994; Durox et al. 1997b). This results in turn in small perturbations in the heat release rate and in fluctuations of the volume of the burned gases. Consequently the length of the burned gases width L_f traversed by ultrasonic waves is also modified. This configuration is shown using the color Schlieren images in Fig. 2.4.

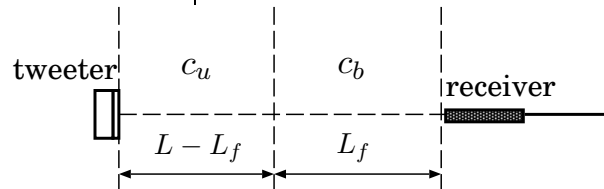


Figure 2.1 : Schematic view of two different homogeneous media between the transmitter and receiver characterized by different speed of sound.

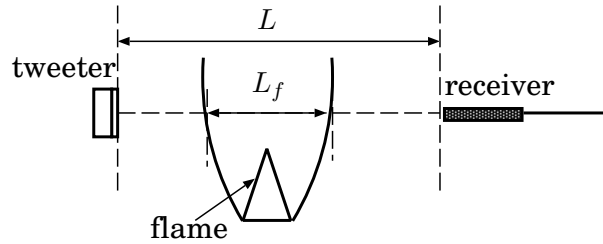


Figure 2.2 : Schematic view of an unconfined conical flame. A sound wave generated by an ultrasonic emitter propagates through ambient air, burned gases before reaching a receiver. The distance between the emitter and receiver is L . Waves propagate through the burned gases over a distance L_f .

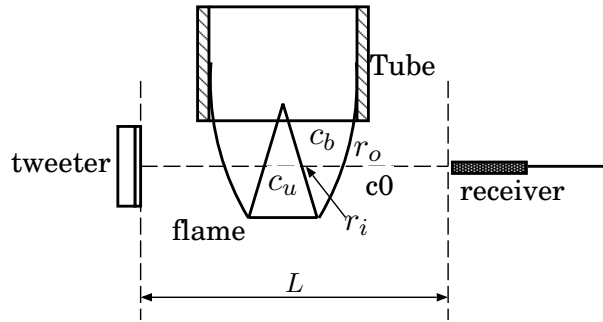


Figure 2.3 : Schematic view of a flame partially confined by a quartz tube. A sound wave generated by an ultrasonic emitter propagates through ambient air, burned gases and fresh mixture before reaching a receiver. The distance between the emitter and receiver is L . Waves propagate through the burned gases over a distance $L_f = 2(r_o - r_i)$, where r_i indicates the location of the flame front and r_o denotes the radius of the interface between the hot plume and ambient air.

- (ii) In the case of a conical premixed flame stabilized on the axisymmetric burner schematically represented in Fig. 2.3, the situation is slightly different. A quartz tube placed on the top of the flame is used to suppress the flow buoyancy instability and the flame is steady for steady flow operating conditions. Ultrasonic waves cross successively ambient air, burned gases which are separated from the fresh mixture by the flame sheet. In hydrocarbon air flames, the fresh mixture is strongly diluted by nitrogen (Xiao and Puri 2001; Ibarreta and Sung 2005) which is injected here at the same temperature as ambient air so that the speed of sound in these media can be considered equal $c_u = c_0$. In this case, the situation is then very much like that depicted in Fig. 2.1 where the length of the acoustic path in the burned gases corresponds to $L_f = 2(r_o - r_i)$, r_o being the radius of the interface between the hot plume and ambient air and r_i the position of the flame front. When the upstream flow is modulated, flow disturbances produce a flame motion and heat release rate perturbations. The flame front is then wrinkling (r_i fluctuates with respect to time) and the position r_o of the burned gases interface is also found to displace in a regular fashion. An example of motions of these two interfaces is given in Fig. 2.5 .

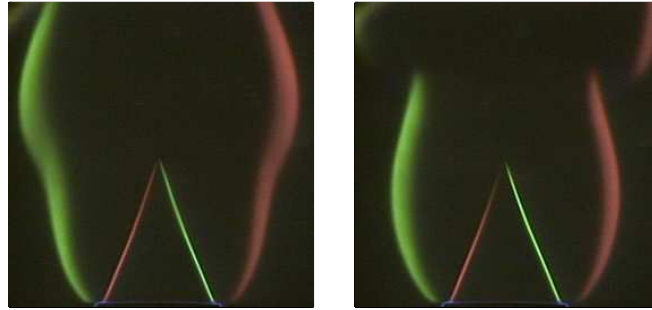


Figure 2.4 : *Color Schlieren images of a methane-air premixed flame ($\phi = 1.00$, $v_u = 1.10 \text{ m} \cdot \text{s}^{-1}$) at two instants. The length L_f of the burned gases width corresponding to the outer luminous interface is perturbed by the buoyancy induced flow instability.*

The consequence of these internal flow perturbations or external flow modulations is that the length L_f fluctuates in time. It can be split in two terms $L_f = \overline{L_f} + L_f'$ corresponding to the mean and unsteady components respectively. Thus the propagation time of an acoustic wave Δt is also fluctuating and can be written as $\Delta t = \overline{\Delta t} + \Delta t'$. The frequency of the buoyancy effect or flow modulation remains low compared to the inverse of flight time i.e. $f\Delta t \ll 1$. In

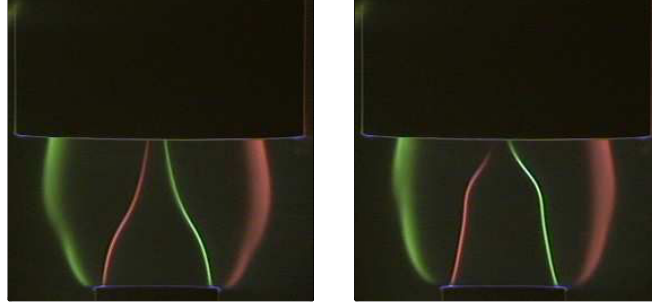


Figure 2.5 : Color Schlieren images of a partially confined conical flame ($\phi = 1.00$, $\bar{v}_u = 1.5 \text{ m} \cdot \text{s}^{-1}$) submitted to harmonic flow velocity modulations at $f = 40 \text{ Hz}$ and a fixed perturbation level $v_{urms}/\bar{v}_u = 0.07$. Two instants are represented in the modulation cycle: $1/10 T$ and $6/10 T$, where T is the period of the modulation. The flame front r_i is indicated by the inner luminous zone and the radius of the interface between the hot plume and ambient air r_o is represented by the outer luminous zone.

these conditions, the flow between the emitter and receiver appears very much like frozen with respect to the traveling time of ultrasonic waves. In these situations, the sound travel time is only altered due to changes in the burned gases and fresh mixture widths. These disturbances originate from flame front wrinkling when the flame is submitted to flow modulations. The link between the mean and fluctuating components of L_f and Δt can be deduced from Eq. (2.2):

$$\overline{\Delta t} = \Delta t_0 - \frac{\overline{L_f}}{c^*} \quad \text{and} \quad \Delta t' = -\frac{L_f'}{c^*} \quad (2.3)$$

In this expression only disturbances in the acoustic path length L_f are taken into account. Fluctuations in temperature and composition of the fresh mixture and burned gases are neglected. This approximation is valid as long as relative perturbations of the equivalent speed of sound remain small $c^{*'} / c^* \ll 1$. This may not be the case in some practical configurations, but it is admitted here. Analysis of this approximation will be the object of further work but this is beyond the scope of the present study. Equation (2.3) is used here to estimate fluctuations in acoustic path length L_f' by measuring the fluctuations of the acoustic propagation time assuming a constant speed of sound of the burned gases. The link between fluctuations in the acoustic path length L_f' with disturbances in heat release rate is established in the next two chapters for the different cases envisaged. This chapter mainly focuses on the determination of the sound travel time. The method used to that purpose is presented in the next sections.

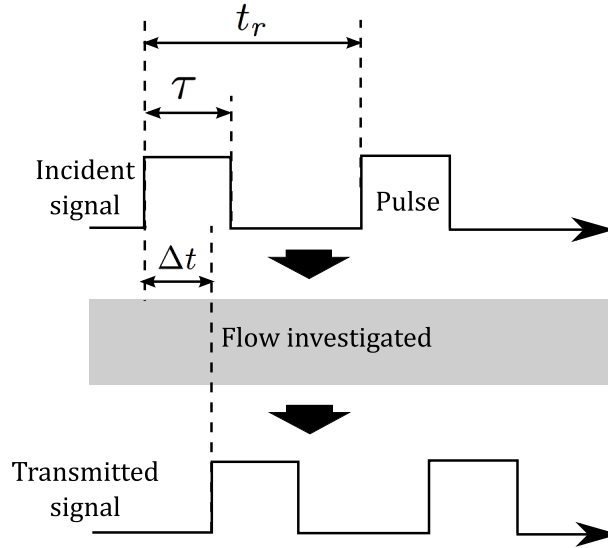


Figure 2.6 : Train of incident and transmitted pulses. Only the signal envelope is represented in this figure.

2.3 Detection of sound travel time

High frequency periodic waves are employed due to their weak interactions with flames (McIntosh and Wilce 1991). Generally, continuous waveforms (CW) or pulsed waveforms with or without modulation are applied to measure sound travel time (Merrill 2008). Techniques with continuous sine waves are often preferred to detect fluctuations in sound travel time due to the Doppler effect induced by disturbances in the speed of sound along the acoustic path (Cook and Bernfield 1993). These types of signals are associated with a post-processing done in the frequency space during a time interval to extract the Doppler frequency which varies linearly with fluctuations in sound travel time (Brandwood 2003). But this technique is limited to high frequency detection since its resolution depends on the duration of time interval. To overcome this shortcoming, a time-frequency analysis (Cohen 1994; Akay 1997; Boashash 2003) may eventually be used.

We are seeking only fluctuations in the sound propagation time to examine heat release rate disturbances. Sequences of short pulses are used as schematically represented in Fig. 2.6. These repeated pulse sequences are characterized by a pulsewidth τ with a repetition time t_r . When a pulse generated by the emitter passes through the flow investigated, it features a certain time delay Δt . The cross-correlation is used as the matching filter to extract the sound propagation time Δt . The cross-correlation between the incident signal $S_i(t)$ and transmitted signal $S_t(t)$ can be expressed as (Hussain et al. 2011):

$$R_{ti}(t) = \frac{1}{\tau} \int_0^\tau S_t^*(t') S_i(t' - t) dt' \quad (2.4)$$

where, $S_t^*(t)$ denotes the complex conjugate of $S_t(t)$. The correlation gives an indication of how the two signals are “related” to each other when the time lag between them is Δt . In other words, it is a measure of similarity between the two signals separated by Δt . The correlation integral reaches a maximum value at $t = \Delta t$ if the two signals are very similar. The correlation function features then a sharp peak located at the position Δt . This correlation function takes otherwise small values if one signal is deterministic and the other is random noise.

In the harsh measurement environment envisaged in this work, a fraction of power of the signal at one frequency is scattered by the flame and the inhomogeneous flow (Lieuwen et al. 2002). The peak of the direct cross-correlation between the incident signal and transmitted signal does not always give the correct propagation time. The envelope of the cross-correlation may also be used as suggested by Thrane et al. (1985), Wilson (1990) and Mirgorodskii et al. (2008) to overcome this problem. The envelope of the cross-correlation $R_{ti}(t)$ is defined by:

$$\mathcal{E}_{ti}(t) = \left[R_{ti}^2(t) + \mathcal{H}(R_{ti}^2(t)) \right]^{\frac{1}{2}} \quad (2.5)$$

where, \mathcal{H} indicates the Hilbert transform which was detailed in Chapter 1. The peak of the envelope $\mathcal{E}_{ti}(t)$ indicates the propagation time Δt as exemplified in Fig. 2.8.

In this work, sequences of sine wave pulses with short duration are used to probe unsteady reacting flows.

2.3.1 Signal waveform

Sine wave pulses with a linear frequency modulation (“chirp”) are employed as the detection signal. This signal is characterized by a constant amplitude β with a pulse duration τ and linear frequency modulation covering a frequency bandwidth B . The mathematical form of the pulse can be expressed as (Klauder et al. 1960):

$$S_m(t) = \beta \text{rect}\left(\frac{t}{\tau}\right) \sin\left(2\pi \left[f_o t + \frac{\mu}{2} t^2\right]\right) \quad (2.6)$$

where, f_o is the carrier frequency of the signal, and $\mu = \pm B/\tau$ denotes the slope of frequency modulation. The sign (+) indicates “up-chirp” with an in-

creasing frequency (Fig. 2.7(a)) while the sign (−) represents “down-chirp” with a decreasing frequency (Fig. 2.7(b)). The rect-function is defined as:

$$\text{rect}(x) = \begin{cases} 1 & |x| \leq \frac{1}{2} \\ 0 & |x| > \frac{1}{2} \end{cases} \quad (2.7)$$

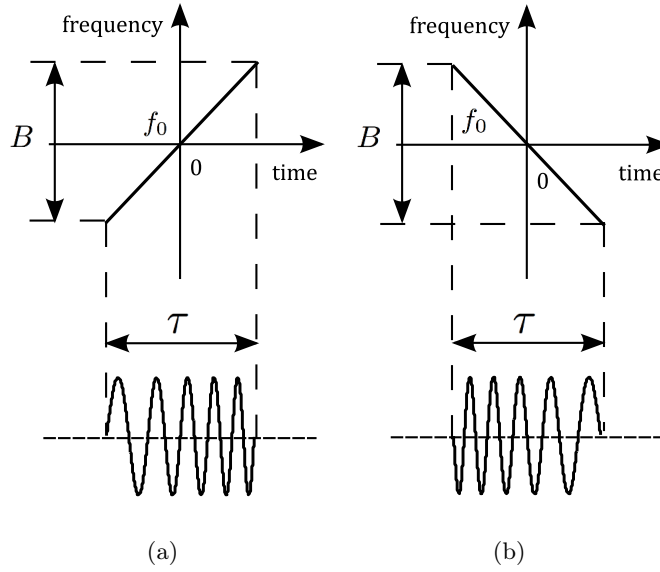


Figure 2.7 : Two kinds of waveform with linear frequency modulation (chirp). (a) up-chirp; (b) down-chirp.

The instantaneous phase of the signal can be expressed by:

$$\varphi(t) = \text{rect}\left(\frac{t}{\tau}\right) \left[2\pi \left(f_0 t + \frac{\mu}{2} t^2 \right) \right] \quad (2.8)$$

and the instantaneous frequency is given by:

$$f(t) = \frac{1}{2\pi} \frac{d}{dt} \varphi(t) = \text{rect}\left(\frac{t}{\tau}\right) (f_0 + \mu t) \quad (2.9)$$

“Up-chirp” signals are used in this work.

To compare the temporal resolution offered by this kind of signal, an harmonic wave in the absence of frequency modulation is also used in these tests:

$$S_o(t) = \beta \text{rect}\left(\frac{t}{T}\right) \sin(2\pi f_o t) \quad (2.10)$$

To make the comparison easier, the transmitted signal is supposed to have the same waveform as the incident signal, but features a time delay Δt . When

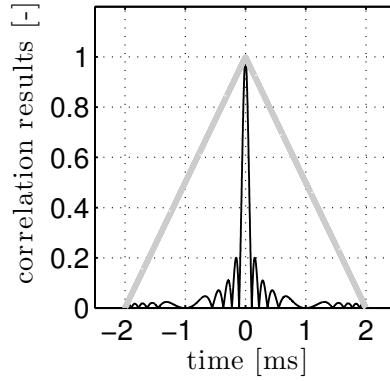


Figure 2.8 : *Envelop of the auto-correlation results of the signals with frequency modulation (black line) and without modulation (gray line). $\tau = 2$ ms, $f_0 = 10$ kHz and $B = 5$ kHz.*

$\Delta t = 0$, the cross-correlation between the transmitted signal is simplified to the auto-correlation of the incident signal.

The envelope of the auto-correlation function of the chirp signal presented in Eq. (2.6) is given by Merrill (2008):

$$\mathcal{E}(t) = \left| \left(1 - \frac{t}{\tau} \right) \text{sinc}[\mu t(\tau - t)] \right| \text{rect}\left(\frac{t}{2\tau}\right) \quad (2.11)$$

where, the sinc function is defined as:

$$\text{sinc}(x) = \frac{\sin(\pi x)}{\pi x} \quad (2.12)$$

For the harmonic wave in the absence of frequency modulation, the envelope of the auto-correlation function is given by:

$$\mathcal{E}(t) = \left| 1 - \frac{t}{\tau} \right| \text{rect}\left(\frac{t}{2\tau}\right) \quad (2.13)$$

Examples of the envelopes of auto-correlation functions with and without frequency modulation are shown in Fig. 2.8. This figure clearly shows that the temporal resolution is improved with the frequency modulated signal. The chirp of duration τ features a main peak characterized a lobe of width $1/B$. The compression ratio $1/(B\tau)$ is an important factor characterizing the performance of the chirp signal and its cross-correlation (Mahafza and Elsherbeni 2004; Merrill 2008).

2.3.2 Optimization of the signal parameters

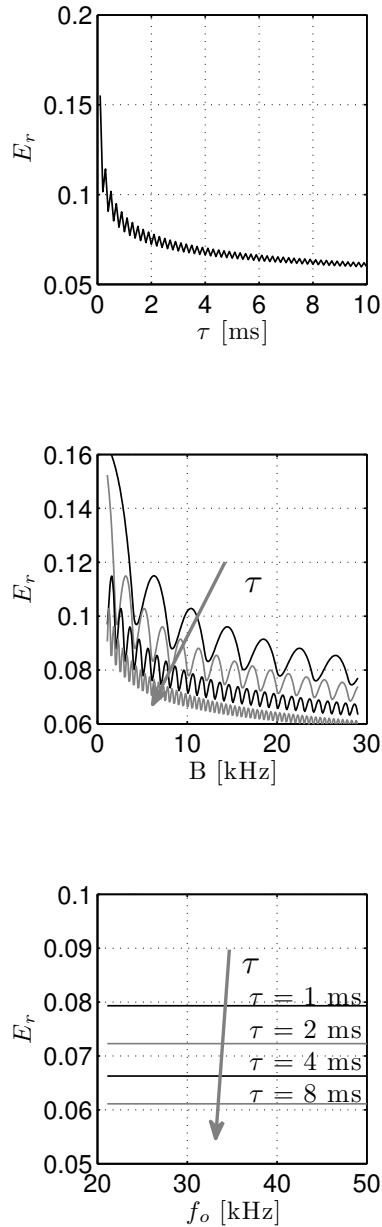


Figure 2.9 : Evolution of the error coefficient E_r with pulse duration τ , frequency bandwidth B and carrier frequency f_0 . Top figure: $f_0 = 30$ kHz, $B = 20$ kHz. Middle figure: $f_0 = 30$ kHz, four solid lines represent results for $\tau = 1, 2, 4$ and 8 ms respectively. Bottom figure: $B = 20$ kHz, four solid lines indicate results for $\tau = 1, 2, 4$ and 8 ms respectively.

The chirp signal is characterized by its frequency bandwidth B , pulse duration τ and carrier frequency f_0 . Effects of these different parameters on the precision of the detection technique are analyzed in this section. An error coefficient $E_r(\tau, B, f_0)$ is considered here as:

$$E_r = \frac{\int_{-\infty}^{\infty} (t' - \Delta t)^2 \mathcal{E}(t') dt'}{\int_{-\infty}^{\infty} \tau^2 \mathcal{E}(t') dt'} \quad (2.14)$$

When this coefficient goes to zero, detection of the sound propagation time Δt improves. Figures 2.9 show examples of results when the three parameters τ , B and f_0 are varied. It can be noted that increasing the pulse duration τ and frequency bandwidth B reduces the error coefficient significantly, while the carrier frequency f_0 has no effect on this coefficient. These numerical tests are completed by experiments in the next section.

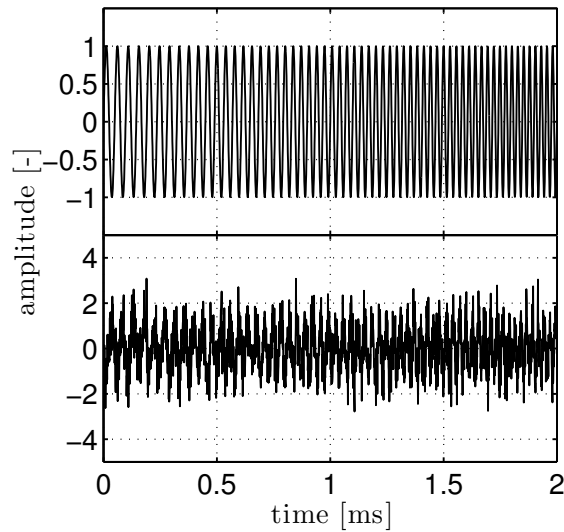


Figure 2.10 : Chirp signal (top figure) and chirp embedded in a 0 dB white gaussian noise (bottom figure). The parameters of the chirp : $f_0 = 30$ kHz, $B = 20$ kHz and $\tau = 2$ ms. $SNR=0$ dB.

For a periodic signal $s(t)$ embedded with random noise $n(t)$, the Signal to Noise Ratio (SNR) can be used to represent the noise level:

$$SNR = 20 \log_{10} \left(\frac{P(s(t))}{P(n(t))} \right) \quad (2.15)$$

where $P(s(t))$ is the average power of the signal $s(t)$ and is defined by:

$$P(s(t)) = \frac{1}{\tau} \int_0^\tau |s(t)|^2 dt \quad (2.16)$$

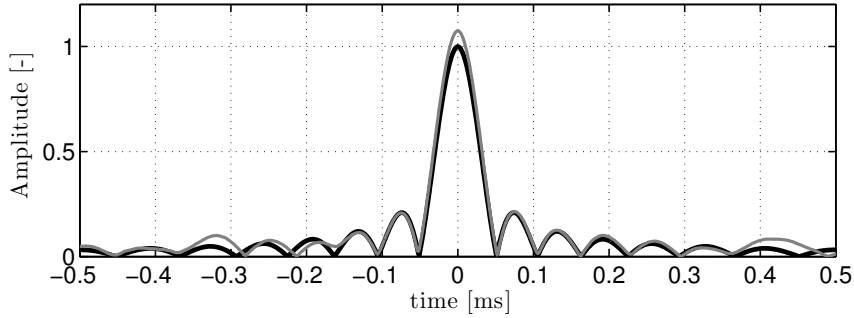


Figure 2.11 : Envelope of the auto-correlation function for $s_c(t)$ (black line) and the cross-correlation between $s_c(t)$ and $s_{cn}(t)$ (gray line).

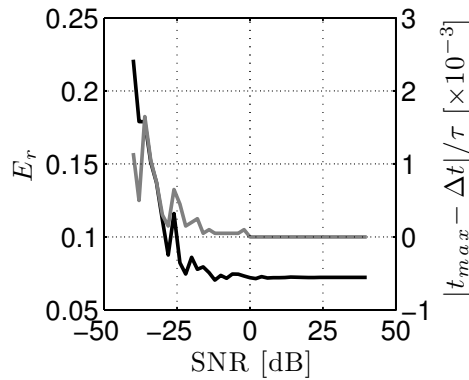


Figure 2.12 : Evolution of the error coefficient E_r indicated by the black line and the detection precision $|t_{max} - \Delta t|/\tau$ represented by the gray line with the signal to noise ratio (SNR).

Only Gaussian white noise is considered in the following tests.

Figure 2.10 shows a chirp signal ($s_c(t)$) and the corresponding signal with a 0 dB white gaussian noise. Introduction of noise results in a distorted chirp signal ($s_{cn}(t)$).

The envelope of the cross-correlation between $s_c(t)$ and $s_{cn}(t)$ is shown in Fig. 2.11. It features nearly the same shape as the auto-correlation of the

chirp $s_c(t)$ signal in the absence of noise. This example indicates that the cross-correlation technique enables to eliminate effects of noise. The performance can also be examined by plotting the evolution of the error coefficient E_r as a function of the signal to noise ratio SNR presented in Fig. 2.12. This figure clearly indicates that the error coefficient E_r decreases with the SNR. The cross-correlation performs well when $\text{SNR} \geq -20$ dB. The same result can also be found by plotting the detection precision $|t_{max} - \Delta t|/\tau$ as a function of the SNR which is also presented in Fig. 2.12.

2.4 Experimental detection system

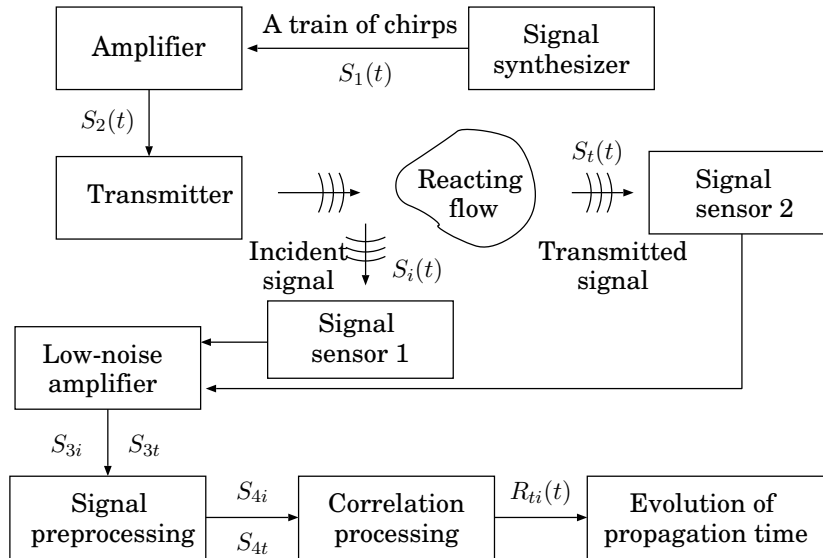


Figure 2.13 : Block diagram for the pulse compression generation and detection measurement chains.

Figure 2.13 presents a block diagram of the experimental setup used to generate ultrasonic chirps and detect their propagation time. The chirp signal $S_1(t)$, is synthesized by a wave generator, amplified and transmitted to space using a tweeter. The ultrasonic waves generated are measured with fixed microphones before (M1) and after (M2) their passage through the perturbed flow. These sound pressure signals ($S_i(t)$ and $S_t(t)$) are then amplified, high pass filtered and post-processed to compute the cross-correlation between the incident and transmitted sound waves. The sound travel time Δt is obtained from the envelope of the cross-correlation between $S_t(t)$ and $S_i(t)$.

2.4.1 Processing of the signals

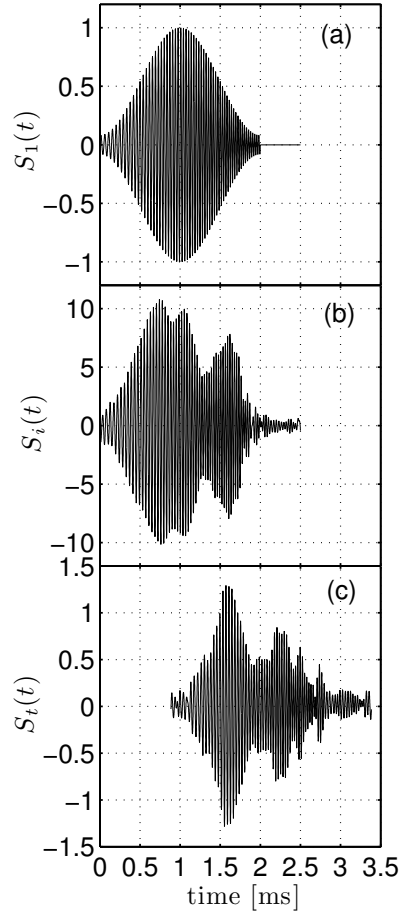


Figure 2.14 : Example of chirp record in the absence of flow, (a) signal from the signal synthesizer output, (b) signal recorded by M1, (c) signal recorded by M2.

Due to the different mechanical and electrical devices in the signal generation and reception, it is not desirable to operate with chirps with a square envelope because of the sudden changes in the signal amplitude at the leading and trailing edges of the sequence. A Hamming window is then applied to the rectangular chirp produced by the signal synthesizer to obtain a smooth transition in amplitude at the beginning and end of the chirp, but the response measured by the different sensors is still distorted as shown for example in Fig. 2.14 for a case in the absence of flow between the emitter and receiver. Figure 2.15 shows the envelope (E_{ii}) of the auto-correlation of the incident signal $S_i(t)$ and the envelope (E_{ti}) of the cross-correlation between $S_t(t)$ and $S_i(t)$. The sound travel

time Δt is determined by the difference between the positions of the main peaks of the two envelopes. Post-processing of measurements not presented here show that the main peak of the envelope of the autocorrelation function E_{ii} from the incident signal always remains at the same location and indicates the value 0. Therefore, change of the sound travel time in the experiments conducted in this work will be only determined from variations of E_{ti} . This simplified method may introduce a small bias in the determination of sound travel time and lead to larger uncertainties, but these effects remain limited since we are only interested in fluctuations of the sound travel time and not in the exact value of this travel time. To simplify the processing, the difference between the position of the main peak of the envelope E_{ti} and value 0 is considered as the sound travel time Δt , which is for example shown in Fig. 2.17. The precision of the measurement is indicated by the width of the main lobe.

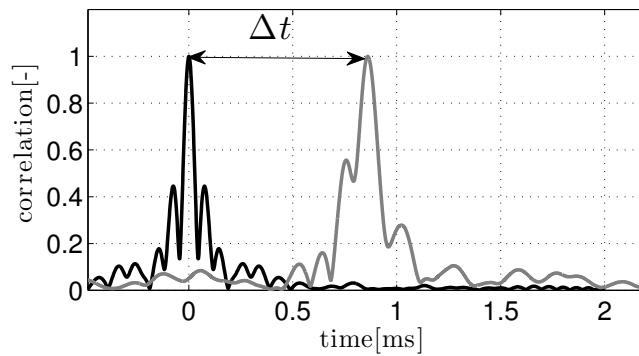


Figure 2.15 : *Envelopes of auto-correlation of signal $S_i(t)$ (black line) and cross-correlation between signals $S_t(t)$ and $S_i(t)$ (gray line).*

To reduce the width of the lobe, a pre-processing is applied to these raw signals. The technique is the same for the incident and transmitted signals and will only be described for the reference microphone M1 in Fig. 2.16. The raw signal is first filtered with a high pass zero-phase shift filter to eliminate the low frequency background noise induced by the flow and the ultrasound generation and measurement devices. The filtered result $S_3^a(t)$ is shown in Fig. 2.16(a). A digital Butterworth filter with a cut-off frequency $f=100$ Hz featuring an attenuation of less than 3 dB in the pass-band and at least 30 dB in the stop-band is used (Oppenheim and Schafer 1975). This filtered signal $S_3^a(t)$ and the signal generated by the synthesizer $S_1(t)$ are processed by the cross-correlation algorithm to locate the leading edge of the chirp. The resulting signal is multiplied by a rectangular box function of duration τ to eliminate the signal outside the chirp and obtain $S_3^b(t)$ as shown in Fig. 2.16(b). A Hilbert transform presented in Chapter 1 is then used to obtain the envelope of the signal $S_3^c(t)$, shown

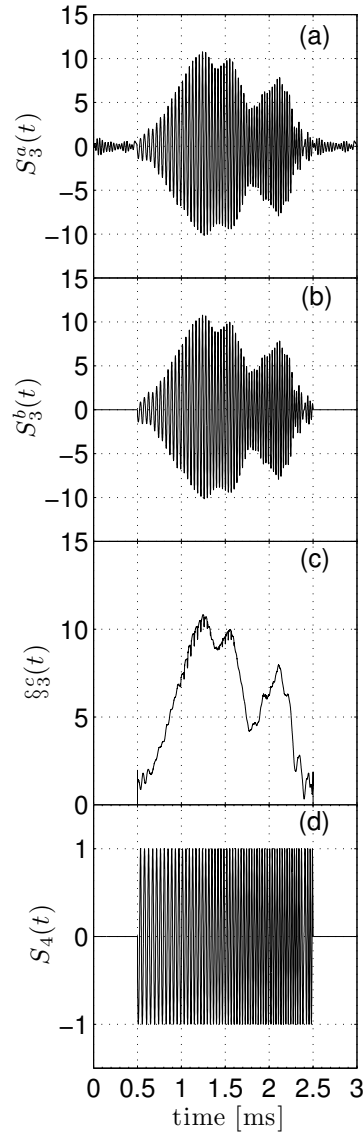


Figure 2.16 : *Pre-processing of signal measured by M1. (a) high pass filtered signal; (b) output of the multiplication between the filtered signal and the rectangular box function; (c) envelope of the signal; (d) normalized signal.*

in Fig. 2.16(c). This envelope enables to renormalize the signal $S_3^b(t)$ presented in Fig. 2.16(b) and obtain a constant amplitude signal $S_4(t)$ as shown in Fig. 2.16(d). The pre-processed signals from microphones M1 and M2 are then cross-correlated. The output $R_{ti}(t)$ is again processed by the Hilbert transform to keep only the envelope. The location of the peak of the main lobe yields the propagation time Δt .

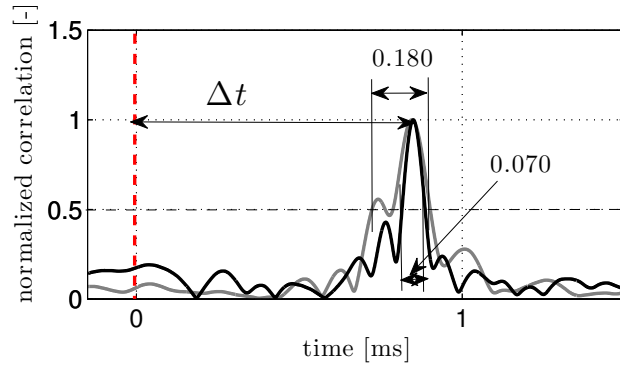


Figure 2.17 : Comparison of the envelopes of the cross-correlations function with (black line) and without pre-processing (gray line).

Figure 2.17 shows an example of the cross-correlation obtained with and without pre-processing. In this case, the sound travel times determined without and with pre-processing are 0.850 ± 0.090 ms and 0.850 ± 0.035 ms respectively. The precision of the detection is represented by the width of the main lobe at half its maximum value. The pre-processing slightly improves the precision of detection technique.

2.4.2 Parameters optimization for the chirp generation

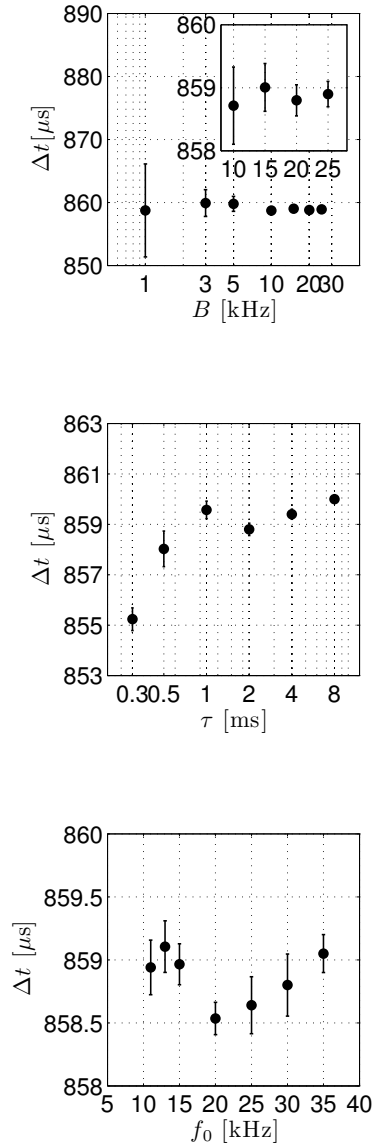


Figure 2.18 : Effects of the chirp parameters on the determination of the sound travel time Δt . Effect of the frequency bandwidth B (top), chirp duration τ (middle) and carrier frequency f_0 (bottom). See Tab. 2.1 for values of the remaining parameters. The distance between the transmitter and receiver is $L = 300$ mm. The speed of sound at ambient conditions is $c_o = 348 \text{ m} \cdot \text{s}^{-1}$. Theoretically, the sound travel time is $\Delta t_{th} = 860 \mu\text{s}$ in this case.

Table 2.1 : *Configurations tested for the chirp generation.*

Case	B [kHz]	τ [ms]	f_0 [kHz]
Effect of B	1- 25	2	30
Effect of τ	20	0.3 - 8	30
Effect of f_0	20	2	11 - 35

Different tests are conducted in the absence of flow and flame to optimize the technique for the generation and detection of the chirp ultrasonic signals. The influence of the frequency bandwidth B , carrier frequency f_0 , chirp duration τ and chirp repetition rate t_r on the precision of the measured sound travel time Δt is analyzed in this section. To avoid mixing different neighbor transmitted signals, the duration between two pulses $t_r - \tau$ must be larger than the fluctuations of propagation time Δt . It was checked that results in these conditions are independent on the repetition rate t_r . The range explored for the values of the three remaining parameters is synthesized in Tab. 2.1. The influence of each parameter is studied separately by keeping the two others fixed. In these experiments, the signals from the microphones are sampled at a frequency $f_s = 2^{21}$ Hz over a duration 0.2 s. Measurements are repeated 100 times for each case explored to obtain the confidence interval of the samples.

The measured sound travel times are plotted as a function of the frequency bandwidth B , pulse duration τ and carrier frequency f_0 in Fig. 2.18. In these plots, error bars correspond to the maximal deviation over 100 repetitions and the black disks denote the mean value. Increasing the frequency bandwidth B or pulse duration τ greatly improves the precision in Fig. 2.18 (top and middle figures). The choice of the pulse duration is however limited when time resolved data are needed. For example, to obtain time resolved information with a sampling rate of 500 Hz, τ has to be less than 2 ms. Theoretically, the carrier frequency f_0 has no effect on the precision as shown in section 2.3.2. Figure 2.18 (bottom figure) shows however that results feature some scatter depending on f_0 . This phenomenon is again induced by the different mechanical and electronic responses of the transmitter and receiver measurement chains. The parameters chosen for the chirp generation in the remaining experiments presented in this work were fixed to the optimal values indicated in Tab. 2.2.

Table 2.2 : *Optimized values for the chirp parameters.*

	f_i [kHz]	B [kHz]	τ [ms]	t_r [ms]
unconfined flames	20	20	2	2.5
partially confined flames	20	20	0.8	1.0

2.5 Conclusion

A detection technique often used in radar, sonar and medical imaging is employed here to measure the travel time of ultrasonic waves through a flow. The choice of the type of ultrasonic signals to probe the flow and its conditioning were discussed. Sequences of pulses constituted by harmonic waves with a linear frequency modulation associated with a cross-correlation procedure were shown to yield reliable results to measure the sound travel time in the absence of flame and flow. Each sequence, called a “chirp” is characterized by four parameters, a frequency bandwidth B , a pulse duration τ , a carrier frequency f_0 and a repetition time t_r . Effects of these parameters on accuracy and precision of the sound travel time detection technique were characterized. Increasing the frequency bandwidth and pulse duration greatly improves the precision as $1/(B\tau)$. The carrier ultrasonic frequency f_0 barely modifies the results. The cross-correlation technique enables to remove noise even at moderate signal to noise ratios. Finally, a pre-processing technique based on a renormalization of the measured signals was proposed to further improve the precision on the sound travel time. These techniques are used in the next chapters to probe reacting flows and infer modifications induced on the sound propagation time.

Chapter 3

Determination of heat release rate disturbances in the absence of external forcing

The acoustic method described in Chapter 2 is considered to detect fluctuations of sound travel time $\Delta t'$ of ultrasonic waves traveling through laminar premixed conical flames in the absence of external flow modulation. This information is used to reconstruct low frequency heat release rate disturbances \dot{Q}' which are driven by buoyancy forces. This phenomenon called “flickering” is associated with the Kelvin-Helmholtz instability due to the interaction between accelerating hot burned gases and cold ambient air at rest. This flow instability produces small heat release perturbations with typical frequencies around 10 to 20 Hz at ground level gravity and provides a generic configuration to validate our acoustic methodology for heat release rate reconstruction in the absence of external forcing device. A theoretical link between the rate of change in sound travel time $d\Delta t/dt$ for ultrasonic waves crossing the flame and fluctuations in heat release rate \dot{Q}' is established. The experimental configuration investigated is then detailed and validation of the acoustic methodology in non-reacting conditions is conducted. Experimental results with laminar conical flames are then compared to theoretical estimates and measurements obtained with an optical technique.

3.1 Theoretical analysis

The following analysis is restricted to laminar premixed conical flames characterized by a “flickering” of the flame tip induced by buoyancy forces acting on the hot burned gases forming the plume surrounding the flame (Durox et al. 1990; Kostiuik and Cheng 1995). These low frequency oscillations are induced

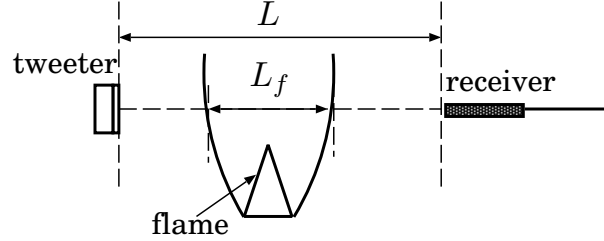


Figure 3.1 : Schematic of the configuration investigated. A sound wave generated by an ultrasonic emitter propagates through ambient air, burned gases before reaching a receiver. The distance between the emitter and receiver is L . Waves propagate through the burned gases over a distance L_f .

by flow perturbations featuring a wavelength large compared to the flame thickness. It is then possible to treat the flame as a thin interface separating the reactive mixture from the combustion products. Using this model, the flame front propagates with the laminar burning velocity S_L and stretch as well as curvature effects are neglected here. Successive approximations are made to obtain an analytical expression of heat release rate disturbances as a function of sound travel time perturbations of ultrasonic waves crossing the flame. These developments offer a simple theoretical framework to analyze effects of the different flow parameters controlling changes in the sound travel time induced by flickering. This is used in the next section to validate the proposed technique by comparisons between predictions and measurements. This analysis is then completed by an independent experimental validation based on an optical technique.

As demonstrated in Chapter 2, the envisaged experimental configuration can be simplified to that presented in Fig. 3.1 where the acoustic path crosses the burned gases characterized by a speed of sound c_b which are surrounded by fresh air with a speed of sound c_u . The motion induced by flame flickering results in turn in small perturbations in the heat release rate and in fluctuations of the volume of the burned gases produced. Consequently the length of the burned gases L_f and sound travel time Δt are modified as described in Chapter 2 (Eq. (2.3)). The link between fluctuations in the sound travel time $\Delta t'$ and perturbations in the heat release rate \dot{Q}' is analyzed in this section. The main steps of the derivation are presented below by assuming that the volume of the burned gases V_b depends on the flame surface area A_f of the conical flame:

$$V_b = \varpi L_f A_f \quad (3.1)$$

where L_f is the apparent dimension of the burned gases in the line of sight of the emitter and receiver and ϖ denotes a constant coefficient for fixed flow operating conditions and experimental arrangement. Since the flame is anchored

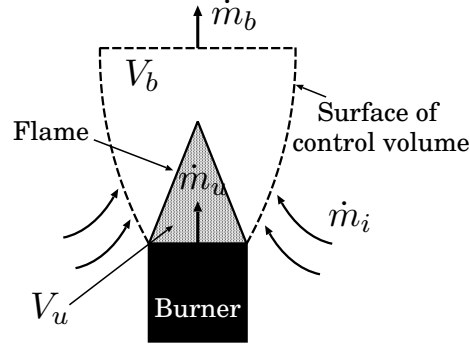


Figure 3.2 : Control volume divided in two parts by the flame: unburned gases (volume V_u and mass flowrate \dot{m}_u) and burned gases (volume V_b and mass flowrate \dot{m}_b).

at the burner rim, a mass balance between the burner outlet and the flame front yields $v_u A = S_L A_f$, where S_L is the laminar burning velocity, v_u the flow velocity at the burner outlet and A the cross section area of the burner outlet. This yields an expression for the hot plume width L_f as a function of the burned gases volume:

$$L_f = \frac{S_L}{\varpi v_u A} V_b \quad (3.2)$$

In this expression, S_L only depends on the equivalence ratio, v_u is kept constant and ϖ is time independent so that L_f can be substituted in Eq. (2.3) to yield

$$\Delta t' = -\frac{S_L}{\varpi v_u A c^*} V_b' \quad (3.3)$$

where $c^* = c_u c_b / (c_b - c_u)$ is the equivalent speed of sound.

Fluctuations in the travel time of ultrasonic waves are proportional to fluctuations in the volume of burned gases V_b' . The objective is now to describe the fluctuations of the burned gases volume as a function of heat release rate disturbances.

For an unconfined flame and buoyancy driven oscillations, the flow can be considered isobaric. Using the simplified model presented in Fig. 3.2, a global energy balance over the control volume yields:

$$\frac{\gamma p}{\gamma - 1} \left(\frac{\partial V_u}{\partial t} + \frac{\partial V_b}{\partial t} \right) = \dot{m}_u c_p T_u - \dot{m}_b c_p T_b + \dot{Q} \quad (3.4)$$

where the lateral surface of the control volume in contact with ambient air is supposed impermeable ($\dot{m}_i = 0$) and adiabatic ($\dot{Q}_i = 0$). The ratio of specific heat capacity $\gamma = c_p / c_v$ and ambient pressure p appear on the left side of

Eq. (3.4). The rate of heat released in the control volume \dot{Q} and the sensible enthalpy fluxes $\dot{m}c_pT$ at the unburned (subscript u) and burned (subscript b) limits are responsible for changes in the unburned V_u and burned V_b volumes. In these expressions, T is the temperature and \dot{m} denotes the mass flow rate. Assuming the absence of mass accumulation in the system at low frequency, a first order perturbation analysis of Eq. (3.4) yields:

$$\frac{\gamma p}{\gamma - 1} \frac{\partial V_b'}{\partial t} = \dot{Q}' \quad (3.5)$$

where fluctuations in the fresh reactants volume were neglected since $V_u/V_b \approx \rho_b/\rho_u = T_u/T_b \ll 1$. For methane-air flames the temperature ratio reaches $T_b/T_u \simeq 4 - 8$ depending on the mixture equivalence ratio ϕ .

Combining Eqs. (3.3) and (3.5), one finally finds that heat release rate disturbances induced by buoyancy effects are proportional to the rate of change in the sound travel time between the transmitter and receiver:

$$\dot{Q}' = -\frac{\gamma p}{\gamma - 1} \frac{\varpi v_u A c^*}{S_L} \frac{\partial \Delta t}{\partial t} \quad (3.6)$$

This last relation shows that it is possible to estimate heat release rate perturbations induced by flame flickering from fluctuations in the sound propagation time of ultrasonic waves crossing the hot plume of premixed flames stabilized on a burner. Heat release rate disturbances are then proportional to the time rate of change of the sound travel time $\partial \Delta t / \partial t \propto \dot{Q}'$. The remaining part of this chapter is devoted to validation of Eq. (3.6).

3.2 Experimental configuration

The experimental setup is presented in Fig. 3.3. Laminar conical premixed methane-air flames are anchored at the burner rim. Ultrasonic pulses transmitted to air are generated by a tweeter placed on one side of the setup. The acoustic waves are recorded by two microphones M1 and M2 before and after their passage through (a) a flame or (b) the corresponding jet flow in the absence of combustion. These microphones are aligned so that ultrasonic waves cross the burner on its symmetry axis. A photomultiplier (PM) is also placed on the side of the burner to record the chemiluminescence from intermediate radicals present within the flame front.

3.3 Validation without flame

The transmission of sound waves between microphones M1 and M2 under non-reacting conditions is now investigated. Experiments are conducted for three

CHAP. 3 - DETERMINATION OF HEAT RELEASE RATE DISTURBANCES IN THE ABSENCE OF EXTERNAL FORCING 61

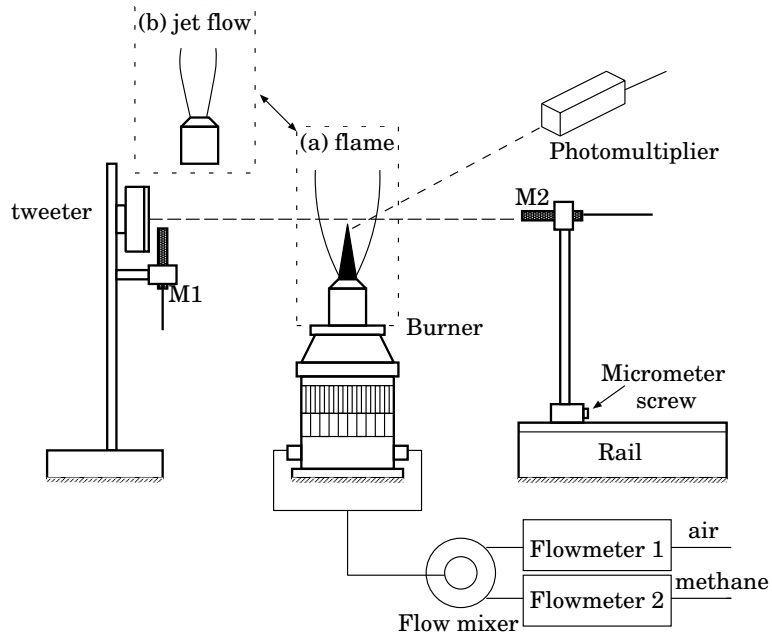


Figure 3.3 : Schematic view of the experimental setup.

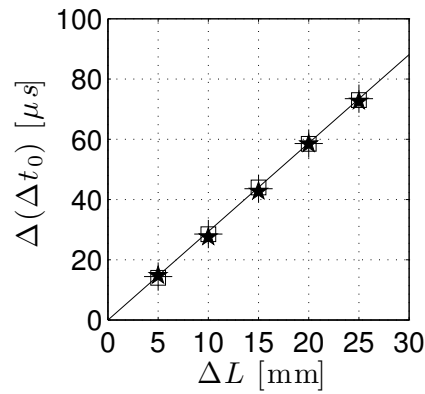


Figure 3.4 : Evolution of the sound travel time difference $\Delta(\Delta t_0) = \Delta t_0(L) - \Delta t_0(L_0)$ with the distance $\Delta L = L - L_0$. The solid line indicates theoretical predictions deduced from Eq. (2.2). Markers denote measures in the absence of burner (\square), with burner ($+$), and for a non-reacting jet flow ($*$).

different cases, (a) in the absence of burner, (b) with the burner between the two microphones but in the absence of flow, and (c) for a non-reacting jet flow (Fig. 3.3). The non-reacting flow condition explored features a Reynolds number based on the flow velocity and the nozzle diameter equal to $Re = 2900$. This corresponds to a laminar jet with a flow velocity typical of the reacting conditions explored in the next section. Parameters used to generate the chirp are listed in Tab. 2.2. Microphones signals are sampled here at a frequency $f_s = 2^{21}$ Hz during a period of 0.2 s. This duration is long enough to collect 80 transmitted chirps for each record.

By modifying the horizontal position of M2 (Fig. 3.3), it is possible to determine the evolution of the travel time of ultrasonic waves Δt_0 as a function of the distance L between the two microphones. In these experiments, the horizontal distance between the two microphones is increased by steps of 5 mm to record the different sets of data. The evolution of the difference $\Delta(\Delta t_0) = \Delta t_0(L) - \Delta t_0(L_0)$ between measurements of the sound travel time recorded for two distances L and L_0 between microphones M1 and M2 is plotted in Fig. 3.4 as a function of the distance $\Delta L = L - L_0$, where the reference distance corresponds to $L_0 = 300$ mm. The difference in sound travel time $\Delta(\Delta t_0)$ increases linearly with ΔL for all cases explored. All data collapse on the same line indicating that there is no scattering effect due to the presence of the burner or the laminar jet. The slope $1/c_0$ fits with predictions from Eq. (2.2), where $c_0 = 338 \text{ m}\cdot\text{s}^{-1}$ is the speed of the sound in ambient air. This setup and the methodology developed can now be used to examine perturbations in the sound travel time induced by the presence of the flame between the two microphones.

3.4 Validation with flame

Laminar premixed conical flames are stabilized on the burner rim. As already discussed in the previous sections, while the flow at the burner outlet is steady, the tip of the conical flame features a small regular oscillation called flickering caused by the unstable interface between the burned gases and ambient air (Fig. 3.5, left image). It is also known that a cylindrical tube on the top of the flame stabilizes the flow of the burned gases and the flickering phenomenon is attenuated (Kizirnis et al. 1984; Linteris and Rafferty 2008). This is illustrated in the right image in Fig. 3.5. Flickering features typical frequencies around 10 to 20 Hz at ground level (Kostiuk and Cheng 1994; Durox et al. 1997b). This motion generates in turn small low frequency perturbations in the heat release rate that can be identified by measuring fluctuations in the light emission intensity I recorded by a photomultiplier PM or by determining fluctuations in

CHAP. 3 - DETERMINATION OF HEAT RELEASE RATE DISTURBANCES IN THE ABSENCE OF EXTERNAL FORCING 63

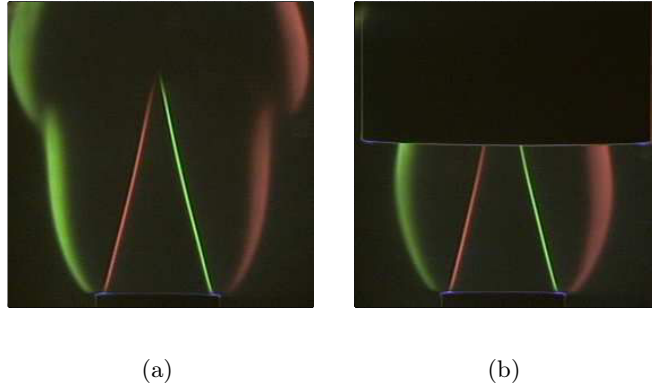


Figure 3.5 : Color Schlieren images of a methane-air premixed flame ($\phi = 0.90$, $v_u = 1.50 \text{ m} \cdot \text{s}^{-1}$) with (a) and without (b) a quartz tube on the top of the flame.

the sound travel time Δt between the microphones M1 and M2.

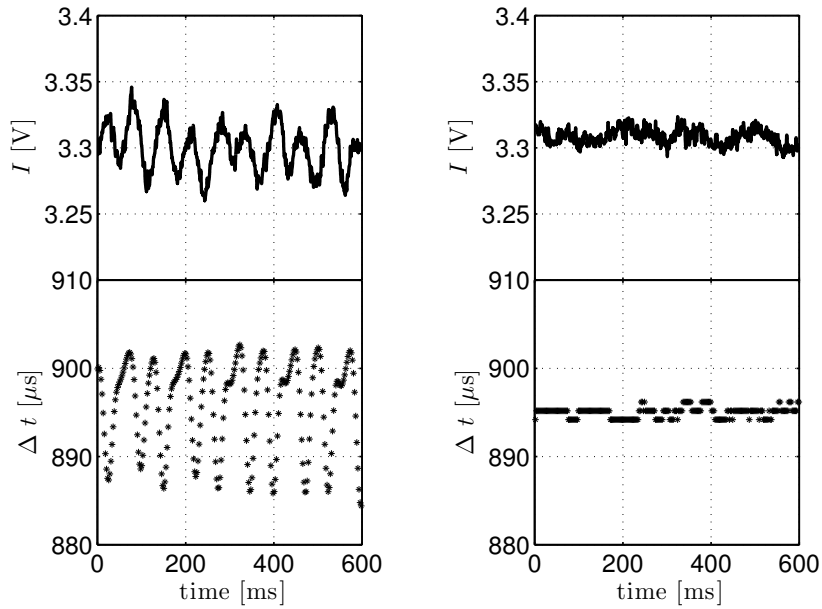


Figure 3.6 : Light emission (top) and sound propagation time (bottom) across a methane-air premixed flame ($\phi = 0.90$, $v_u = 1.50 \text{ m} \cdot \text{s}^{-1}$) with (left figure) and without flickering (right figure).

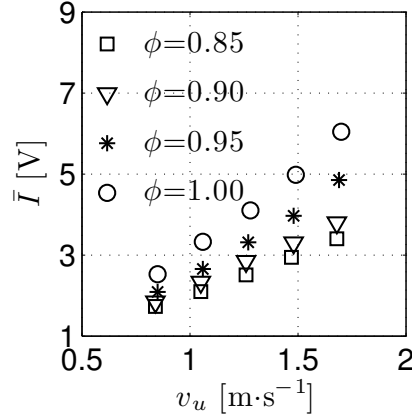


Figure 3.7 : Evolution of the mean flame emission intensity \bar{I} as a function of the flow velocity v_u for different equivalence ratios ϕ .

Measurements are shown for a lean methane-air flame with a bulk velocity $v_u=1.5 \text{ m}\cdot\text{s}^{-1}$ and equivalence ratio $\phi = 0.9$ with and without the quartz tube on the top of the flame. Signals are recorded here with the same sampling frequency $f_s = 2^{11} \text{ Hz}$ but over a longer sampling time 1.5 s than in the experiments in the absence of combustion. The left graph in Fig. 3.6 shows that the light intensity $I(t)$ and sound travel time Δt both feature a periodic motion. Power spectral analysis based on the data collected with the PM and the microphones show that the main peak in both cases corresponds to the oscillation frequency $f = 16 \pm 1 \text{ Hz}$. These measurements are in agreement with the flickering frequency deduced from the correlation of Kostiuk and Cheng (1994):

$$\frac{f^2 D}{g\xi(\xi - 1)} = 0.00028 \left(\frac{v_u D}{\xi \nu} \right)^{2/3} \quad (3.7)$$

By taking $D = 20 \text{ mm}$ for the diameter of the burner outlet, $g = 9.8 \text{ m}\cdot\text{s}^{-2}$ for the gravitational acceleration, $\xi = T_b/T_u = 7$ for the volumetric expansion ratio and $\nu = 1.5 \times 10^{-5} \text{ m}^2\cdot\text{s}^{-1}$ for the kinematic viscosity in the fresh reactants at room temperature, one also finds $f = 16 \text{ Hz}$. This confirms that the two previous techniques highlight the same unsteady behavior induced by flame flickering. Results presented on the right in Fig. 3.6 clearly demonstrate that fluctuations in the light intensity I and travel time of ultrasonic waves Δt vanish when the quartz tube is used.

Fluctuations in the chemiluminescence emission intensity I and disturbances in the sound travel time Δt result both from heat release rate perturbations. The link between these quantities is obtained by plotting the evolution of the

Table 3.1 : Inlet flow velocity v_u and equivalence ratio ϕ used for the six configurations explored denoted by C_i where $i=1, \dots, 6$. The measured value of the coefficient Ξ is also indicated together with the corresponding value of the linear regression factor r^2 .

Case	C1	C2	C3	C4	C5	C6
ϕ	0.85	0.85	0.85	0.90	0.95	1.0
v_u [m·s ⁻¹]	0.84	1.24	1.68	0.84	0.84	0.84
Ξ [V ⁻¹]	-0.0213	-0.0151	-0.0108	-0.0137	0.0125	-0.0107
r^2	0.88	0.93	0.81	0.95	0.87	0.92

mean value of the light intensity \bar{I} as a function of the flow velocity v_u at the burner outlet. Results are presented in Fig. 3.7 for four flames featuring different equivalence ratios $\phi = 0.85, 0.90, 0.95$ and 1.00 . The evolution is linear $\bar{I} = \epsilon v_u$, where the coefficient ϵ depends on the equivalence ratio of the combustible mixture. It is then possible to obtain an expression for the coefficient k appearing in Eq. (1.9) in Chapter 1 linking the heat release rate \bar{Q} and the chemiluminescence intensity \bar{I} :

$$k = \frac{\bar{Q}}{\bar{I}} = \frac{\bar{Q}}{\epsilon v_u} = \frac{\rho_u \Delta q A}{\epsilon} \quad (3.8)$$

where ρ_u is the unburned mixture density, A the cross section area at the burner outlet Δq the heating value per unit mass of reactive mixture. In this expression, it is assumed that all the mixture is burned. Combining Eqs. (3.6) and (3.8), the following relation between perturbations in chemiluminescence intensity I and sound travel time Δt can be derived:

$$\frac{d\Delta t}{dt} = \Xi I' \quad \text{where} \quad \Xi = -\frac{(\gamma - 1) S_L \Delta q}{\varpi \epsilon v_u c_u^2 c^*} \frac{1}{c^*} \quad (3.9)$$

For a fixed mixture composition and flow velocity, fluctuations in the flame emission are proportional to the rate of change of the sound travel time of acoustic waves crossing the flame.

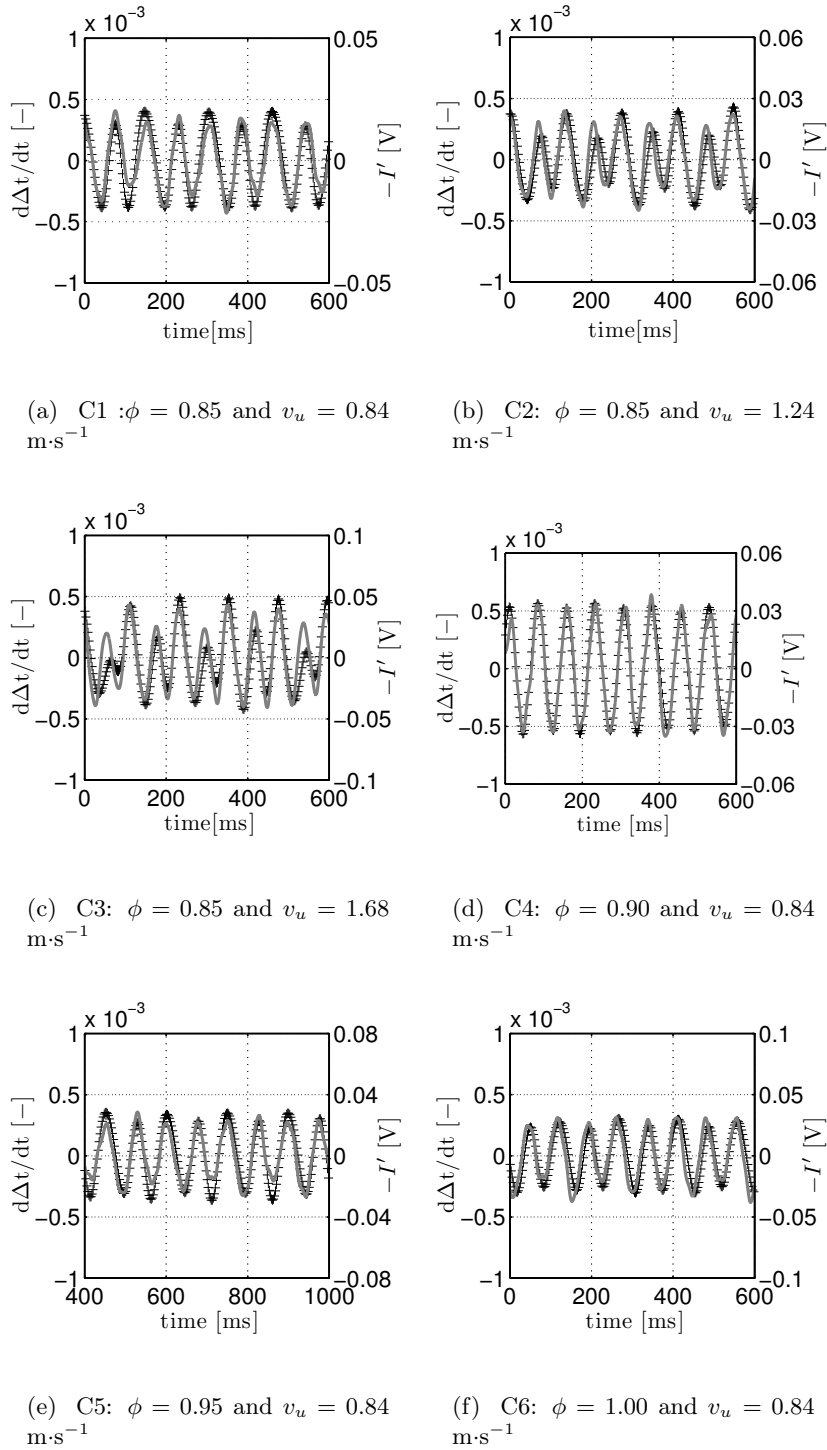


Figure 3.8 : Simultaneous records of chemiluminescence intensity perturbations $-I'$ (solid line) and disturbances in the rate of change of the sound travel $d\Delta t/dt$ (+).

Table 3.2 : Numerical values used to estimate the coefficient Ξ appearing in Eq. (3.9).

ϕ	S_L [m·s ⁻¹]	c_u [m·s ⁻¹]	c_b [m·s ⁻¹]	Δq [kJ·kg ⁻¹]	ϵ [V·s·m ⁻¹]	ϖ
0.85	0.31	343	797	1740	1.99	0.1
0.90	0.34	343	809	1810	2.27	0.1
0.95	0.37	343	821	1870	3.20	0.1
1.00	0.38	343	834	1930	4.08	0.1

Measurements of $d\Delta t/dt$ and I' are conducted for lean premixed methane-air flames featuring different inlet flow velocities ranging from $v_u = 0.84$ to 1.68 m·s⁻¹ and equivalence ratios ϕ varying from 0.85 to 1.00. Parameters fixed for the chirp generation are indicated in Tab. 2.2. Acoustic measurements are sampled at a frequency equal to 400 Hz corresponding to a repetition time $t_r = 2.5$ ms. The resulting signal for $\Delta t'$ is then filtered by a low-pass zero-phase shift filter with a cut-off frequency equal to 40 Hz. The chemiluminescence intensity I measured by PM is sampled at a frequency of 8192 Hz during a period of 1.5 s and is filtered with the same low pass filter. Comparisons between data obtained with the two techniques are presented in Fig. 3.8 for the six cases listed in Tab. 3.1. The opposite signal $-I'$ is plotted in this figure because the proportionality coefficient Ξ between I' and $d\Delta t'/dt$ given by Eq. (3.9) is negative. Signals are also rescaled in this figure to obtain comparable oscillations levels. The two signals $d\Delta t/dt$ and $-I'$ match well in phase and amplitude for all cases, clearly demonstrating that the rate of change of the sound travel time of ultrasonic waves is proportional to fluctuations in light intensity emission: $d\Delta t/dt \propto I'$.

It is also interesting to plot $d\Delta t/dt$ as a function of I' for the different operating conditions explored. One example is presented in Fig. 3.9 for the case C2 (see Tab. 3.1). The value of the coefficient Ξ appearing in Eq. (3.9) can then be determined by a linear regression. These values and the corresponding regression coefficients r^2 are indicated in Tab. 3.1 and confirm the linear link between $d\Delta t/dt$ and I' for all cases explored. Data determined experimentally can also be compared to predictions using values indicated in Tab. 3.2 to estimate the coefficient Ξ appearing in Eq. (3.9). Predictions are plotted in Fig. 3.10 and are compared to measurements for two different equivalence ratios $\phi = 0.85$ and $\phi = 1.00$ as a function of the nozzle outlet flow velocity v_u . The distributions of experimental results match well with predictions confirming the validity of Eq. (3.9) and the possibility to detect heat release rate fluctuations by measuring perturbations in the transmission of ultrasonic waves crossing flames.

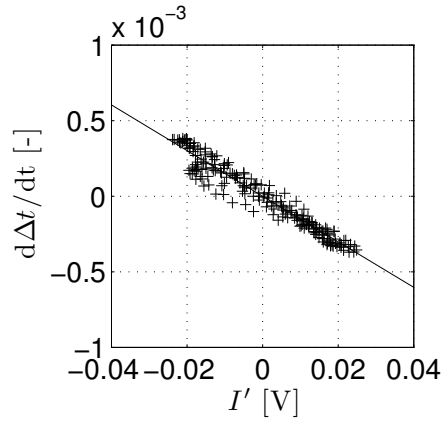


Figure 3.9 : Plot of the rate of change of travel time of ultrasonic waves $d\Delta t/dt$ as a function of fluctuation in light intensity I' emitted by the flame . Flame C2: $\phi = 0.85$ and $v_u = 1.24 \text{ m} \cdot \text{s}^{-1}$.

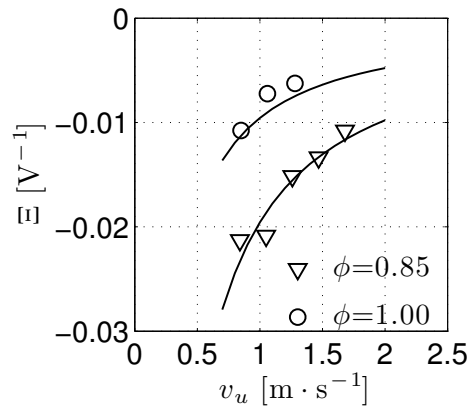


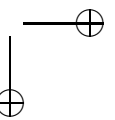
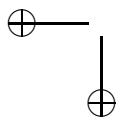
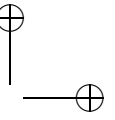
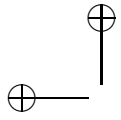
Figure 3.10 : Comparison between measurements and predictions (solid line) for the coefficient Ξ for two equivalence ratios $\phi = 0.85$ (∇) and $\phi = 1.0$ (\circ) as function of the flow velocity v_u .

3.5 Conclusion

Disturbances in the travel time of ultrasonic waves have been successfully used to detect small heat release rate disturbances due to flickering in premixed laminar conical flames. An experimental validation of the proposed technique was conducted on a generic configuration with a tweeter to produce the ultrasonic waves and two microphones to record the incident and transmitted signals through different laminar premixed conical flames. An analytical relation was derived linking sound travel time and heat release rate disturbances. Time re-

**CHAP. 3 - DETERMINATION OF HEAT RELEASE RATE DISTURBANCES IN THE ABSENCE OF
EXTERNAL FORCING** 69

solved measurements obtained with this acoustic method were compared with data obtained from records of the chemiluminescence emission from the flames. A good agreement was obtained for the different cases explored demonstrating that the transmission of ultrasonic waves can effectively be used to estimate heat release rate disturbances. It was also shown that the proposed technique is very sensitive to small disturbances in heat release rate. These results are encouraging and motivate its use to detect heat release rate disturbances when the flame is submitted to external flow modulations.



Chapter 4

Determination of heat release rate disturbances in pulsated flames

The flames investigated in this chapter are partially confined by a quartz tube placed on the top to eliminate buoyancy effects, and are submitted to upstream flow velocity modulation. A new link between resulting heat release rate fluctuations \dot{Q}' and the corresponding perturbations in the propagation time of ultrasonic waves $\Delta t'$ is established in these configurations. This link takes the form of a transfer function which depends on the flow operating conditions, flame aspect ratio and frequency. The experimental configuration used to validate the predictions is presented. Results deduced from acoustic measurements are compared to theoretical estimates and data obtained with the chemiluminescence emission.

4.1 Theoretical analysis

The following analysis is restricted to laminar premixed flames submitted to flow velocity modulations at a fixed equivalence ratio. The same type of approximations are made as in Chapter 3 to analyze the flame response and its interactions with sound waves.

Consider the schematic in Fig. 4.1, disturbances in heat release rate are induced by the modulation of the unburned gases velocity. The flame front is then wrinkling (r_i of the flame front fluctuates with respect to time) and the position r_o of the interface between the hot plume and ambient air is also perturbed. The length of acoustic path in the burned gases here corresponds to $L_f = 2(r_o - r_i)$. It is then possible to determine the perturbed length L_f' by examining the motion of the flame and burned gases interfaces r_i and r_o . Considering the

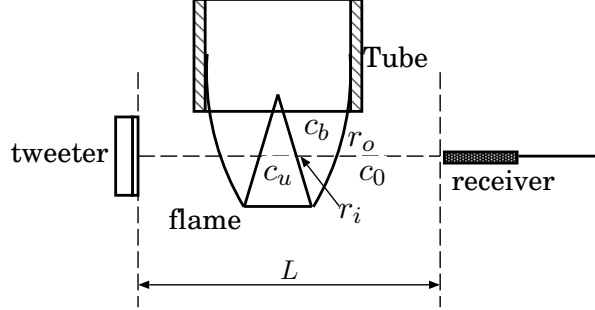


Figure 4.1 : *Experimental configuration investigated in this study. Ultrasonic waves cross three different media between the transmitter and the receiver: ambient air, burned gases and the fresh gas mixture.*

elementary control volume represented by the hatched area in Fig. 4.2, a mass balance is used to obtain the relationship between the flame radius r_i and the burned gases radius r_o at each instant t when the thickness dy along the axial direction is reduced to zero. A first order perturbation analysis is conducted by expanding instantaneous quantities $a(t)$ into their average over a period and a small disturbance $a(t) = \bar{a} + a'$ where $a'/\bar{a} \ll 1$. The mass balance for the steady flow yields:

$$\bar{\rho}_b \bar{v}_b (\bar{r}_o^2 - \bar{r}_i^2) - \bar{\rho}_u \bar{v}_u (R^2 - \bar{r}_i^2) = 0 \quad (4.1)$$

In this expression, the lateral surface of the shadow zone in contact with ambient air is supposed to be impermeable ($\dot{m}_i = 0$) as in chapter 3. The velocities v_u and v_b correspond to the axial components of the velocity field \mathbf{v} in the fresh mixture and burned gases characterized by the density ρ_u and ρ_b respectively. In the case of low frequency wrinkles along the flame front with a wavelength large compared to the thickness dy , these first-order disturbances obey to:

$$\bar{\rho}_b \bar{v}_b (\bar{r}_o r'_o - \bar{r}_i r'_i) + \bar{\rho}_u \bar{v}_u \bar{r}_i r'_i = 0 \quad (4.2)$$

This relation holds for small flow velocity disturbances $v'/\bar{v} \ll 1$ when density fluctuations in the fresh mixture and burned gases can be neglected. The relationship between the velocity in the fresh mixture and burned gases for a conical flame inclined with an angle α with respect to the flow direction is known as $\bar{v}_b/\bar{v}_u = 1 + (\bar{\rho}_u - \bar{\rho}_b)/\bar{\rho}_b \sin^2 \alpha$ (Searby 2008). It is then possible to use this expression to obtain the steady and first order approximation of the burned gases locations as a function of the flame positions:

$$\bar{r}_o^2 = \Gamma \bar{r}_i^2 + (1 - \Gamma) R^2 \quad \text{and} \quad r'_o = \Gamma \frac{\bar{r}_i}{\bar{r}_o} r'_i \quad (4.3)$$

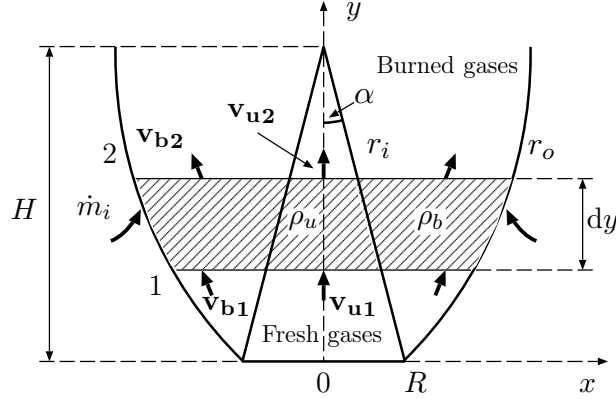


Figure 4.2 : Schematic representation of a laminar conical premixed flame surrounded by the burned gases and ambient air. The distance H indicates the flame height and α denotes half the angle of the flame cone.

where the dimensionless quantity $\Gamma = 1 - (\bar{\rho}_u/\bar{\rho}_b)[1 + (\bar{\rho}_u - \bar{\rho}_b)/\bar{\rho}_b \sin^2 \alpha]^{-1}$ is fixed for given flow operating conditions. For a conical flame, the mean flame radius \bar{r}_i is a linear function with respect to the axial distance y to the burner outlet:

$$\frac{\bar{r}_i}{R} = 1 - \frac{y}{R} \tan \alpha \quad (4.4)$$

where R is the burner radius. By combining this last relation with Eq. (4.3), one obtains an expression for the mean burned gases width $\bar{L}_f = c^*(\Delta t_0 - \bar{\Delta t}) = 2(\bar{r}_o - \bar{r}_i)$ as a function of the axial distance y , where c^* is the equivalent speed of sound as indicated in Chapter 2.

Figure 4.3 shows a comparison between predictions obtained from Eq. (4.3) and color Schlieren images for a laminar conical premixed flame in the absence of flow modulation. Red and green filters are used in these experiments to separate the light deflected in different horizontal directions and highlight the flame front (in red) from the limit of the hot plume (in green) (Ducruix et al. 2000). Preliminary experiments described in Chapter 3 showed a strong influence of buoyancy on the stability of the burned gases plume (Durox et al. 1997b) so that experiments are conducted with and without flame tube on the top of the burner to partially confine the flame and damp this phenomenon. A fairly good agreement between predictions and Schlieren images in Fig. 4.3 is obtained for heights limited to about $y \leq 20$ mm. Above this height buoyancy effects are more pronounced and modify the shape of the hot plume which is not well reproduced by the model. The cylindrical tube made of quartz is darkened in these experiments to avoid light deflection in this region. This tube enables here to limit buoyancy effects. It is in particular shown that this flame tube does not modify the expansion of the burned gases below $y \leq 20$ mm. The same type of

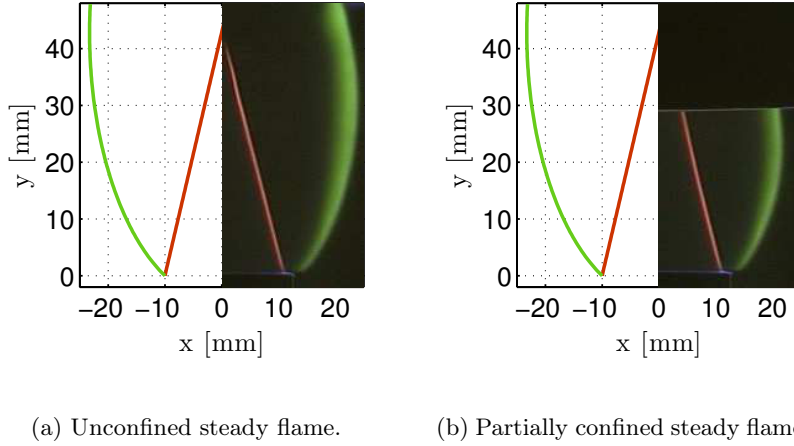


Figure 4.3 : Comparison between locations of the flame front radius r_i and the burned gases radius r_o obtained from Eq. (4.3) (left side) and Schlieren images in the absence of external modulation (right side). Flame FL1: $\phi = 0.90$, $\bar{v}_u = 1.5 \text{ m} \cdot \text{s}^{-1}$.

comparison is conducted when the incoming flow is perturbed in Fig. 4.4. Two snapshots of the instantaneous locations of the flame and burned gases interfaces during a modulation cycle are compared with predictions for two driving frequencies $f = 40 \text{ Hz}$ (Fig. 4.4(a) and (b)) and $f = 80 \text{ Hz}$ (Fig. 4.4(c) and (d)). The perturbation level $v_{urms}/\bar{v}_u = 0.07$, where v_{urms} denotes the root mean square velocity modulation measured at the burner outlet, is kept constant in these experiments. Predictions of the flame and burned gases motions are again in fairly good agreement with measurements for both modulation frequencies in the lower parts of the images when $y \leq 20 \text{ mm}$.

It is now necessary to have a model to describe the evolution of the flame front displacement as a function of the imposed velocity modulation. The solution of this problem has been examined in numerous studies (Baillot et al. 1992; Fleifil et al. 1996; Ducruix et al. 2000; Schuller et al. 2003). This can be modeled by a transport equation for the perturbed flame front position r'_i which is convected along the flame front by the mean flow velocity parallel to the flame front. In this description, perturbations in the flame position are generated by velocity disturbances normal to the mean flame front position and write:

$$\frac{\partial r'_i}{\partial t} + \bar{v}_u \cos^2 \alpha \frac{\partial r'_i}{\partial y} = v'_u \tan \alpha \quad (4.5)$$

Flow perturbations generated at the burner outlet are transported by the mean flow and can be well described by a convective wave along the axial direction

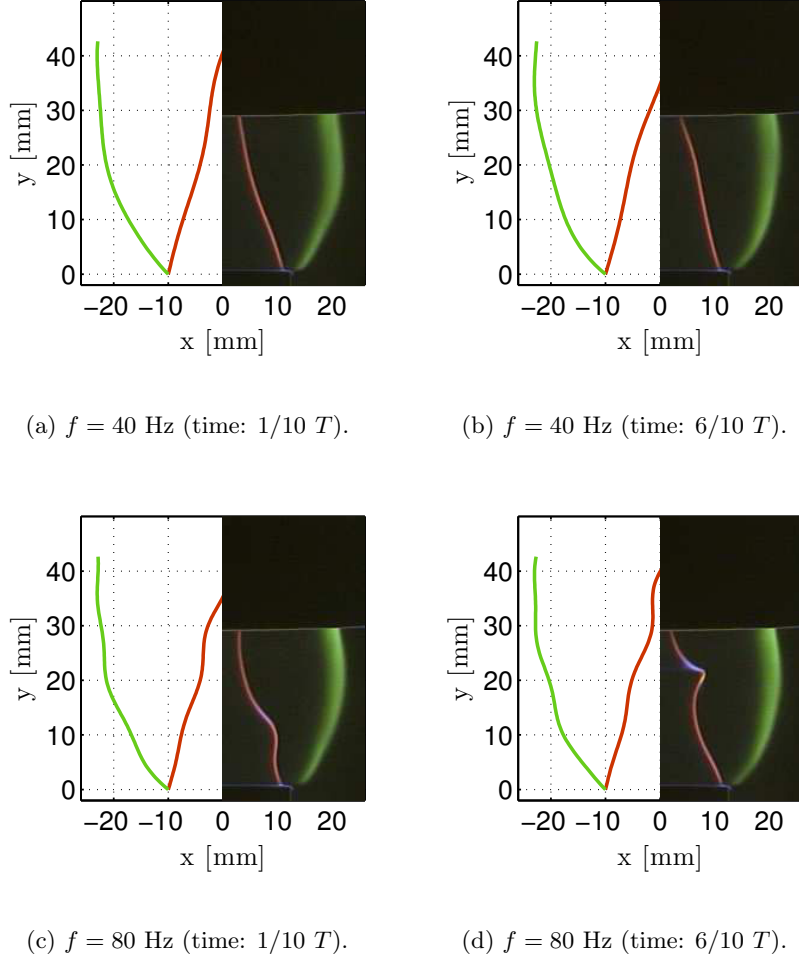


Figure 4.4 : Comparison between locations of the flame front radius r_i and the burned gases radius r_o obtained from Eq. (4.3) (left side) and Schlieren images of the flame (right side) when the flow is modulated at $f = 40$ Hz ((a) and (b)) and 80 Hz ((c) and (d)) at a fixed perturbation level $v_{u,rms}/\bar{v}_u = 0.07$. Flame FL1: $\phi = 0.90$, $\bar{v}_u = 1.5 \text{ m} \cdot \text{s}^{-1}$. Two instants are represented in the modulation cycle: $1/10 T$ and $6/10 T$, where T is the forcing period.

$v'_u(y, t) = \tilde{v}_u \exp(iky - i\omega t)$ when the flow is modulated harmonically (Baillot et al. 1992; Baillot et al. 1996; Schuller et al. 2002a; Birbaud et al. 2006). In this expression the convective wave number $k = \omega/\bar{v}_u$ is based on the mean value of the flow velocity \bar{v}_u and $\omega = 2\pi f$ denotes the angular frequency. The response of the flame front displacement r_i is also harmonic and writes $r_i(y, t) = \tilde{r}_i(y) \exp(-i\omega t)$. By injecting these expressions in Eq. (4.5), one finds

(Schuller et al. 2003):

$$\tilde{r}_i(y) = \frac{\tilde{v}_u}{\bar{v}_u} \frac{1}{ik \sin \alpha \cos \alpha} \left[\exp\left(\frac{iky}{\cos^2 \alpha}\right) - \exp(iky) \right] \quad (4.6)$$

The heat release rate is given by $\dot{Q} = \int \rho_u S_L \Delta q dA$, where Δq is the heat value per unit mass of mixture. For well premixed flames at a fixed equivalence ratio, heat release rate perturbations are only a function of flame surface area disturbances $A' = \tilde{A} \exp(-i\omega t)$ (Schuller et al. 2002b; Candel et al. 2004). By integrating the above expression along the flame front and neglecting the motion at the flame root, it finally comes (Schuller et al. 2003):

$$\frac{\tilde{\dot{Q}}}{\bar{\dot{Q}}} = \frac{\tilde{A}}{\bar{A}} = \frac{\tilde{v}_u}{\bar{v}_u} \frac{2}{\omega_*^2} \frac{1}{1 - \cos^2 \alpha} \left[1 - \exp(i\omega_*) + \frac{\exp(i\omega_* \cos^2 \alpha) - 1}{\cos^2 \alpha} \right] \quad (4.7)$$

where $\omega_* = \omega R/S_L \cos \alpha$ is a dimensionless reduced angular frequency.

Perturbations in the positions of the flame front and interface between burned gases and ambient air correspond also to harmonic signals inducing disturbances in the length $L_f = \tilde{L}_f \exp(-i\omega t)$ and in the travel time of ultrasonic waves crossing this flow $\Delta t' = \tilde{\Delta t} \exp(-i\omega t)$ which are linked by:

$$\frac{\tilde{L}_f}{\bar{L}_f} = \frac{\tilde{\Delta t}}{\bar{\Delta t} - \Delta t_0} = \frac{\tilde{r}_o - \tilde{r}_i}{\bar{r}_o - \bar{r}_i} \quad (4.8)$$

By placing the transmitter and the receiver at half the height of the flame $y = H/2 = R/(2 \tan \alpha)$, and by combining the expressions Eqs. (4.3) and (4.6) to (4.8), one obtains the link between heat release rate and sound travel time disturbances:

$$\mathcal{T}_r = \frac{\tilde{\dot{Q}}/\bar{\dot{Q}}}{\tilde{\Delta t}/(\bar{\Delta t} - \Delta t_0)} \quad (4.9)$$

where

$$\mathcal{T}_r = \frac{(4 - 3\Gamma)^{1/2} - 1}{\Gamma(4 - 3\Gamma)^{-1/2} - 1} \times \frac{i}{\omega_*} \frac{[1 - \exp(i\omega_* \cos^2 \alpha)] - [1 - \exp(i\omega_*)] \cos^2 \alpha}{\exp(1/2i\omega_*) - \exp(1/2i\omega_* \cos^2 \alpha)}$$

This link corresponds to a transfer function \mathcal{T}_r in the frequency space which depends on the dimensionless parameter Γ characterizing the flow operating conditions, the flame aspect ratio or flame angle α and the reduced angular frequency ω_* . The experimental methodology to determine the transfer function \mathcal{T}_r is described in the next section.

4.2 Experimental configuration

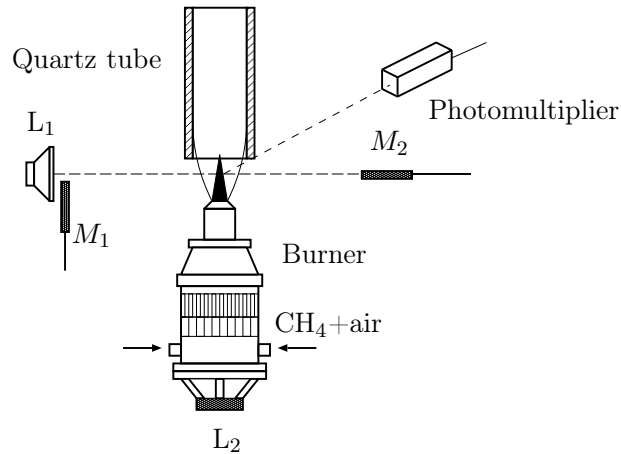


Figure 4.5 : *Experimental setup used to validate the acoustic methodology. The burner is equipped with a loudspeaker to modulate the flow. The chemiluminescence emission is recorded with a photomultiplier. A quartz tube is placed on the top of the flame.*

Experiments are conducted with the setup described in Chapter 1. Laminar conical premixed methane/air flames are stabilized on the lips of the burner and are submitted to velocity modulations with a loudspeaker L2 at the base of the burner. Ultrasonic pulses used to probe the reacting flow are generated by the tweeter L1 which is placed on one side of the setup. The high frequency acoustic waves produced are recorded by microphones M1 and M2 before and after their passage through the flame. Microphones M1 and M2 are placed in front of the flame at the elevation corresponding to half of the flame height. These microphones are well aligned so that sound waves cross the burner on the symmetry axis in Fig. 4.5. The steady and modulated flow velocities are also controlled with a hot-wire placed at the exit of the burner (in the absence of combustion). The photomultiplier PM records the light intensity from the chemiluminescence emission of the flame. A quartz tube, with an inner diameter of 50 mm and a length of 300 mm is placed on the top of the burner to partially confine the burned gases and avoid flame flickering (Kizirnis et al. 1984; Linteris and Rafferty 2008). Heat release rate fluctuations measured with the photomultiplier PM can be compared to those deduced from fluctuations in the travel time of ultrasonic waves determined with microphones M1 and M2.

4.3 Experimental validation

Four conical methane/air flames designated by FL1 to FL4 featuring a distinct equivalence ratio ϕ or flow velocity \bar{v}_u are used in this study to validate the acoustic methodology. The operating conditions are gathered in Tab. 4.1.

Table 4.1 : *Flame characteristics. ϕ : equivalence ratio; S_L : laminar burning velocity; \bar{v}_u : flow velocity; H : flame height; Γ : dimensionless flame parameter; c^* : equivalent speed of sound.*

	ϕ [-]	S_L [m·s ⁻¹]	\bar{v}_u [m·s ⁻¹]	H [mm]	Γ [-]	c^* [m·s ⁻¹]
FL1	0.90	0.34	1.5	42	-4.4	548
FL2	1.00	0.38	1.5	38	-4.3	539
FL3	1.00	0.38	1.1	27	-5.0	539
FL4	1.00	0.38	1.9	49	-3.2	539

The acoustic method is first validated with FL1 in the absence of modulation. Figure 4.3 indicates that the acoustic path width L_f traversed by the ultrasonic waves in the burned gases varies with the distance y from the nozzle outlet. This width $L_f = 2(r_o - r_i)$ can be determined from Schlieren images by identifying the locations of the flame front r_i and the interface between the burned gases and ambient air r_o . Theoretical estimates with Eq. (4.3) can also be used. By modifying the positions of the microphones M1 and M2 above the burner it is also possible to determine the evolution of the travel time of ultrasonic waves as a function of the distance y . In these experiments, the vertical position of the microphones is increased by steps of 5 mm to record the different sets of data. The evolution of the mean sound travel time difference $\Delta t_0 - \overline{\Delta t}$ with the distance y is presented in Fig. 4.6 with square markers. Results are compared with the travel time $\overline{L_f}/c^*$ deduced from Eq. (4.3) (black line) and from the Schlieren images (gray line). A good match is found between the different methods for axial distances lower than $y \leq 20$ mm. These experiences are repeated for the three operating conditions FL2 to FL4. They yield the same type of results. The pulse compression technique developed in this study can thus be used to estimate the mean width of burned gases traversed by ultrasonic waves when optical access is limited.

Results are now examined for flames submitted to harmonic flow modulations. The characteristics of the chirp signals indicated in Tab. 2.2 enable to obtain time resolved data at a repetition rate of 1 kHz which is limited here by the

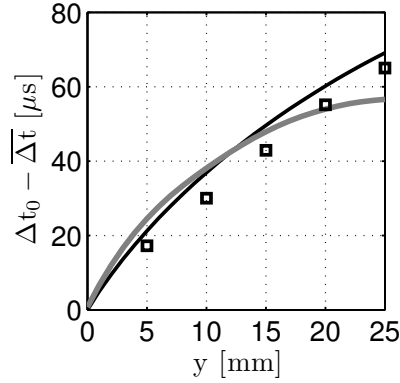


Figure 4.6 : Validation of the acoustic methodology to determine the mean travel time $\Delta t_0 - \overline{\Delta t}$ induced by the presence of burned gases with the acoustic method (markers \square). Comparisons with estimates $\overline{L_f}/c^*$ deduced from Eq. (4.3) (black line) and from the analysis of the Schlieren images (gray line). Flame FL1.

chirp repetition time $t_r = 1$ ms. This repetition rate is mainly limited by the material available (the actuators and sensors) used to generate and record the sequences of ultrasounds modulated signals. This repetition rate is large enough to determine heat release rate fluctuations at the largest modulation frequency envisaged in this study $f = 100$ Hz. The incident and transmitted signals measured by microphones M1 and M2 are sampled at a frequency 2^{21} Hz during one second. The resulting signal Δt obtained from the pre-processing procedure detailed in Section 2.4.1 is filtered by a low-pass zero-phase shift filter with a cut-off frequency equal to 200 Hz. It is then possible to examine effects of the flame on the sound travel time of ultrasonic waves when the flow is modulated. In the following experiments, the velocity modulation level is controlled by the hot wire placed at the burner outlet in a separate set of experiments in the absence of combustion but under the same flow conditions. Perturbations in the sound travel time determined with this method are plotted in Fig. 4.7 for two forcing frequencies $f = 40$ and 80 Hz and a modulation level $v_{urms}/\bar{v}_u = 0.09$. In the absence of flame, results collapse for both frequencies on a constant straight line $\Delta t_0 = 893 \mu s$ indicating no measurable fluctuations in the propagation time of ultrasonic waves transmitted through the modulated flow. Transmitted ultrasonic waves then barely interact with this modulated inert flow but are characteristics of the flame response. When flame FL1 is placed between the sound transmitter and receiver, the sound travel Δt drops due to the increase in the speed of sound in the burned gases. Figure 4.7 also clearly shows that this response features a periodic behavior that depends on the forcing frequency. These experiments with and without flame can be used

to obtain the difference $\Delta t_0 - \overline{\Delta t}$ induced by the presence of the flame which is equal in this case to $57 \mu\text{s}$ and does not depend on the forcing frequency.

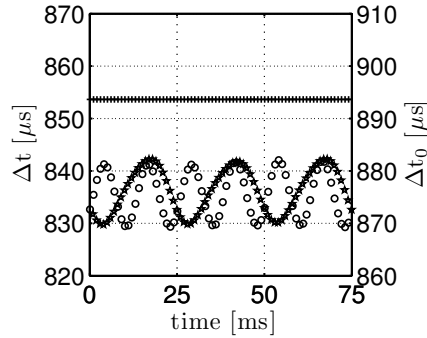


Figure 4.7 : Time history of sound travel time in the presence of flow modulation $v_{urms}/\bar{v}_u = 0.09$. Results are presented for two forcing frequencies $f=40$ Hz (\star) and $f=80$ Hz (\circ). Measurements with flame FL1 are linked to the left axis. Measurements without flame are linked to the right axis. In the absence of the flame, data collapse on a single value $\Delta t_0 = 893 \mu\text{s}$ for the two forcing frequencies ($+$).

The photomultiplier signal is also recorded and sampled at a frequency of 8192 Hz during a period of one second. It is then filtered with the same low pass filter as the acoustic signal. The output of the signal synthesizer is used as a reference to synchronize all the diagnostics. Data for the velocity signal v_u measured by the hot wire, flame chemiluminescence intensity I collected by the PM and sound travel time Δt deduced from the two microphones are shown in Fig. 4.8 for two modulation frequencies $f = 40$ and 80 Hz and a fixed perturbation level $v_{urms}/\bar{v}_u = 0.09$. The chemiluminescence intensity I and the sound travel time Δt correspond nearly to harmonic signals featuring the same frequency as the velocity disturbance v_u imposed at the burner outlet. These signals clearly follow the flow modulation at the two forcing frequencies. They feature however different phase lags between them which are also a function of the forcing frequency.

Increasing the modulation amplitude, the shape of the velocity, chemiluminescence and sound travel time signals feature larger differences with a pure harmonic response. A spectral analysis not represented here shows that the main peak is always clearly associated with the modulation frequency for all cases investigated. The evolution of the amplitude of the light intensity signal I which is proportional to the fluctuation in heat release rate and the evolution of the oscillation amplitude of the sound travel time Δt are examined in Fig. 4.9 when the perturbation level v_{urms}/\bar{v}_u is progressively increased. For

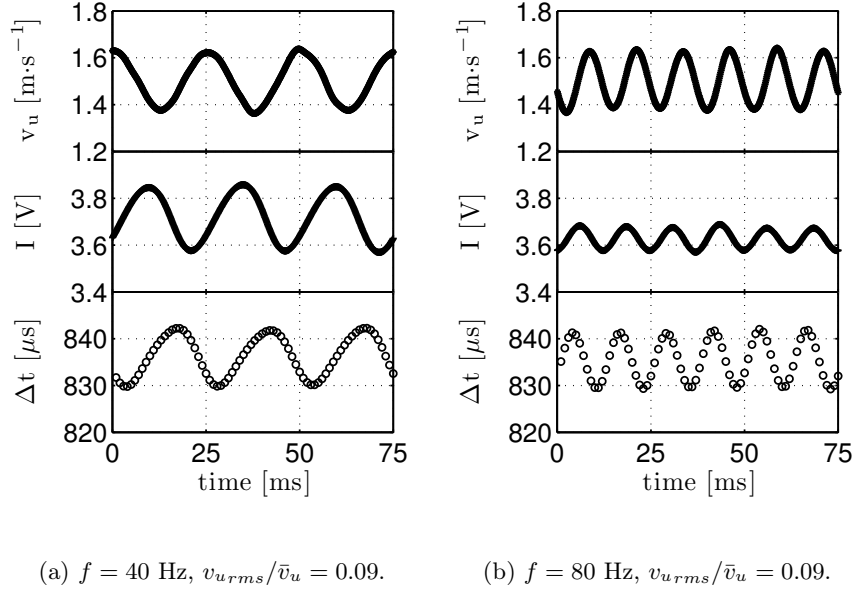


Figure 4.8 : Synchronized measurements of the flow velocity at burner outlet v_u (top), light intensity I (middle) and sound travel time Δt (bottom) of flame FL1 for two flow modulation frequencies.

small disturbances, fluctuations in the chemiluminescence intensity and sound travel time increase linearly with the forcing level at both frequencies investigated $f = 40$ and 80 Hz. Saturation is however reached in the sound travel time measurements at a lower forcing level than in the chemiluminescence signals which remain roughly linear over the range of perturbation levels explored. This figure also indicates that the saturation level slightly depends on forcing frequency. Significant deviation from linearity in the sound travel time response occurs for $v_{urms}/\bar{v}_u \simeq 0.2$ at $f = 40$ Hz and $v_{urms}/\bar{v}_u \simeq 0.1$ at $f = 80$ Hz in this figure. A direct interpretation of these fluctuating signals remains however difficult since they do not account for changes in the mean signal when the modulation amplitude is increased. It is more appropriate to compare the relative ratio I_{rms}/\bar{I} and $\Delta t_{rms}/(\Delta t_0 - \bar{\Delta t})$ as illustrated in Fig. 4.10. The linear link between these two ratios is demonstrated here when the perturbation level is not too large but the figure also shows that the proportionality coefficient depends on frequency. It is also worth noting that small fluctuations in the relative chemiluminescence intensity signal result here in relatively large disturbances of the sound travel time emphasizing the sensitivity of the acoustic technique. Data in this figure are also compared to predictions from Eq. (4.9) obtained for vanishingly small flow perturbations. These theoretical estimates

fit well with the measurements at the forcing frequency $f = 40$ Hz as long as relative fluctuations in the sound travel time are not too large. A linear relationship is also found at 80 Hz but with a large difference between theoretical predictions and experimental results. This is probably due to the fact that the shape of the flame front and burned gases interface are less well reproduced by the model (see Fig. 4.4(c) and (d)). Perturbations in the sound travel time can safely be used to reconstruct the amplitude of heat release rate disturbances \dot{Q}_{rms}/\bar{Q} for fluctuation levels limited to about $\Delta t_{rms}/(\Delta t_0 - \bar{\Delta t}) \leq 0.15$ in the conditions explored in this study. This constitutes the first validation of the proposed acoustic methodology to determine the amplitude of heat release rate disturbances for small to moderate velocity perturbations. It is now interesting to examine the phase difference between the chemiluminescence emission I and sound travel time response Δt by computing the cross-correlation between these two signals. This phase shift does not change with the perturbation amplitude v_{urms}/\bar{v}_u in the linear regime, but depends on the forcing frequency as indicated by the bottom plots in Fig. 4.9.

These data are completed by systematic measurements of flame chemiluminescence and sound travel time for forcing frequencies ranging from 20 to 100 Hz at a fixed modulation level $v_{urms}/\bar{v}_u = 0.09$. These signals are treated to determine the transfer function $\mathcal{T}_r = \left[(I - \bar{I})/\bar{I} \right] / \left[(\Delta t - \bar{\Delta t})/(\Delta t_0 - \bar{\Delta t}) \right]$. Results for flames FL1 to FL4 featuring different flow operating conditions are compared to theoretical estimates from Eq. (4.9) in Figs. 4.11(a) to 4.11(d). The gain $G = |\mathcal{T}_r|$ is plotted in the top of the figures while the phase lag $\varphi = \arg(\mathcal{T}_r)$ between heat release rate disturbances and fluctuations in the sound propagation time is represented in the bottom plots. A good agreement between predictions and measurements is obtained for the gain and phase of the transfer functions except at low frequencies where buoyancy effects strongly disturb the acoustic signals.

Deviations from theoretical estimates are attributed to fluctuations in the volume of the hot gases plume due to the intrinsic instability of the interface between the burned gases and ambient air studied in chapter 3. This instability is attenuated in this study by partially confining the flame plume with a quartz tube, but it is not possible to eliminate it completely. The motion of the burned gases and ambient air interface induced by flame wrinkling is modeled before this interface destabilizes due to buoyancy forces. Predictions of the transfer function in the frequency range of buoyancy characteristics frequencies inevitably deteriorate. Note that this aspect of the problem is specific to unconfined flames in contact with ambient air. Buoyancy effects are absent in confined configurations and the situation is simpler provided that the ultrasonic actuators and sensors can withstand high temperatures.

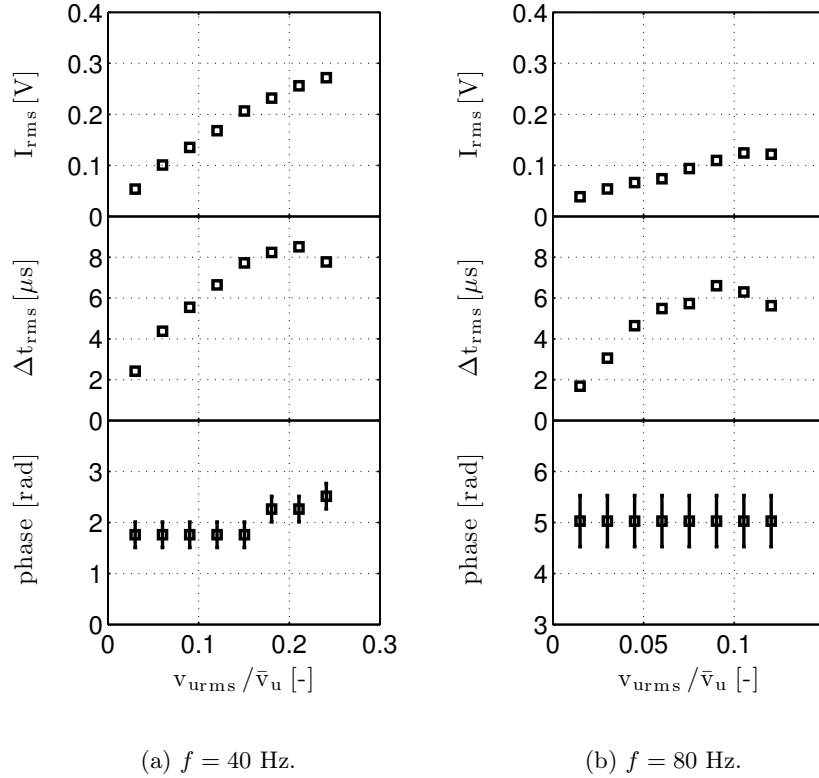


Figure 4.9 : Plots of r.m.s value of I and Δt , and the phase shift between the two signals as a function of the flow modulation level v_{urms}/\bar{v}_u for two modulation frequencies. Flame FL1.

4.4 Conclusion

It has been shown that it is possible to estimate heat release rate perturbations by measuring fluctuations in the sound propagation time of ultrasonic waves transmitted through a flame. An analytical expression between heat release rate and sound travel time disturbances has been derived in the case of pulsed conical laminar premixed flames. This corresponds to a transfer function that depends on the flow operating conditions, flame shape and modulation frequency. This has also led to the development of an acoustic methodology to determine small changes in the sound propagation time of ultrasonic waves crossing an unsteady reacting flow using a pulse compression technique. First validations were conducted in a generic configuration with a tweeter to generate the sound waves and microphones to record the incident and transmitted signals when the flow is submitted to harmonic velocity modulations. The

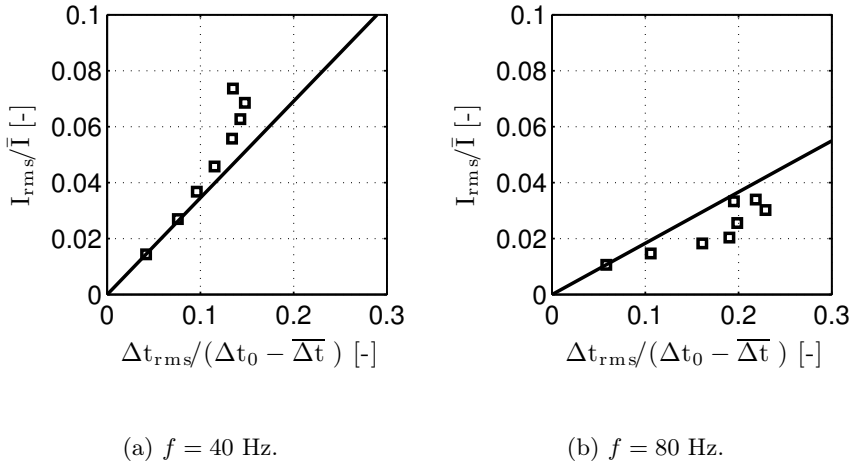
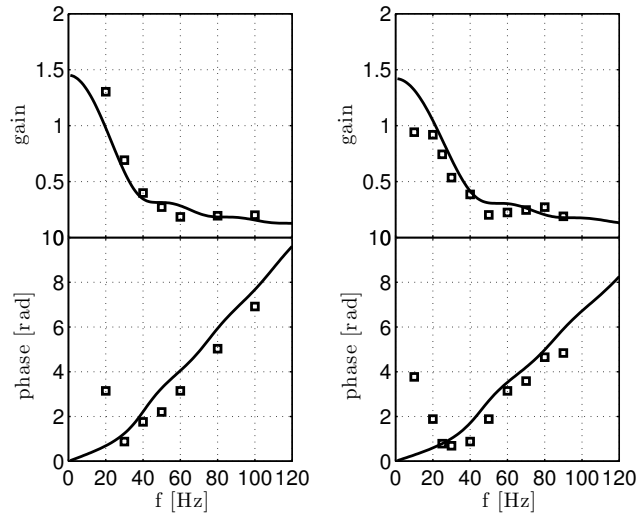


Figure 4.10 : Heat release rate fluctuation I_{rms}/\bar{I} as function of sound propagation time disturbances $\Delta t_{rms}/(\Delta t_0 - \bar{\Delta t})$ for two modulation frequencies. Markers \square indicate the measurements and solid line denotes the theoretical predictions from Eq. (4.9). Flame FL1.

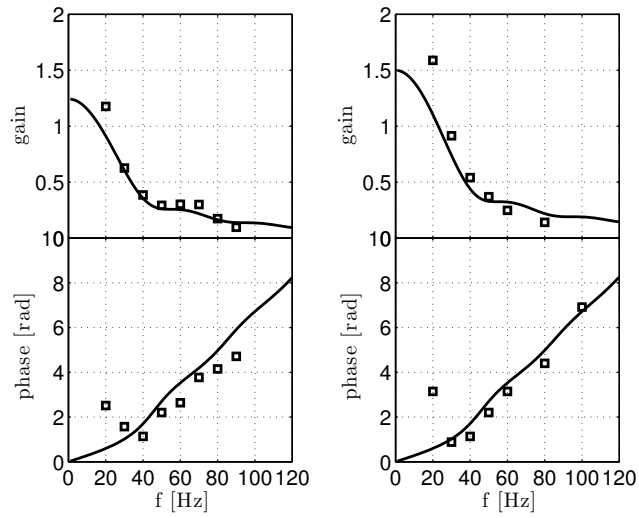
linearity of the response of sound travel time fluctuations induced by heat release rate disturbances has been demonstrated experimentally when the flame is submitted to flow modulations at different forcing frequencies and when the perturbation level is not too large. A saturation phenomenon was highlighted at higher modulation amplitudes. Predictions of the transfer function between heat release rate and sound travel time disturbances show good agreement with experimental data for lean and stoichiometric laminar flames obtained at different flow and mixture.

In the absence of external forcing device, it was also shown in the preceding chapter that the proposed technique is very sensitive to small heat release rate disturbances produced by an intrinsic hydrodynamic flow instability. This was used to detect low frequency tiny heat release rate perturbations. These combined measurements demonstrate the sensitivity of the proposed technique to internal and external flow perturbations. In both cases, it was shown how to obtain time resolved data with a relatively inexpensive material. These results are encouraging and motivate further developments of this alternative technique when optical access is limited. Remaining issues for the validation of this technique in more sophisticated configurations are examined in the conclusion of this manuscript.



(a) Flame FL1.

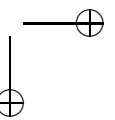
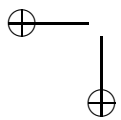
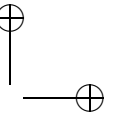
(b) Flame FL2.



(c) Flame FL3.

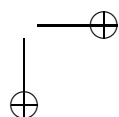
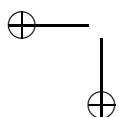
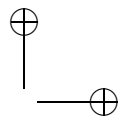
(d) Flame FL4.

Figure 4.11 : Comparison between analytical predictions and experimental results for the transfer function \mathcal{T}_r as a function of modulation frequency f .



Part II

Optical diagnostic



Chapter 5

Probing reacting flows with a Laser Interferometric Vibrometer

A Laser Interferometric Vibrometer (LIV) is used to probe reacting flows in this chapter. The principle of LIV is firstly described. The technique is then used to detect the sound waves produced at the burner outlet when the flow is modulated. The results are compared to the sound pressure measured by a microphone at the same position. The final section is devoted to measurements with combustion. Density fluctuations in a hot jet are firstly probed with the LIV. The hot jet is produced by a laminar conical premixed flames confined by a quartz tube. Measurements are conducted at the outlet of the quartz tube. The resulting integrated density fluctuations and local density perturbations deduced from an Abel inversion at different measurement positions are mapped to identify the density distribution in the hot jet. Finally, the LIV is used to probe laminar pulsated flames. Experiments are conducted to examine the possibility to use this technique to determine density fluctuations in flames and to optimize the LIV settings for the measurements in the next two chapters.

5.1 Laser Interferometric Vibrometry

5.1.1 Principle

Laser interferometric vibrometry (LIV) is a common technique based on a Mach-Zehnder interferometer to detect surface vibration (Kokkonen and Kaivola 2008; Schott 2010). The principle is described in Fig. 5.1. A continuous laser beam is generated and separated into two beams by a beam splitter. The first beam, which is considered as the reference beam, is reflected by a reference re-

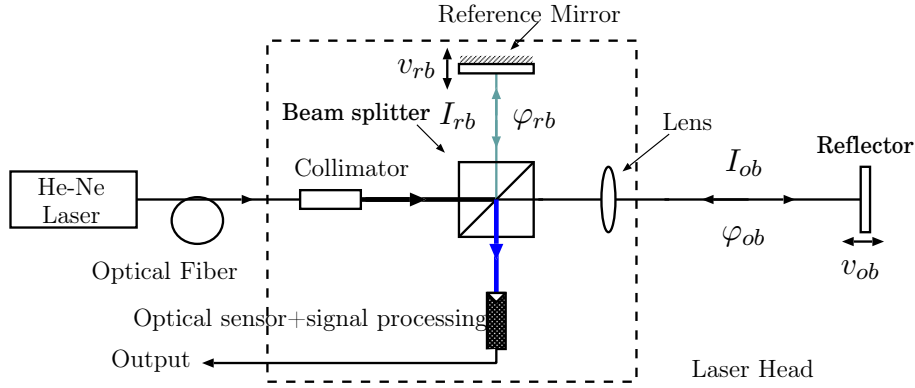


Figure 5.1 : Schematic view of the principle of Laser Interferometric Vibrometer.

reflector, passes again through the beam splitter and is transmitted to an optical sensor. The second beam, named the object beam, crosses a lens, traverses the flow that is probed, is reflected by an external reflector, traverses again the probed flow, the LIV lens and beam splitter and is finally recorded by the same optical detector as the reference beam. The reference beam is characterized by a light intensity I_{rb} and phase φ_{rb} at the optical detector location. The object beam features an intensity I_{ob} and phase φ_{ob} at the same location. The phase difference $\varphi = \varphi_{ob} - \varphi_{rb}$ results from the integrated value along the optical path. It can be expressed as:

$$\varphi(x, y, t) = \frac{2\pi}{\lambda_0} \int_{\text{object}} n(x, y, z, t) dz - \frac{2\pi}{\lambda_0} \int_{\text{reference}} n(x, y, z, t) dz \quad (5.1)$$

where the coordinate z indicates the direction of the object beam normal to the x - y plane. In this expression, λ_0 denotes the wavelength of the laser beam in the vacuum and n represents the refractive index. Keeping the refractive index constant, Eq. (5.1) can be simplified to:

$$\varphi(t) = \frac{4\pi}{\lambda} z(t) \quad (5.2)$$

where $\lambda = \lambda_0/n$ is the laser beam wavelength in the medium of refractive index n and $z(t)$ denotes the distance between the laser head and the external reflector. The displacement of the reflector alters the phase difference:

$$\Delta\varphi(t) = \frac{4\pi}{\lambda} \Delta z(t) \quad (5.3)$$

This link is widely used in analysis of vibration of surfaces (Graebner et al. 2000).

CHAP. 5 - PROBING REACTING FLOWS WITH A LASER INTERFEROMETRIC VIBROMETER 91

The phase difference can be obtained by counting the fringes of the interferogram. The light intensity distribution of the reference beam and the object beam combined at the detector location writes:

$$I_{com} = I_{rb} + I_{ob} + 2(I_{rb}I_{ob})^{1/2} \cos(\varphi_{ob} - \varphi_{rb}) \quad (5.4)$$

When the phase difference $\varphi = \varphi_{ob} - \varphi_{rb} = 2N\pi$, where $N = 0, \pm 1, \pm 2, \dots$, the light intensity at the detector location reaches maximum values corresponding to distinct bright fringes in the interferogram. The values $\varphi = (2N + 1)\pi$ correspond to dark fringes. A photodetector focusing on the interferogram is used to scan the light fringes and determine the phase difference.

Equation (5.1) indicates that the phase difference is a function of the geometrical path z and refractive index n . By keeping the refractive index constant, this technique can be used to measure distances. The situation in this work is different and the distance z is kept constant. Modifications of the refractive index n constitute disturbances of the phase difference $\varphi'(t)$. The refractive index of a gas depends on its density and this link can be described by the Gladstone-Dale relation (Menkirch 1981):

$$n - 1 = G\rho \quad (5.5)$$

where G denotes the Gladstone-Dale coefficient for a mixture of gases and ρ represents the mixture density. The Gladstone-Dale coefficient of the mixture is given by:

$$G = \sum_i \frac{\rho_i}{\rho} G_i \quad (5.6)$$

where G_i is the Gladstone-Dale constant of each component (i) and ρ_i its corresponding partial density. The configurations investigated in this work are more complicated since the gas mixture composition changes during the combustion of methane-air reactants to combustion product. In analysis with diffusion flames, Gardiner et al. (1981) suggested the use of an average molar refractive index which takes into account different chemical products after combustion. For the premixed flames envisaged in this work, the situation can be further simplified. A constant Gladstone-Dale coefficient can be used to analyze premixed flames. Reuss (1983) found that the variation of this coefficient during combustion does not exceed $\pm 2\%$. In this work, a constant value $G = 2.5 \cdot 10^{-4} \text{ m}^3 \cdot \text{kg}^{-1}$ (Giuliani et al. 2010b) is used for the calculation. Density disturbances in the flow thus manifest in changes of refractive index (Mayrhofer and Woisetschlager 2001; Koberl et al. 2010) leading to perturbations of the phase difference φ . Perturbations in density correspond to phase differences given by:

$$\varphi'(t) = \frac{4\pi G}{\lambda_0} \int_L \rho'(z, t) dz = \frac{4\pi G}{\lambda_0} \langle \rho'(t) \rangle L \quad (5.7)$$

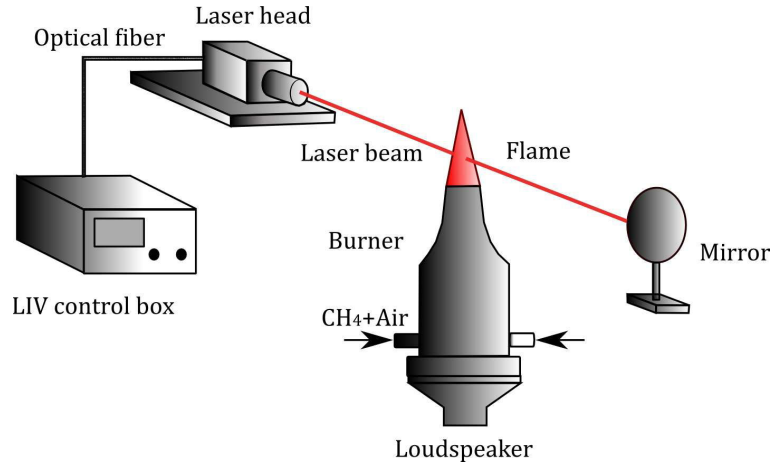


Figure 5.2 : *Experimental setup with a LIV used to probe laminar premixed flames.*

where, L indicates the geometrical path and is kept constant. In this expression, $\langle \rho'(t) \rangle_L$ corresponds to the resulting density fluctuation along the geometrical path L and is the main quantity measured in this work.

The LIV technique described herein is sensitive to the phase changes induced by density fluctuations in the investigated flow and light deflection effects used for example in the Schlieren imaging technique are not considered (Mayrhofer and Woisetschlager 2001).

5.1.2 Description of the LIV

In these experiments, a LIV model LS-V 2500 from SIOS Metechnik GmbH is used to determine line-of-sight integrated density fluctuations in laminar premixed flames (Fig. 5.2). It comprises a He-Ne laser ($\lambda_0 = 633$ nm) with an object beam traversing a sensor head constituted by a compact objective used both as a transmitter and receiver. The laser passes through the reacting flow (for example the flame shown in Fig. 5.2) and is then reflected by a flat aluminum mirror located at a fixed position, passes through the reacting flow again and is recorded by the sensor head. The distance between the sensor head and burner axis is fixed to $L_{bl} = 500$ mm and $L_{bm} = 200$ mm between the mirror and burner axis. The laser is focused on the mirror and the size of the laser beam in the flame zone does not exceed a diameter of 2 mm in these experiments.

The voltage output U from the LIV signal processor yields an information which

is proportional to density fluctuations integrated along the laser beam:

$$U = k_{gain} G \langle \rho'(t) \rangle L \quad (5.8)$$

where k_{gain} is the unit conversion factor ranging from $1000.97 \text{ V}\cdot\text{m}^{-1}$ to $4.17 \text{ V}\cdot\mu\text{m}^{-1}$. The gain can be adjusted from the LIV control box presented in the Fig. 5.2. The frequency bandwidth of the LIV ranging from 0 to 500 kHz enables to detect disturbances in density at very high frequencies. The system is limited by its maximum translation rate $1.5 \text{ m}\cdot\text{s}^{-1}$ yielding the corresponding value $[d\langle \rho'(t) \rangle L/dt]_{max} = 6000 \text{ kg}\cdot\text{m}^{-2}\cdot\text{s}^{-1}$ for the rate of change of line-of-sight integrated density fluctuations. This value is large compared to density fluctuations expected in the perturbed flames investigated.

The upper and lower bounds on the output signal are set to $\pm 3 \text{ V}$ by the manufacturer. The voltage output is converted to a digital signal by a A/D converter equipped in the computer which has a maximum tolerance of $\pm 10 \text{ V}$ and voltage precision of $5\cdot 10^{-3} \text{ V}$.

5.1.3 Alignment of the instrumentation

The laser head and the external mirror must be accurately aligned to maximize reflection and obtain the full benefit of the high metric accuracy of the LIV. The laser beam in these experiments passes through the axis of the burner. The LIV is ready for operation once the beam exiting the sensor head has been aligned normal to the external mirror reflecting surface. The alignment can be performed either by aligning the laser head on the external mirror and/or adjusting the orientation of the external mirror. When the alignment is well performed, the amplitude of the signals on the light detection system of the reference beam and the object beam (Eq. (5.4)) reaches a maximum value and the full performance of the instrument is obtained. This signal can also be used to monitor alignment. During the alignment, a piezoelectric vibrator mounted on the reference mirror (Fig. 5.1) is turned on to generate controlled disturbances of its position. The motion of the mirror changes the phase difference φ . The reference mirror displaces with a velocity $v_{rb} = \hat{v}_{rb} \cos(\omega_{rb}t)$ and adds a Doppler frequency $f_{dp} = 2v_{rb}/\lambda_0$ to the reference beam. The altered frequency f_{rb} of the reference beam can be expressed as:

$$f_{rb} = f_{lb} + \frac{2v_{rb}}{\lambda_0} \quad (5.9)$$

where f_{lb} indicates the frequency of the laser beam. This procedure induces perturbations in the phase difference $\varphi'(t)$:

$$\varphi'(t) = \frac{4\pi\hat{v}_{rb}}{\lambda_0} \cos(\omega_{rb}t) \quad (5.10)$$

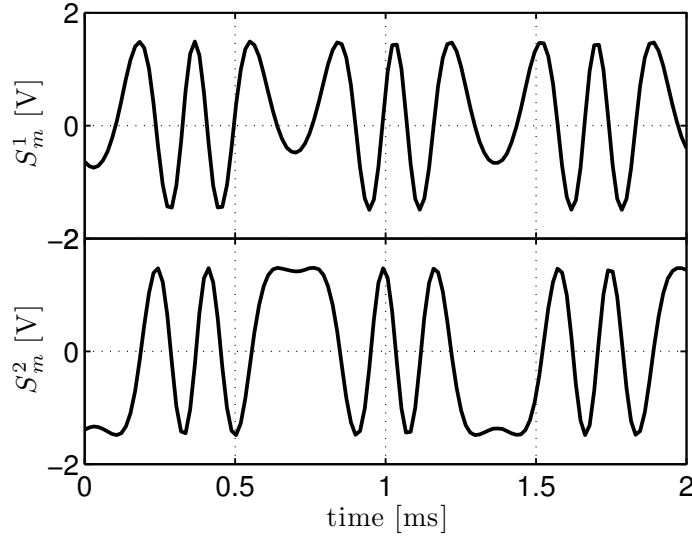


Figure 5.3 : Evolution of the electrical signals S_m^1 and S_m^2 when the alignment is optimized.

Disturbances in the phase difference correspond to fluctuations in the interferogram at the detector location:

$$I'_{com}(t) = 2 (I_{rb}I_{ob})^{1/2} \cos \left[\frac{4\pi\hat{v}_{rb}}{\lambda_0} \cos(\omega_{rb}t) \right] \quad (5.11)$$

A pair of photodiodes installed inside the sensor head transform incoming optical radiation into electrical signals. These electrical signals are then processed

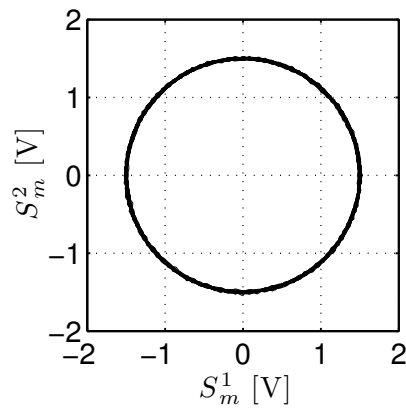


Figure 5.4 : The Lissajous figure between the two signals S_m^1 and S_m^2 presented in Fig. 5.3. The radius is $r_m = 1.5$ V in this case.

to two signals S_m^1 and S_m^2 with a 90 degree phase shift as shown in Fig. 5.3 for one example. The Lissajous figure between these two periodic signals is shown in Fig. 5.4, where the radius of the circle indicates the amplitude of the two signals. The Lissajous figure provides a reference for the alignment. When the Lissajous figure takes the form of a circle and the radius reaches 1.5 V, alignment is optimized. After alignment, the piezoelectric vibrator is turned off.

5.1.4 Experimental setup

Once the alignment is done, the positions of the laser head and the external mirror are kept fixed. The same burner equipped with a loudspeaker is used in the following experiments. The burner is fixed on a two axes micrometric displacement table shown in Fig. 5.5 to move the burner in the vertical and horizontal directions by increments of $1 \mu\text{m}$. The origin of the coordinate system is located at the center of the burner exit. The abscissas x and y are used to indicate the horizontal and vertical directions respectively. A quartz tube on the top can also be used to confine the flame.

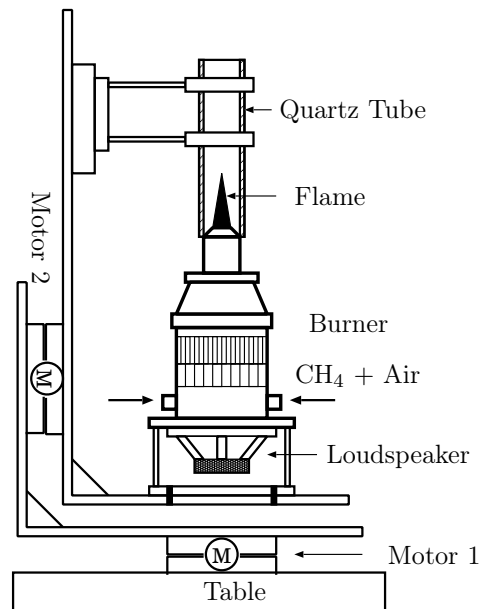


Figure 5.5 : Burner fixed on a two axes micrometric displacement table.

5.2 Analysis without combustion

5.2.1 Analysis in the absence of flow

Laser Interferometric Vibrometry has already been successfully used in the visualization of sound field in the vicinity of music instruments (Olsson and Tatar 2006; Gren et al. 2006). In this section, this technique is employed to detect the sound waves produced at the burner outlet with the loudspeaker fixed at the bottom of the burner. These experiments are conducted in the absence of mean flow. In this case, resulting density fluctuations originate only from the loudspeaker excitation. Measurements with LIV are made at a height $y = 10$ mm above the burner outlet. They are compared to separate measurements obtained with microphone M_1 at the same location.

For sound waves, pressure and density disturbances are linked by:

$$\rho' = \frac{p'}{c_0^2} \quad (5.12)$$

where c_0 is the speed of sound in ambient air. The acoustic pressure along the optical path of the laser beam is supposed uniform. The LIV yields a voltage output $U(t)$ which is proportional to line-of-sight integrated density fluctuations:

$$U(t) \propto \langle \rho'(t) \rangle L \propto p' \quad (5.13)$$

This voltage can be compared to the acoustic pressure $p'_M(t)$ measured at the burner outlet. The proportionality coefficient between these signals is denoted by Ξ_{pp} :

$$\langle \rho'(t) \rangle L = \Xi_{pp} p'_M(t) \quad (5.14)$$

The validation is conducted by progressively increasing the amplitude of the signal used to drive the loudspeaker. The signals from LIV and microphone M_1 are sampled with the same frequency $f_s = 8192$ Hz over 10 seconds. The density fluctuations produced by the acoustic forcing are very tiny at the burner outlet and the SNR in these experiments remains quite small. It is not worthy to analyze the signals in time domain. Power spectral analysis is used instead to examine the response of LIV and microphone M_1 . Figure 5.6 shows an example of results measured by the two diagnostics when the loudspeaker is turned off and on. The loudspeaker here is driven by a harmonic signal with a forcing frequency $f_m = 110$ Hz. A sharp peak located at the position $f = 110$ Hz emerges in the power spectral distribution for both signals when the loudspeaker is switched on indicating that the two diagnostics highlight the same behavior induced by the acoustic excitation. The main difference is that the LIV signal features also a low frequency background noise with a main peak around 25 Hz and few harmonics even in the absence of acoustic forcing.

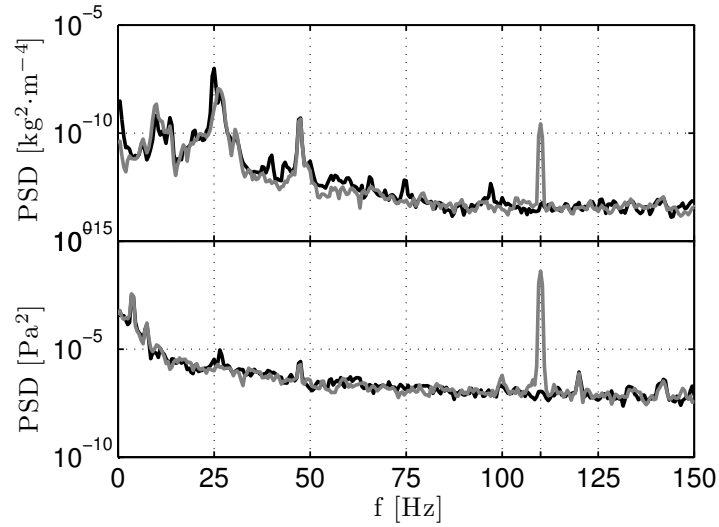


Figure 5.6 : Power spectral distribution of the signals from the LIV (upper figure) and microphone (bottom figure) when the loudspeaker is turned off (black line) and on (gray line). Harmonic forcing $f_m = 110$ Hz, $SPL = 80$ dB.

The SNR can be further improved by adding a Bragg Cell in the path of the object beam (see Giuliani et al. (2007)). The additional frequency shift induced by the Bragg Cell alters the phase difference and improves the SNR. The peaks at low frequency in the LIV measurements reduce significantly. In this work, the main objective is to measure density fluctuations in reacting unsteady

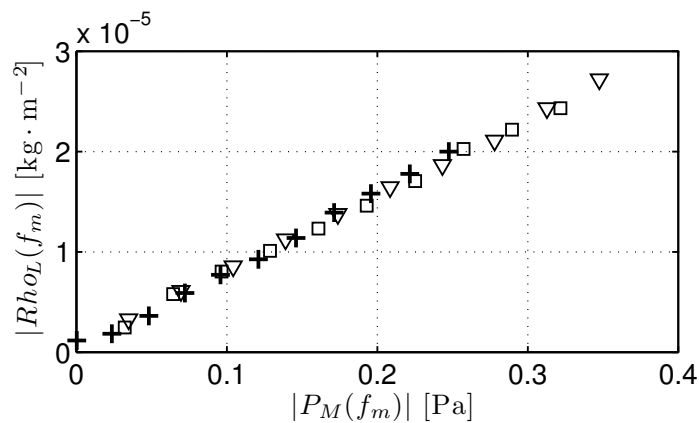


Figure 5.7 : Evolution of the LIV signal $|Rho'_L(f_m)|$ with the sound level $|P'_M(f_m)|$. Harmonic forcing at (+) $f_m = 110$ Hz, (∇) $f_m = 190$ Hz and (\square) $f_m = 270$ Hz.

flows. It will be shown later in the manuscript that in this case, density disturbances are much bigger and the SNR is much higher in reacting conditions. Such Bragg Cell was thus not used here.

The link between line-of-sight integrated density fluctuations $\langle \rho'(t) \rangle L$ measured by LIV and sound pressure $p'_M(t)$ measured by the microphone M_1 is examined in more details. This is conducted by taking the Fourier transforms of the two signals recorded $\langle \rho'(t) \rangle L$ and p'_M which write:

$$Rho'_L(f) = \int_{-\infty}^{\infty} \langle \rho'(t) \rangle L e^{-j2\pi ft} dt \quad (5.15)$$

$$P'_M(f) = \int_{-\infty}^{\infty} p'_M(t) e^{-j2\pi ft} dt \quad (5.16)$$

Figure 5.7 shows the evolution of $|Rho'_L(f_m)|$ with respect to $|P'_M(f_m)|$. The value $\Xi_{pp} = 8.1 \cdot 10^{-5} \text{ kg}\cdot\text{m}^{-2}\cdot\text{Pa}^{-1}$ can be obtained by linear regression of the data. This value does not depend on the forcing frequency indicating that the LIV technique can be used to measure density fluctuations induced by acoustic excitation.

5.2.2 Effect of an inert flow

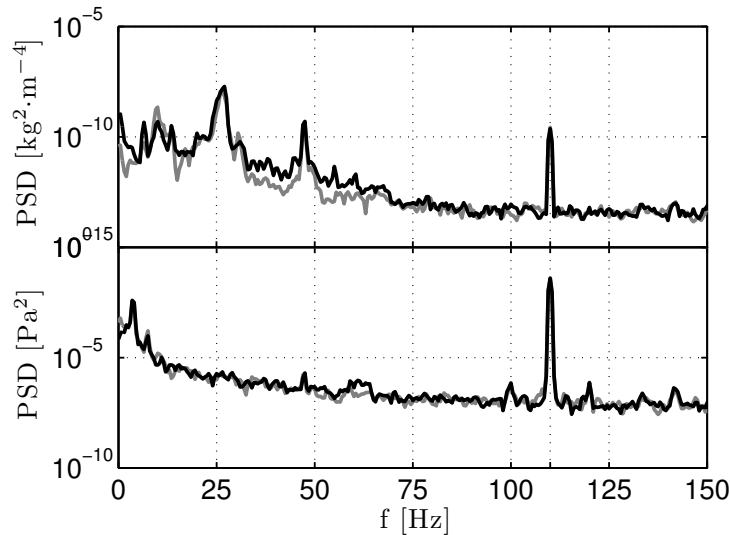


Figure 5.8 : Power spectral density of the signals from the LIV (top figure) and microphone M_1 (bottom figure) with (black line) and without (gray line) a mean laminar flow $\bar{v}_u = 1.5 \text{ m} \cdot \text{s}^{-1}$.

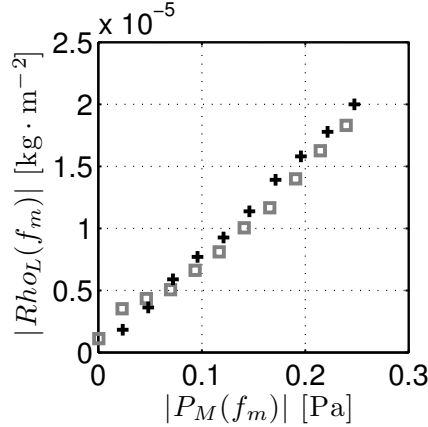


Figure 5.9 : Evolution of the LIV signal $|Rho'_L(f_m)|$ with the sound level $|P'_M(f_m)|$. With flow (\square) and without flow ($+$). Harmonic forcing at $f_m = 110$ Hz.

Effects of an additional low speed flow in these measurements is examined. An operating condition with a flow velocity $\bar{v}_u = 1.5 \text{ m}\cdot\text{s}^{-1}$ is investigated. The flow forms an jet at the burner outlet which is submitted to acoustic forcing by the loudspeaker at the bottom. Density fluctuations may originate from (a) acoustic excitation or (b) hydrodynamic disturbances. Figure 5.8 shows the power spectral distributions of the signals from LIV and microphone M_1 in the presence and absence of flow. The bottom figure shows that the acoustic response for the two cases are nearly the same, but the analysis of the top figure shows that the presence of the flow modulation adds small additional density perturbations. The comparison between the evolution of $|Rho'_L(f_m)|$ with $|P'_M(f_m)|$ with and without flow is shown in Fig. 5.9. Changes due to the flow modulation can be neglected compared to that from the acoustic excitations.

5.3 Analysis with combustion

5.3.1 Measurements in a hot jet

Density fluctuations in a hot jet are examined in this section. The hot jet is produced by a laminar conical flame confined in a quartz tube as shown in Fig. 5.5. The tube has a length of 150 mm and inner diameter of 27 mm. It is sealed at its bottom to avoid gas recirculation. When the flame is modulated, the heat release rate is altered due to the incoming flow perturbations induced by acoustic forcing. These perturbations produce in turn density disturbances in the burned gases.

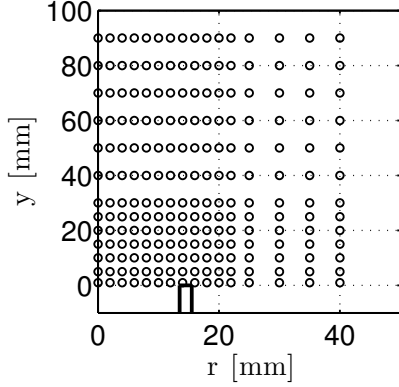


Figure 5.10 : Grid of measurement positions. The grid is dense in the zone next to the exit of the tube where large density fluctuations take places. The solid line indicates the tube wall. $y = 0$ indicates here the quartz tube outlet.

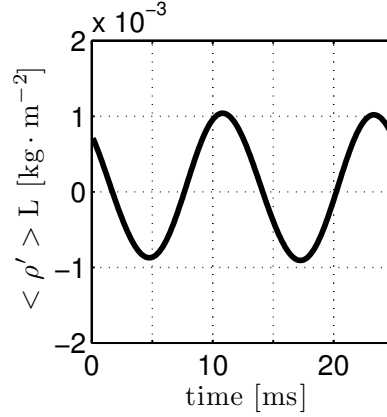


Figure 5.11 : Evolution of integrated density fluctuations $\langle \rho' \rangle L$ at the measurement position $[r, y] = [2, 20]$.

The burned gases form a hot jet at the quartz tube outlet featuring density disturbances. Measurements are conducted for the positions indicated in Fig 5.10, where $y = 0$ does not correspond to the burner outlet but indicates the quartz tube outlet. Since the flow is axisymmetric, measurements are made only on haft of the jet.

The flow velocity of the methane-air mixture is set to $\bar{v}_u = 1.5 \text{ m}\cdot\text{s}^{-1}$ and the equivalence ratio is equal to $\phi = 1.00$. The flow is modulated by harmonic forcing at $f_m = 80 \text{ Hz}$ with a perturbation level $v_{u,rms}/\bar{v}_u = 0.21$ measured at the burner outlet. The signal from LIV is sampled at a frequency $f_s = 10 \text{ kHz}$ during $t_s=10 \text{ s}$. The signal from the wave synthesizer used to drive the loudspeaker is also recorded to synchronize the LIV signals measured at different positions. Results are then post-processed using a Welch periodogram method (Rorabaugh 2011) to obtain a mean signal:

$$S_p(t) = \frac{1}{M} \sum_{i=1}^M S(t + N(i-1)T_m) \quad (5.17)$$

where $S(t)$ indicates the raw signal, $N = 8$ is the number of periods $T_m = 1/f_m$ per each sample of the raw signal and $M = 100$ is the number of sampling windows used to obtain the mean signal $S_p(t)$. The processed voltage signal U_p enables to determine the corresponding line-of-sight integrated density fluctuation $\langle \rho' \rangle L$ using Eq. (5.8). An example of result measured at the position

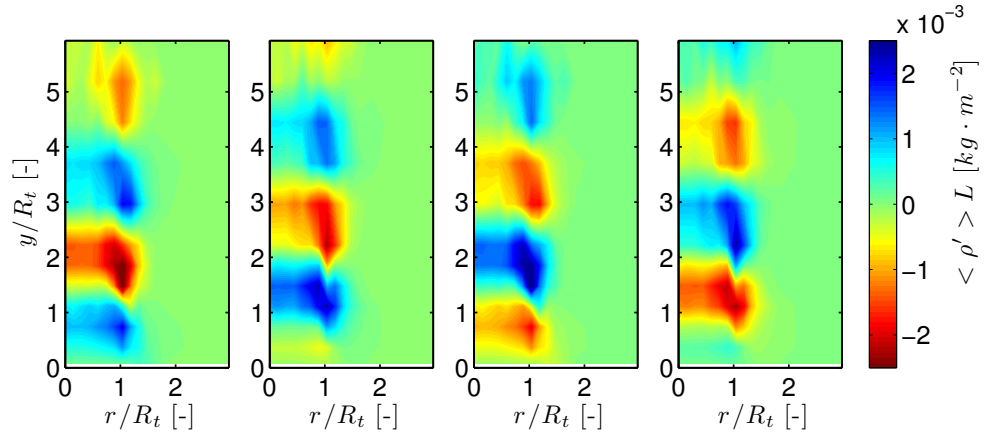


Figure 5.12 : Contour plot of line-of-sight integrated density fluctuations $\langle \rho' \rangle L$ in the modulated hot jet at four instants in the modulation cycle. From left to right: $t/T_m = 1/125, 32/125, 63/125, 94/125$, where $f_m = 1/T_m = 80$ Hz, and R_t denotes the inner radius of the quartz tube.

$[r,y]=[2,20]$ is shown in Fig. 5.11. Two modulation periods are shown in this figure clearly demonstrating that the density also oscillates at the modulation frequency.

It is interesting to map the integrated density fluctuations $\langle \rho' \rangle L$ at the dif-

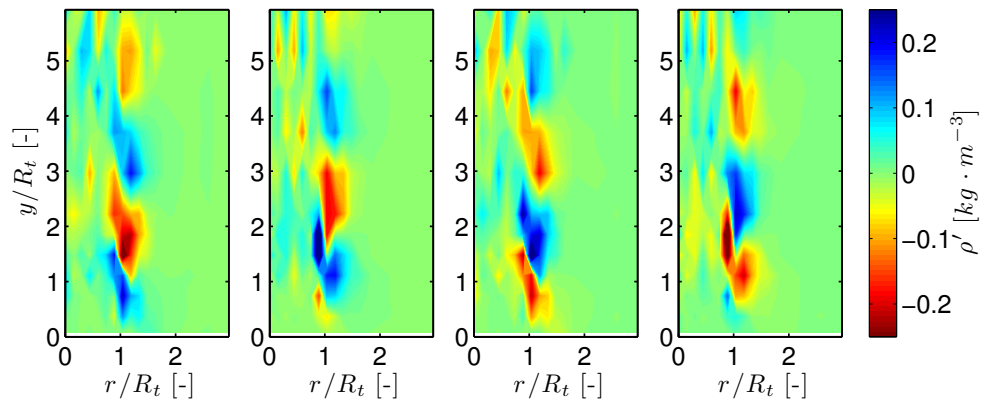


Figure 5.13 : Contour plot of the local density fluctuation ρ' at four instants corresponding to those shown in Fig. 5.12 for the same flow and modulation conditions.

ferent measurement grids during the modulation cycle. Four instants are shown in Fig. 5.12. The motion of the flow downstream the exit of the quartz tube is dominated by a convective wave at the modulation frequency $f_m = 80$ Hz. Regimes where the hot jet is mixed with ambient air feature the largest density fluctuations. This phenomenon can be highlighted by mapping the local density fluctuations at different measurement grids.

To obtain local density perturbations in the plane of symmetry of the burner, a tomographic reconstruction is used. The mean flow and coherent structures triggered by acoustic forcing of the hot jet envisaged features a rotationally symmetric shape, so the Abel inversion can be used (Walsh et al. 2000):

$$D(r) = -\frac{1}{\pi} \int_r^{r_\infty} \frac{dI(x)}{dx} \frac{1}{(x^2 - r^2)^{1/2}} dx \quad (5.18)$$

This inversion provides a radial symmetric distribution $D(r)$ from a set of integrated data $I(x)$ along the beam direction, recorded by traversing a line (x direction) normal to the beam direction. The projection data $I(x)$ are given by a set of discrete measurement data, for example the integrated density fluctuations $[\langle \rho' \rangle L](x, y, t)$ at the instant t . The discrete Abel inversion for this test writes:

$$\rho'(r(n), y, t) = -\frac{1}{\pi} \sum_{i=n}^{N-1} \frac{[\langle \rho' \rangle L](x(i+1), y, t) - [\langle \rho' \rangle L](x(i-1), y, t)}{(r^2(i) - r^2(n))^{1/2}} \quad (5.19)$$

where N indicates the number of measurement positions in the x direction. The resulting local density fluctuations ρ' are also mapped in Fig. 5.13 corresponding to those shown in Fig. 5.12. It is shown that there are large density fluctuations around the interface between the hot jet and ambient air.

5.3.2 Measurements in a pulsated flame

The technique LIV is now applied to detect line-of-sight integrated density fluctuations $\langle \rho'(t) \rangle L$ inside a pulsated flame. This information is used to estimate fluctuations of the position of the flame front and local heat release rate disturbances presented in the next two chapters. In this section, tests are carried out to examine the possibility to use this technique to determine density fluctuations in flames and to optimize the LIV settings for these measurements.

The first test is conducted on a laminar premixed conical flame in the absence of confinement tube. The flow velocity $\bar{v}_u = 1.5 \text{ m}\cdot\text{s}^{-1}$ and equivalence ratio $\phi = 1.0$ are fixed. The abscissa y now indicates the distance to the burner

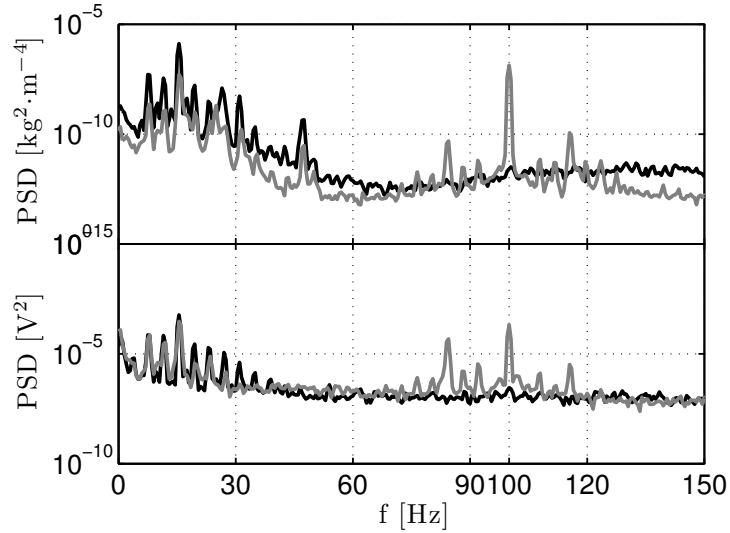


Figure 5.14 : *PSD of the signals from the LIV (top) and photomultiplier PM (bottom) for an unconfined flame with (gray line) and without (black line) harmonic flow modulation at $f_m = 100$ Hz.*

outlet. A photomultiplier PM located on the side of the burner records the chemiluminescence emission from the flame. Measurements are first examined without and with harmonic forcing at $f_m = 100$ Hz. In this case, the velocity fluctuation level at the burner outlet is fixed to $v_{u,rms}/\bar{v}_u = 0.07$.

Fig. 5.14 shows the power spectral density distribution of the signals from the LIV and photomultiplier. The PM and LIV output spectra features the same frequency content except at low frequency. The peaks around 15 Hz and the harmonics at 30 and 45 Hz correspond to the perturbations induced by the buoyancy forces already examined in Chapter 3 while the peak at 100 Hz corresponds to the harmonic flow modulation.

Buoyancy effects also affect the spectrum around the main peak at 100 Hz in the LIV signal. These components cannot be filtered unless buoyancy effects on the flame is eliminated. This can be done by placing a quartz tube on the top of the flame which was already used in Chapter 4. Measurements with LIV are then conducted for partially confined flames.

The tube is placed on the top of the burner at 30 mm from the burner exit. The tube is well aligned so that its axis coincides with the centerline of the burner. The measurements are done at the positions indicated in Fig. 5.15. Using elements from chapter 4, it is possible to predict the position of the flame front and

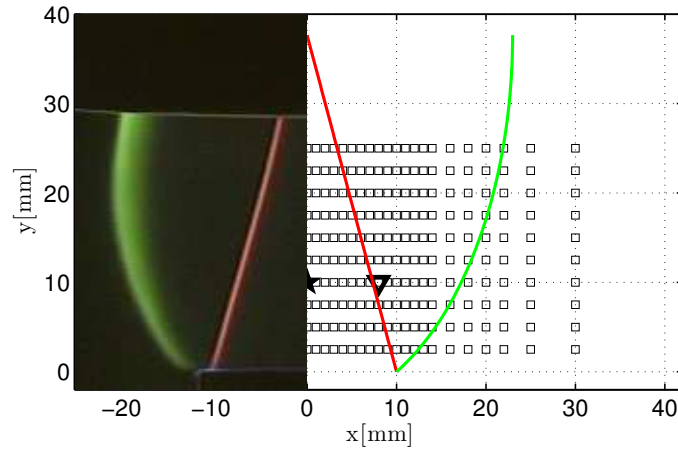


Figure 5.15 : Schlieren image of half of a partially confined conical steady flame (left part) and the corresponding grid of measurement positions for LIV (right part). The red line on the right indicates the flame front while the green one represents the boundary between burned gases and ambient air. The measurement grid is dense in the flame zone. Markers ★ and ▽ are used to represent the position $[x, y] = [0, 10]$ and $[8, 10]$. Operating conditions: $\phi = 1.00$, $\bar{v}_u = 1.50 \text{ m} \cdot \text{s}^{-1}$.

the boundary between the burned gases and ambient air using Eq. (4.3). Half of the figure represents a color Schlieren image of the partially confined flame. The right part of the figure indicates the predicted flame front (red line) and boundary of burned gases (green line) together with the different measurement

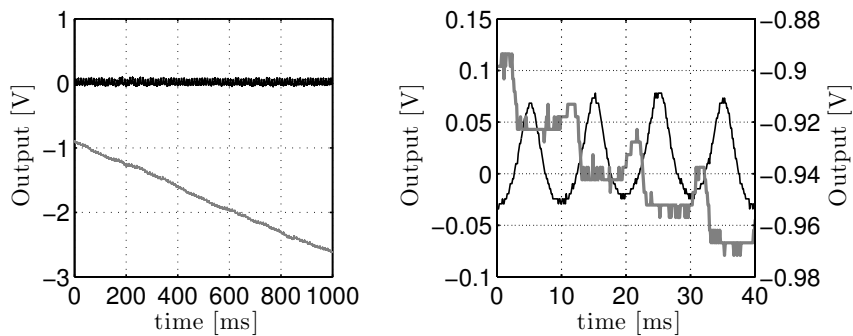


Figure 5.16 : Left figure: time evolution of the LIV output voltage for measurements at the position $[x, y] = [0, 10]$ (black line) and the position $[x, y] = [8, 10]$ (gray line). Right figure: analysis of these signals over a shorter duration and a narrow voltage band. The black line is linked to the left vertical axis while the gray one is linked to the right vertical axis.

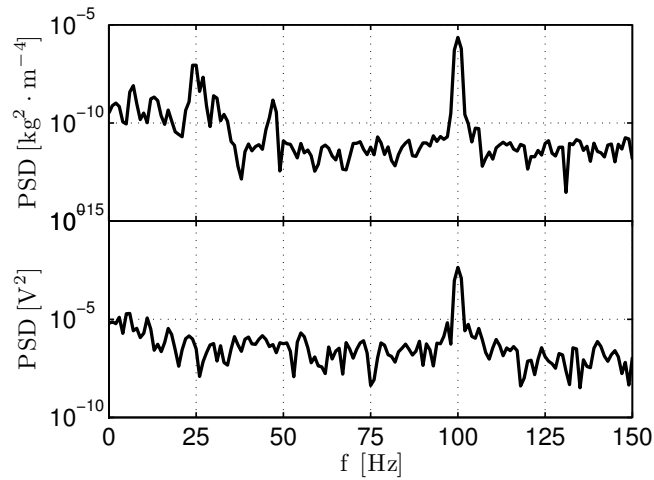


Figure 5.17 : PSD of the integrated density perturbation $\langle \rho' \rangle L$ measured at the position $[x, y] = [0, 10]$ (top figure) and the light intensity measured by PM (bottom figure).

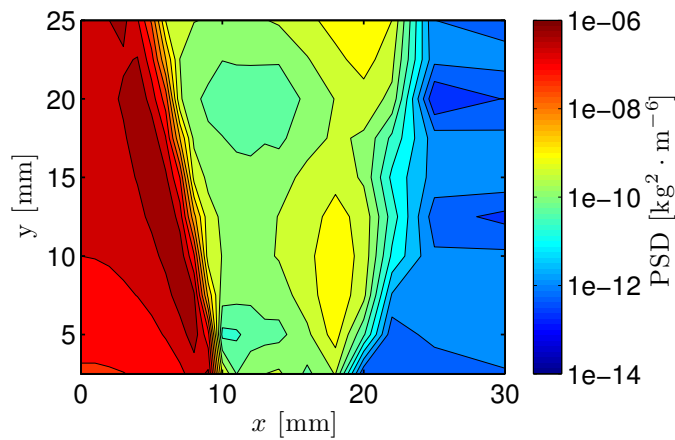


Figure 5.18 : Contour plot of the PSD peak value examined at $f = 100$ Hz from the LIV signal of half of the flame imaged in Fig. 5.15.

positions. Integrated density fluctuations $\langle \rho' \rangle L$ vary sharply near the flame front and may cause a large deflection of the laser beam. This phenomenon produces a bias in the fringes count of the LIV system. Figure 5.16 shows the output from LIV at two positions. The first is located inside the flame and the second lies around the flame front. Measurements inside the flame feature a regular periodic oscillation when the flow is modulated harmonically. But records around the flame front are different. The mean tension decreases quickly with time (sometimes increases), and goes beyond the limitation of the output [-3V

3V] causing errors. This phenomenon is caused by the accumulation of bias error with time. Due to these limitations, it is not possible to record data over a long time period. Adjusting the gain of the amplifier of the LIV may be used to reduce this phenomenon, but this is still limited by the precision of the A/D converter (5 mV) as shown in the right part in Fig. 5.16. Optimal conditions result from a trade-off between the limiting conditions.

In the following measurements, data from LIV and photomultiplier are sampled with the same frequency $f_s = 8192$ Hz over $t_s = 1$ ms. The gains of the LIV are continuously adjusted to optimize precision. The signal from the wave generator is also recorded to synchronize the PM and LIV devices. The power spectra of the resulting integrated density fluctuations $\langle \rho' \rangle_L$ and light intensity I are shown in Fig. 5.17. Low frequency disturbances induced by buoyancy forces are minimized by the quartz tube. The noise at low frequency in the LIV signal can be filtered by a high-pass filter. The peak value at the modulation frequency $f = 100$ Hz indicates the level of fluctuation at this frequency. This peak value is extracted from each measurement and mapped onto Fig. 5.18. Although the SNR in region outside the flame zone is small, useful information can still be extracted from this figure. It demonstrates that large density fluctuations are limited to region within the flame zone while fluctuations decrease in the burned gases and ambient air. The magnitude of the density fluctuations around the interface between the burned gases and ambient air are of the same order as those in the vicinity of the flame front. This constitutes a source of disturbances to infer heat release rate perturbations and will be discussed in Chapter 7.

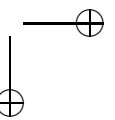
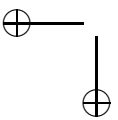
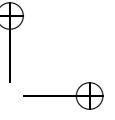
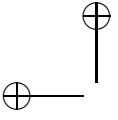
5.4 Conclusion

A Laser Interferometric Vibrometer often used for measurements of surface vibration without any contact was employed in this work to probe reacting flows. This technique is based on the principle of a Mach-Zehnder interferometer. Disturbances in the phase difference between the two laser beams are directly linked to integrated density perturbations along the optical path of the object beam when the geometry of the optical path is fixed.

This technique was first used to detect sound waves originating in a quiescent flow at the burner outlet. Results were compared with those measured by a microphone at the same location. A proportional link was found between the two results which does not depend on the sound frequency demonstrating that the LIV technique can be used to measure density fluctuations induced by acoustic excitation. Density fluctuations in a hot jet were then examined by LIV. The hot jet was produced by a laminar conical premixed flame confined in a quartz tube. The contour plots of resulting integrated density fluctuations \langle

CHAP. 5 - PROBING REACTING FLOWS WITH A LASER INTERFEROMETRIC VIBROMETER 107

$\rho' > L$ and resulting local density fluctuations ρ' deduced from LIV at different measurement positions show that the regions where the hot jet mixed with ambient air feature the largest density perturbations. Finally, LIV was used to detect integrated density fluctuations in pulsated flames. Results show that this technique can be well used to probe unsteady flames. The settings of the LIV system were optimized. The output signal from the LIV features a low frequency background noise with a main peak around 25 Hz and few harmonics. Measurements using LIV at higher frequencies ($f > 50$ Hz) are preferred to avoid these interactions with background noise. Density changes sharply near the flame front and may cause a large deflection of the laser beam. Off-axis measurements in these regions should be avoided to minimize this phenomenon.



Chapter 6

Determination of flame front wrinkling

Laser Interferometry Vibrometry (LIV) is used to detect flame front wrinkling. It is shown here that fluctuations of flame front position are proportional to line-of-sight integrated density perturbations when the disturbances in the density of burned gases and fresh mixture are neglected. Validations are conducted on different laminar premixed conical flames submitted to harmonic flow velocity modulations. This includes flames with different heights H varying from 30 mm to 54 mm, different equivalence ratios ϕ varying from 0.85 to 1.20, confinement tubes with different inner diameters D varying from 27 mm to 50 mm, different modulation frequencies f varying from 20 Hz to 300 Hz and modulation amplitudes $v_{u,rms}/\bar{v}_u$ varying from 0.04 to 0.35. The position of flame front obtained with the LIV are then compared with those deduced from images obtained with an intensified CCD camera.

6.1 Introduction

Measurement of flame front motion is a key issue to understand and model the burning velocity of turbulent premixed flames (Clavin 1985; Sinibaldi et al. 1998; Peters 2000). These data are also important for analysis of combustion dynamics to predict self-sustained combustion oscillations (Candel 2002). The development of diagnostics to estimate flame wrinkling is thus an active research area. The motion of flame front is generally deduced by measuring the evolution of the position of some flame markers with time. For premixed flames, it was shown that the position of chemiluminescence emission matches well with the HCO radical concentration which is a good marker of the flame heat release rate (Najm et al. 1998). Therefore, by recording the flame light emission with a camera, one is able to determine the flame front motion. The HCO radi-

cal does not feature natural chemiluminescence, it is then natural to examine the emission of other radicals present within the flame front. This is generally done by examining the distribution of OH^* , CH^* or C_2^* (Gaydon 1957). However, this method has a limited spatial resolution since the techniques based on the chemiluminescence emission yields a line-of-sight integrated information. For axisymmetric systems, it is however possible to reconstruct the flame front position in vertical axial plane using an Abel deconvolution (Walsh et al. 2000).

One possibility to improve spatial resolution is to use Laser Induced Fluorescence (LIF) by exciting radicals present in the reactive region with a laser sheet intersecting the flame front. OH LIF is often used because the OH peak mole fraction occurs in the burned gases just behind the reaction zone and the gradients of the fluorescence signal are found to match well with the position of local flame front (see for example Knikker et al. (2002)). The CH fluorescence signal is a better tracer of the reaction zone due to its relatively short lifetime and its abundance over a narrow region in the flame zone (Nguyen and Paul 1996; Donbar et al. 2000). The CH fluorescence signal is however more difficult to obtain than OH fluorescence which can easily be excited with Nd:YAG lasers widespread worldwide. Time resolved data based on stimulated fluorescence emission are more difficult to obtain due to the limited repetition rates and energy delivered per pulse from the lasers, although OH and CH planar measurements at a few kHz were recently reported to characterize transient phenomena in complex turbulent reacting flows (see for example Tanahashi et al. (2008); Boxx et al. (2009); Stöhr et al. (2011)). Besides, these techniques are difficult to apply for combustion control purposes because they require multiple sophisticated optical devices such as high-energy lasers, intensified CCD cameras and large optical access.

Laser Interferometric Vibrometry (LIV) is an alternative technique, easy to handle and operate, enabling measurements of time resolved data at very high frequency. As demonstrated in chapter 5, LIV yields reliable measurements of line-of-sight integrated density fluctuations along the optic path through flames. Density changes in ambient air along the optical path are neglected compared to those in flames. Only the fresh mixture, flame and burned gases are taken into account in the model schematically presented in Fig. 6.1. Fresh mixture and burned gases are characterized by the density ρ_u and ρ_b over the length L_u and $L - L_u$. The flame thickness is here neglected and therefore, the line-of-sight integrated density along the optical path can be expressed as:

$$\langle \rho \rangle L = \int_{L_u} \rho_u dz + \int_{L-L_u} \rho_b dz \quad (6.1)$$

When changes in the density of burned gases and fresh mixtures are neglected compared to the wrinkling of the flame interface, one obtains for first-order

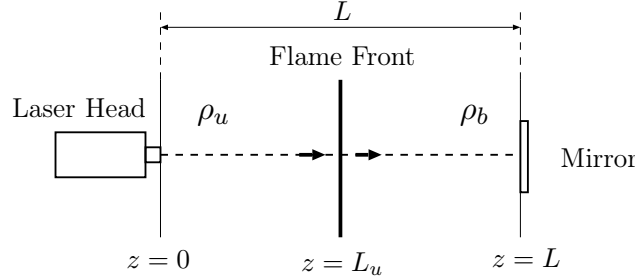


Figure 6.1 : Schematic view of fresh mixtures and burnt gases characterized by different densities between the laser head and mirror.

perturbations:

$$\langle \rho' \rangle L = L'_u(\rho_u - \rho_b) \quad (6.2)$$

where, L'_u is the perturbation of the flame front position. This expression yields a relation between the flame front motion and line-of-sight integrated density fluctuations. In this chapter, the LIV is used to measure $\langle \rho' \rangle L$, and the resulting information is used to estimate disturbances in the flame front position L'_u . An intensified CCD camera (ICCD) recording the chemiluminescence emission serves as a reference technique to compare the results obtained with LIV. The experimental configuration is presented in Section 2. The method used to determine the flame motion from the ICCD images is then described in Section 3. Tests carried on flames working at different conditions are then presented in Section 4 to validate the proposed technique. Conclusions are drawn in Section 5.

6.2 Experimental configuration

The setup is presented in Fig. 6.2 . Experiments are conducted on the axisymmetric burner presented in Chapter 1 with a cylindrical quartz tube on the top of the burner to confine the flame. Three tubes with different inner diameters can be used to examine their effects on the results. The geometrical characteristics of the tubes are described in Tab. 6.1. Experiments are conducted for flames with different equivalence ratios and heights by modifying the flowrate. The conditions explored are presented in Tab. 6.2. One first observes that the flame tube changes the shape of the steady flame. This is for example shown in Fig. 6.3 for the flame confined with the tube (Tube-1) featuring the smallest diameter $D = 27$ mm. The burned gases around the flame in this case cannot fully expand and are directly in contact with the quartz. The conical shape of the flame is then slightly bent due to the pressure of the burned gases acting

on the flame and causing a vertical acceleration of the fresh gases in the center-line (Higuera 2009). For the flame presented in Fig. 6.3 (Flame-2-1), the flame

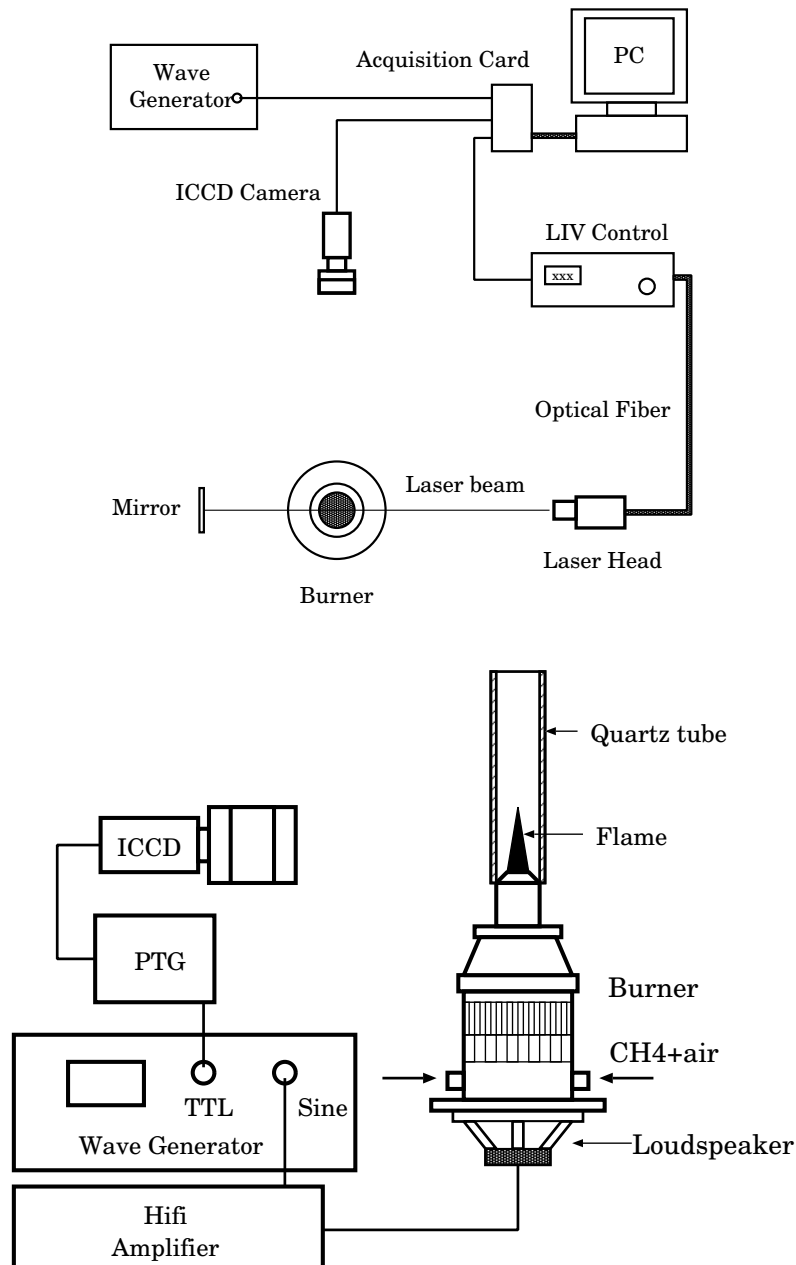


Figure 6.2 : Schematic of the experimental setup: (a) Arrangement of measurement devices. (b) Details of the configuration with the ICCD camera.

height is stretched from $H = 37$ mm in the absence of tube to $H = 42$ mm with Tube-1.

Table 6.1 : Quartz flame tube information.

Tube	Inner diameter [mm]	Length [mm]
Tube-1	27	150
Tube-2	36	120
Tube-3	50	300

Harmonic signals from the wave synthesizer are used to drive the loudspeaker placed at the base of the burner while a synchronized TTL signal enables to trigger the ICCD camera. A total of 200 snapshots with the same phase are accumulated onto the CCD array of the camera and saved by the computer. The laser head and the mirror of the LIV are well aligned so that the laser beam crosses the symmetry axis of the flame. A cylindrical coordinate system is used to locate the flame front position where r indicates the radial distance to the flame front from the burner axis and $y = 0$ indicates the burner outlet. Measurements at different vertical positions are realized by moving the burner along the vertical direction using the micrometric displacement table. The harmonic forcing signal driving the loudspeaker together with the output from the LIV system are digitized by the A/D converter and recorded by the computer.

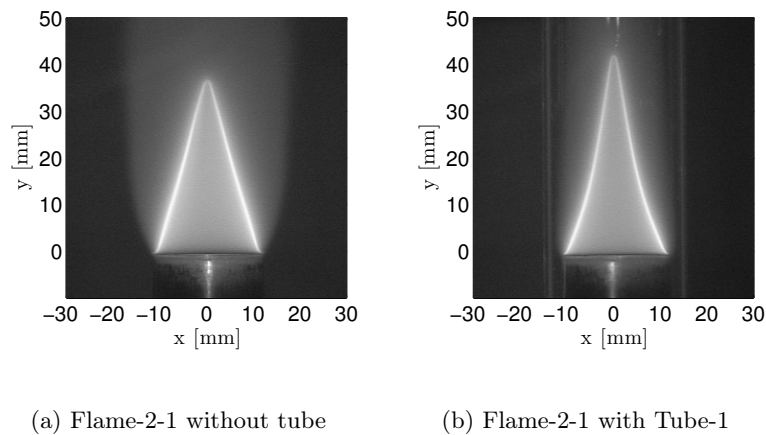


Figure 6.3 : Steady flame without quartz tube (left, flame height $H = 37$ mm) and with the Tube-1 (right, flame height $H = 42$ mm).

Table 6.2 : *Flame operating conditions.*

Flame	Equivalence ratio ϕ [-]	Flow velocity \bar{v}_u [m·s ⁻¹]	Flame height in Tube-1 H [mm]
Flame-1	1.00	1.06	30
Flame-2-1	1.00	1.50	42
Flame-3	1.00	1.91	54
Flame-2-2	0.85	1.06	42
Flame-2-3	1.20	1.35	42

6.3 Processing of chemiluminescence images

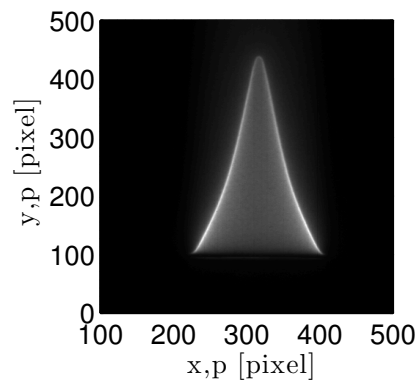


Figure 6.4 : *Example of image collected with the ICCD camera. Steady Flame-2-1 with Tube-1.*

Images generated by the ICCD camera consist of a matrix of 512×512 square pixels. Each pixel contains a value proportional to the line-of-sight integrated light intensity collected of the flame chemiluminescence (see for example figure 6.4). As indicated in the introduction, it is assumed that the radial position of flame front is located where the distribution of the chemiluminescence intensity is maximal. Since the configuration explored features a cylindrical symmetry along the burner axis, an Abel transformation is applied to each frame to obtain the radial intensity distribution in a plane parallel to the camera CCD array crossing the burner axis. Data processing includes two stages. The optical magnification is first determined, i.e., the ratio between the number of the

pixels in the image and the real flame size in both directions is first calculated using a reference image. The Abel inversion is then applied and the position of the flame front is measured.

6.3.1 Flame location

It is necessary to identify the axis of the flame in the image. Since the flame is symmetrical, the pixel value along the radial direction also features a symmetrical distribution along the burner axis as shown in Fig. 6.5(a). Raw data and filtered result are both shown in this figure. Two symmetric peaks can be found and the mean value of the pixels indicating the left and right maximum values can be considered as the position of symmetry axis. The burner axis is determined with this method and the result is shown in Fig. 6.5(b). The dotted lines in the flame zone indicate the axis of the flame. The bottom of the flame is defined by the burner exit in the image.

6.3.2 Calculation of the optical magnification

The size of the flame is determined using the following procedure. This can be done by recording images of a steady flame at different vertical positions by decreasing the height of the burner progressively by steps of 5 mm using the micrometric displacement table. The displacement in the image can then

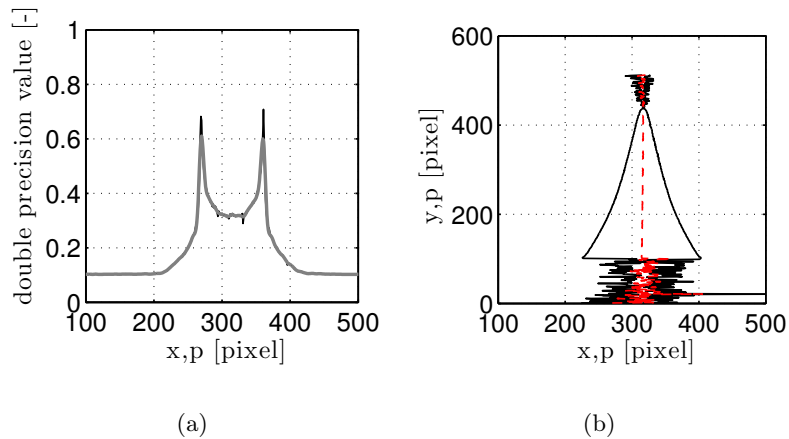


Figure 6.5 : (a) Pixel value distribution along the radial direction at the vertical location $y = 200$ pixels. The black line indicates the raw signal and the gray one is the filtered signal. (b) Distribution of the maximum pixel values (solid lines) and the corresponding symmetry axis (dotted lines).

be determined by the cross-correlation of two images recorded at two different positions as shown in Fig. 6.6(a). The position of the maximum value indicates the vertical displacement. It is then possible to plot the displacement in the image versus the real displacement of the flame. Results are shown in Fig. 6.6(b). The scaling factor can be calculated by a linear regression of the data. One finds here $8.1 \text{ pixels}\cdot\text{mm}^{-1}$.

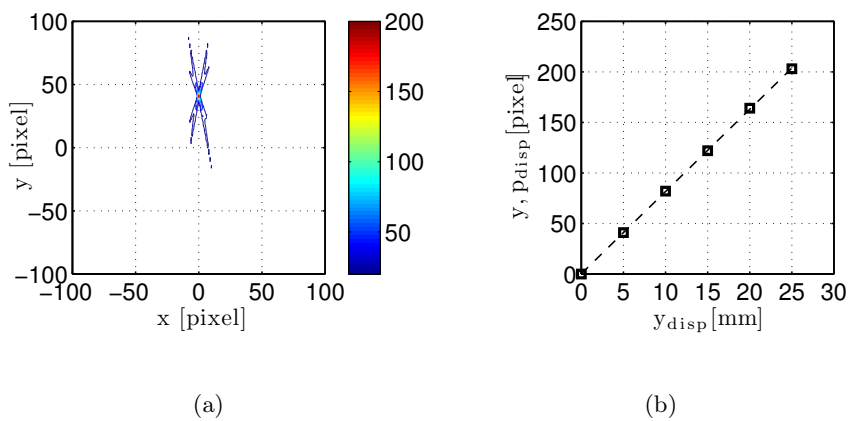


Figure 6.6 : (a) Cross-correlation between two images of a steady flame at two vertical positions separated by a displacement $y_{disp} = 5 \text{ mm}$. The position of the maximum pixel value indicates the displacement of the flame in the image y, p_{disp} . (b) Plot of the pixel displacement in the image (unit: pixel) versus flame displacement imposed by the micrometric displacement system (unit: mm).

6.3.3 Abel inversion

Raw images collected with the ICCD camera are now post-processed using the Abel transformation Eq. (5.19) without any regularization due to the high SNR. Figure 6.7 shows examples of raw images at four instants in a modulation cycle for a flame perturbed at a frequency $f = 100 \text{ Hz}$ and a forcing level $v_{u,rms}/\bar{v}_u = 0.21$. The flame front executes large deformations where a flame pocket is produced in the first image. The Abel inversion of these images is presented in the Fig. 6.8. The flame front is highlighted in the transformed images. Another example with a higher modulation frequency $f = 200 \text{ Hz}$ is shown in Fig. 6.9 with the resulting transformation presented in Fig. 6.10.

It is then possible to extract the flame front positions at different vertical positions and plot its evolution with time. Herein, the mean location of the left and right fronts is taken as the flame front position r with respect to the symmetry

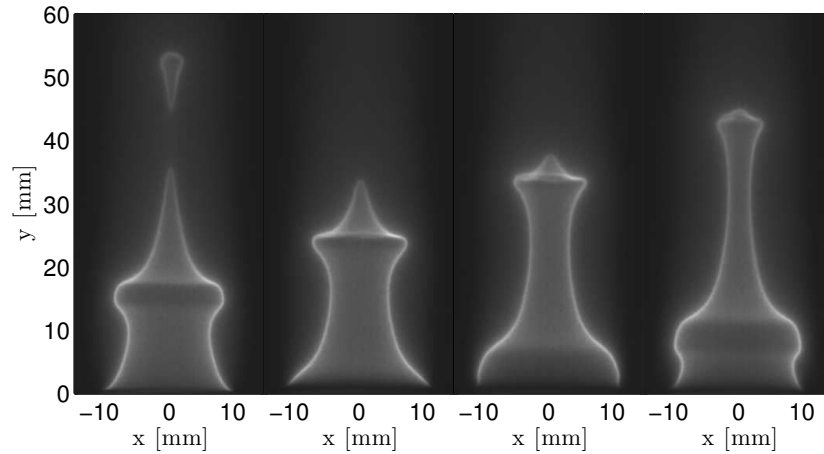


Figure 6.7 : Raw phase conditioned images collected with the ICCD camera of a pulsated flame at four instants in the forcing cycle. From left to right: $t/T = 1/20, 6/20, 11/20$ and $16/20$, where $T = 1/f$. Flame-2-1. Tube-1. $f = 100$ Hz, $v_{u,rms}/\bar{v}_u = 0.21$.

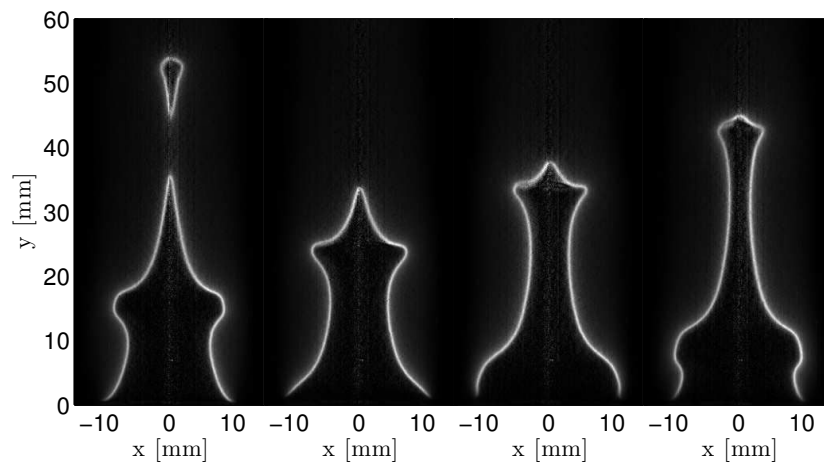


Figure 6.8 : Abel inversion of the images shown in Fig. 6.7.

axis. Figure 6.11 shows two examples of results at different heights y . The flame front position executes a periodic motion at the same frequency as the forcing one. This technique performs well near the flame base and for heights limited to about $y \leq 35$ mm in the different conditions explored. Near the flame tip, the SNR drops close to the symmetry axis $x = 0$ of the flame where the Abel transformation is not defined (See Eq. (5.19)).

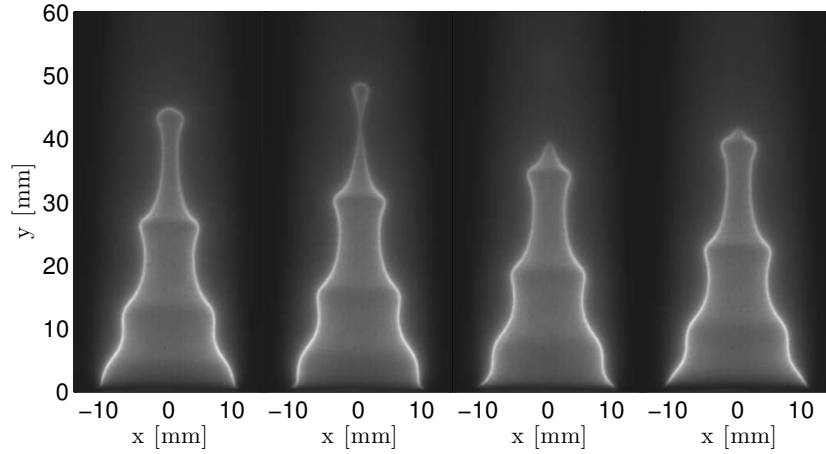


Figure 6.9 : Raw phase conditioned images collected with the ICCD camera of a pulsated flame at four instants in the forcing cycle. From left to right: $t/T = 1/20, 6/20, 11/20$ and $16/20$, where $T = 1/f$. Flame-2-1. Tube-1. $f = 200$ Hz, $v_{u,rms}/\bar{v}_u = 0.11$.

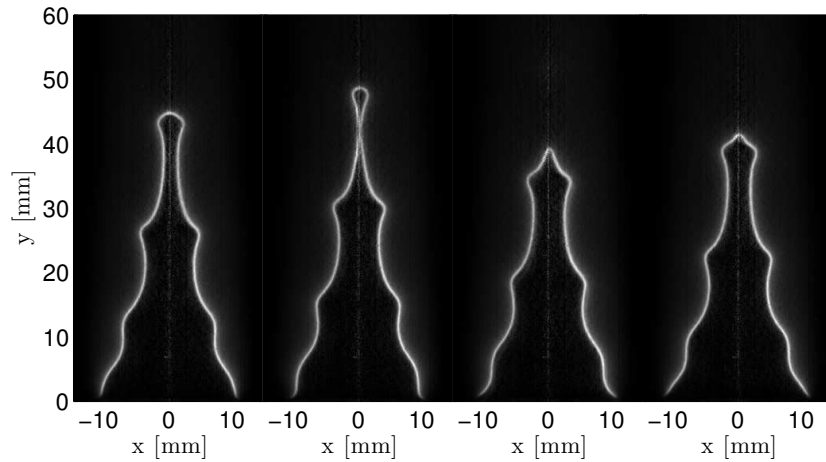


Figure 6.10 : Abel inversion of the images shown in Fig. 6.9.

6.4 Results and discussion

Records with the ICCD camera and measurements of line-of-sight integrated density fluctuations with LIV are carried out separately. LIV measurements are done at five different heights above the burner from $y = 5$ mm to 25 mm separated by 5 mm increments along the burner axis. The signal from the wave generator serves as a reference to synchronize all signals. In these experiments, the signals from the LIV and wave generator are sampled at the same frequency $f_s = 8192$ Hz during 10 s. The output voltage from LIV is then converted to

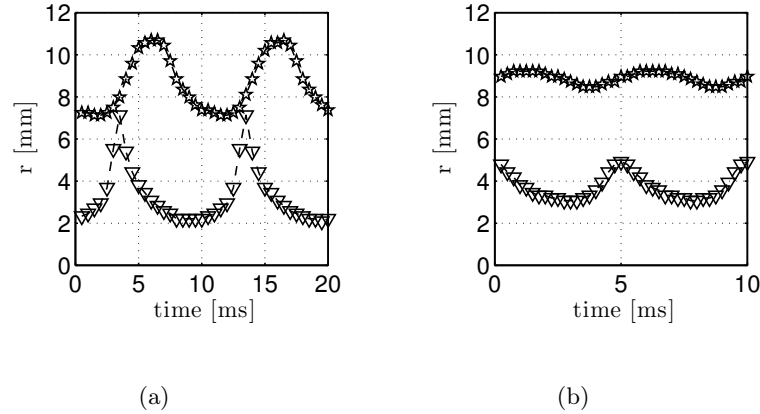


Figure 6.11 : Evolution of the flame front oscillation at two vertical positions $y = 5$ mm (marker \star) and $y = 25$ mm (marker ∇). Flame-2-1. Tube-1. (a) Modulation at $f = 100$ Hz, $v_{u,rms}/\bar{v}_u = 0.21$. (b) Modulation at $f = 200$ Hz, $v_{u,rms}/\bar{v}_u = 0.11$.

line-of-sight integrated density fluctuations using Eq. (5.8). It was shown in Chapter 5 that this signal contains noise at low frequency. A high-pass zero-phase shift filter with a cut-off frequency equal to $f/2$ is then applied to filter the LIV signal, where f is the modulation frequency. It is then compared with the flame front oscillation deduced from the ICCD images. Comparisons between the two techniques at five vertical positions are presented in Figs. 6.12 to 6.15 for eight cases for different flow operating and perturbation conditions. Signals in these figures are rescaled to obtain comparable oscillations levels. The two signals always correlate well for the 8 cases explored. The effects of modulation level, modulation frequency, flame height and flame equivalence ratio are analyzed in the remaining part of this chapter.

For a flame with a given modulation frequency, a modification of the modulation level alters the amplitude of the motion of the flame front oscillation. This is used to investigate the sensitivity of the LIV technique. Flames submitted to small perturbation only respond with a small oscillation of the flame front which is difficult to detect in the ICCD images due to the limitation of resolution in these images. This is for example highlighted in the bottom graph in Fig. 6.13(b) for Flame-2-1 at the forcing frequency $f = 200$ Hz with a perturbation level $v_{u,rms}/\bar{v}_u = 0.07$. LIV enables to easily retrieve the fluctuation while the detection based on flame images is more difficult to interpret. Another issue is to validate whether the LIV technique performs well at higher modulation levels. Figure 6.12 shows results for Flame-2-1 modulated at $f = 100$ Hz with two perturbation amplitudes $v_{u,rms}/\bar{v}_u = 0.07$ and 0.21 . The

flame front motion executes a quasi-harmonic response near the flame base at small to moderate perturbation levels. This response exhibits sharper angles as the height above the burner or when the perturbation level is increased. It is however clearly shown in Fig. 6.12 that LIV enables to capture the flame front motions at different vertical positions when the perturbation amplitude is increased. As demonstrated in Eq. (6.2), line-of-sight integrated density perturbations $\langle \rho' \rangle L$ are proportional to flame front wrinkles L'_u with a coefficient $(\rho_u - \rho_b)$. In these experiments, the optical path crosses two flame fronts. The radius r_i is used to represent the flame front location with respect to the burner axis, and therefore, $L'_u = 2r'_i$. The proportionality coefficient between $\langle \rho' \rangle L$

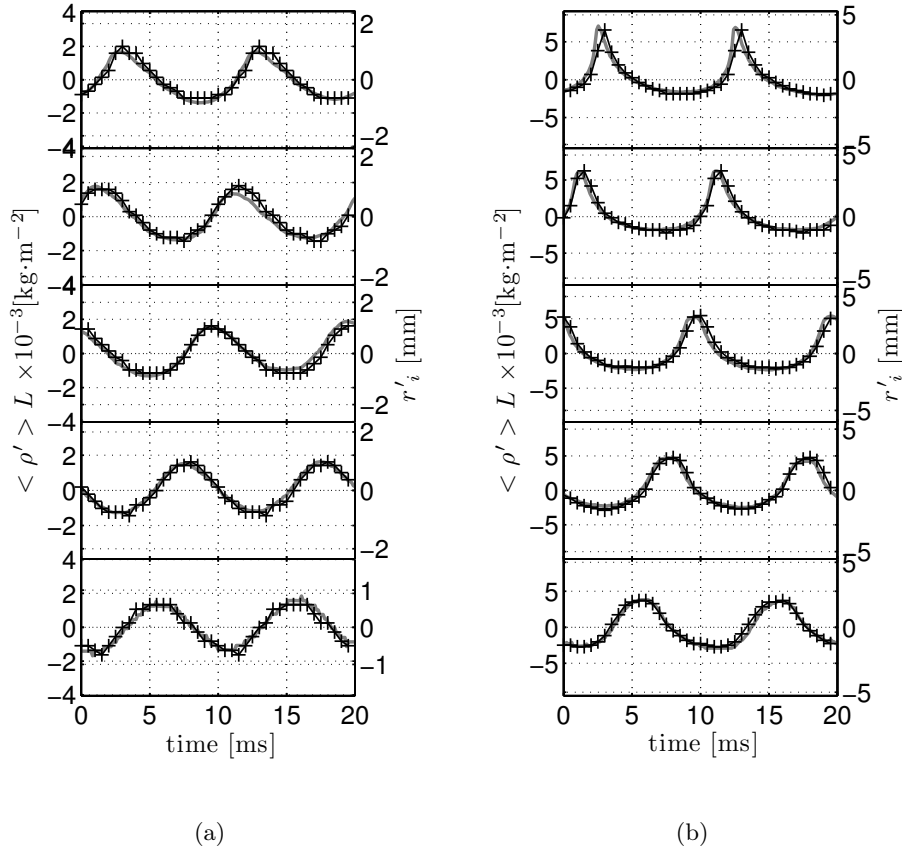


Figure 6.12 : Comparison between line-of-sight integrated density fluctuations $\langle \rho' \rangle L$ (solid line) and flame front oscillations r'_i deduced from ICCD images (marker +) at five vertical positions, $y=5$ to 25 mm by increments of 5 mm from bottom to top. Flame-2-1. Tube-1. (a) Modulation at $f = 100$ Hz, $v_{u,rms}/\bar{v}_u = 0.07$. (b) Modulation at $f = 100$ Hz, $v_{u,rms}/\bar{v}_u = 0.21$.

and r'_i is now given by $2(\rho_u - \rho_b)$. The link between the two signals $\langle \rho' \rangle L$ and r'_i can be examined by plotting the r.m.s values of the two signals measured at the different vertical positions and different modulation amplitudes investigated. Results presented in Fig. 6.16 for the two modulation frequencies $f = 100$ Hz and 150 Hz clearly validate this relation between these two signals. Figure 6.16(a) indicates that the proportionality coefficient may slightly vary at the different measurement positions for a given forcing frequency. This difference may be attributed to the calculation of the r.m.s value of these signals which is still contaminated by other frequencies even after the high-pass filtering. This phenomenon is however very limited and the two signals generally

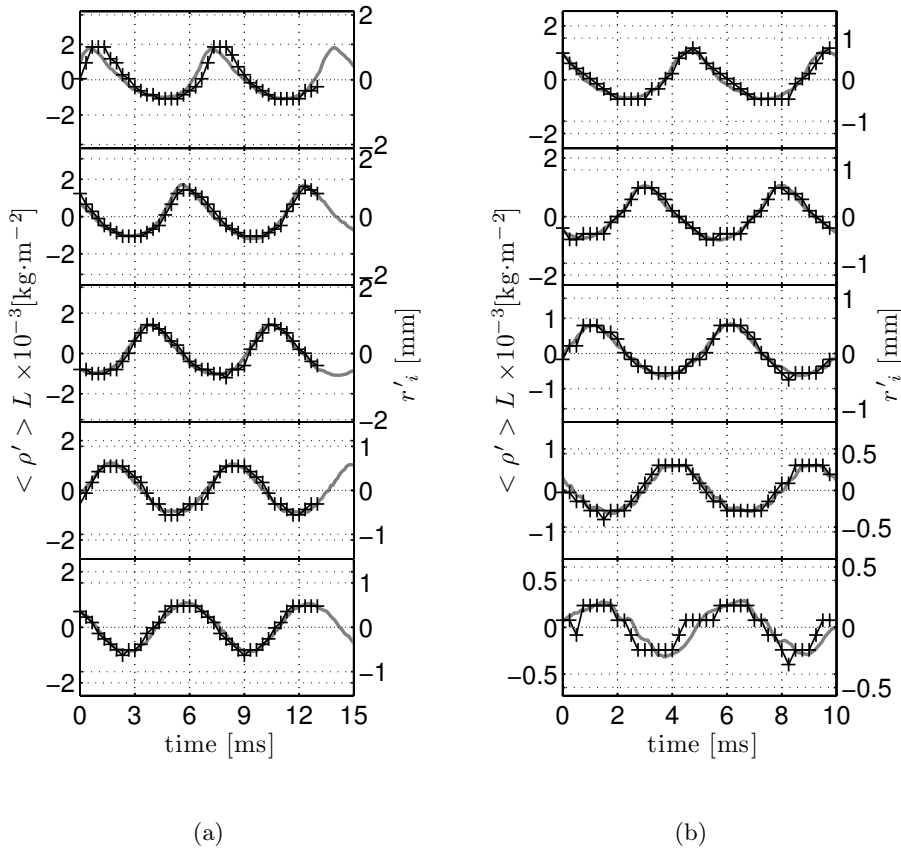


Figure 6.13 : Comparison between line-of-sight integrated density fluctuations $\langle \rho' \rangle L$ (solid line) and flame front oscillations r'_i deduced from ICCD images (marker +) at five vertical positions, $y=5$ to 25 mm by increments of 5 mm from bottom to top. Flame-2-1. Tube-1. (a) Modulation at $f = 150$ Hz, $v_{u,rms}/\bar{v}_u = 0.07$. (b) Modulation at $f = 200$ Hz, $v_{u,rms}/\bar{v}_u = 0.07$.

can be considered proportional. When the modulation frequency increases, the amplitude of the displacement of the flame front decreases. This is highlighted by comparing results in the Figs. 6.12(a), 6.13(a) and 6.13(b).

It is interesting to examine the proportionality coefficient $\langle \rho' \rangle L_{rms} / r_{i,rms}$ in more details. This value can be estimated by a linear regression of the r.m.s values of the data collected for increasing forcing levels and a fixed modulation frequency. For the data shown in Fig. 6.16, this value both equals to $1.8 \text{ kg}\cdot\text{m}^{-3}$ which is not far from the theoretical prediction $2(\rho_u - \rho_b) = 2(1 - T_u/T_b)\rho_u \approx 1.98 \text{ kg}\cdot\text{m}^{-3}$. The difference may be attributed to interaction of the flame with

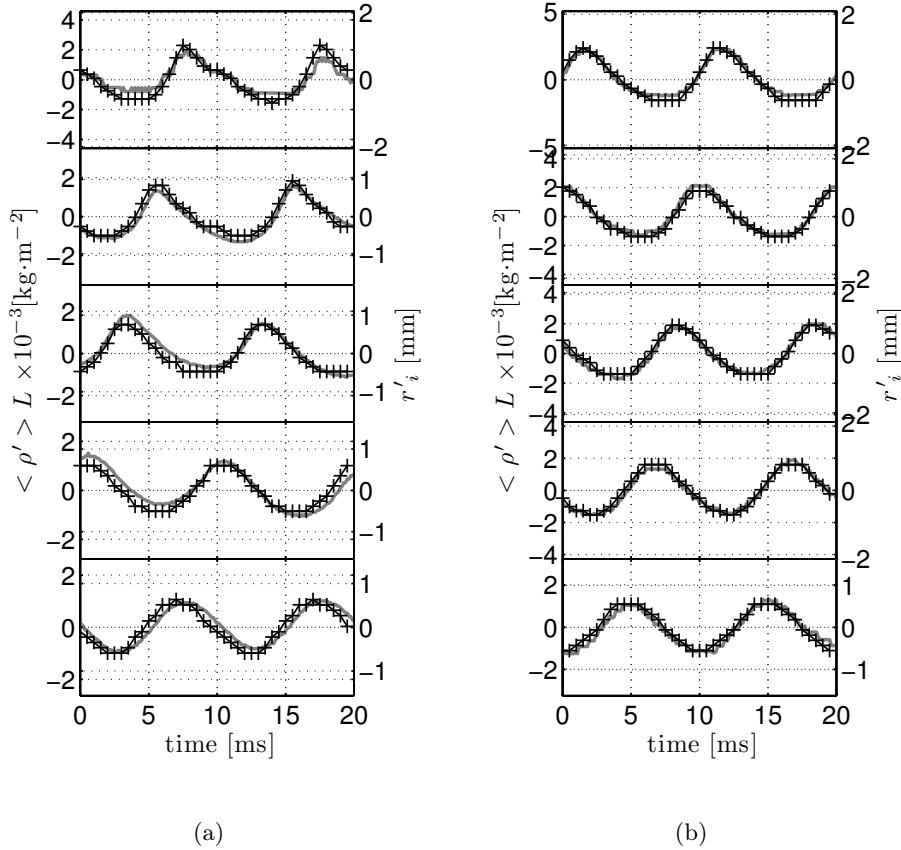


Figure 6.14 : Comparison between line-of-sight integrated density fluctuations $\langle \rho' \rangle L$ (solid line) and flame front oscillations r'_i deduced from ICCD images (marker +) at five vertical positions, $y=5$ to 25 mm by increments of 5 mm from bottom to top. (a) Flame-1. Tube-1. Modulation at $f = 100$ Hz, $v_{u,rms}/\bar{v}_u = 0.07$. (b) Flame-3. Tube-1. Modulation at $f = 100$ Hz, $v_{u,rms}/\bar{v}_u = 0.07$.

the quartz tube where heat losses take place. The hot gases temperature is then slightly lower than the adiabatic flame temperature used to estimate this coefficient. It is also worth examining whether this value is dependent on the modulation frequency. Tests are done on Flame-2-1 with modulation frequencies varying from 20 to 200 Hz. Figure 6.17 plots $\langle \rho' \rangle L_{rms}$ as a function of $r_{i,rms}$ at the position $y = 15$ mm for the different cases explored. Data collapse on a single line indicating that the proportionality coefficient is independent of modulation frequency.

Flames featuring different mean flow operating conditions are also investigated.

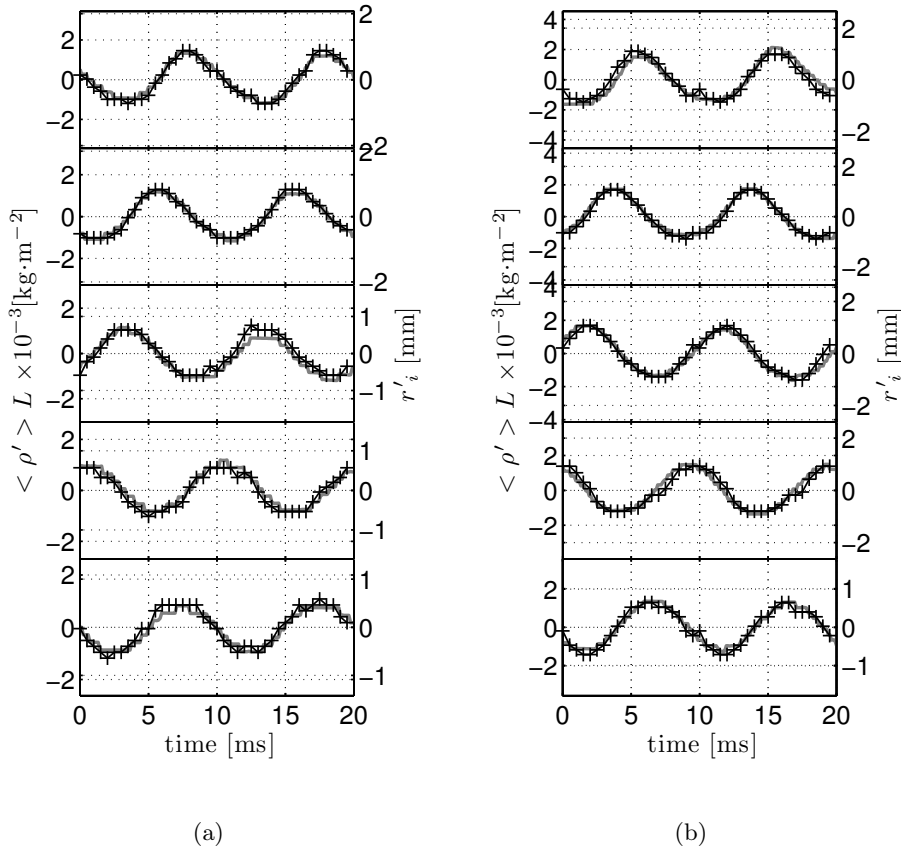


Figure 6.15 : Comparison between line-of-sight integrated density fluctuations $\langle \rho' \rangle L$ (solid line) and flame front oscillations r'_i deduced from ICCD images (marker +) at five vertical positions, $y=5$ to 25 mm by increments of 5 mm from bottom to top. (a) Flame-2-2. Tube-1. Modulation at $f = 100$ Hz, $v_{u,rms}/\bar{v}_u = 0.07$. (b) Flame-2-3. Tube-1. Modulation at $f = 100$ Hz, $v_{u,rms}/\bar{v}_u = 0.07$.

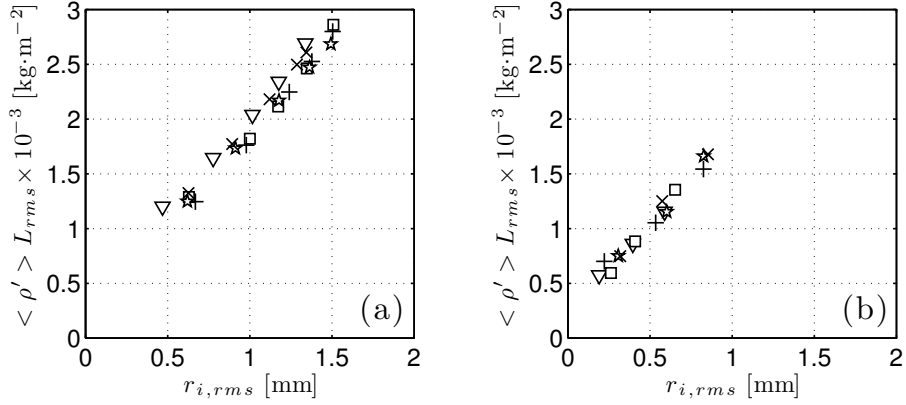
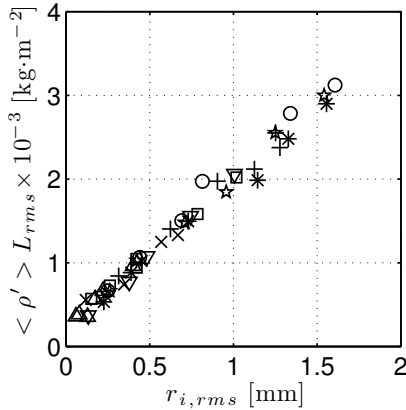


Figure 6.16 : Plot of the r.m.s value of line-of-sight integrated density fluctuations ($\langle \rho' \rangle L$)_{rms} as a function of perturbations in the flame front position $r_{i,rms}$. Markers ∇ , \square , $+$, \star and \times indicate results measured from $y = 5$ to 25 mm by increments of 5 mm. Flame-2-1. Tube-1. (a) $f = 100$ Hz, $v_{u,rms}/\bar{v}_u$ varies from 0.07 to 0.21. (b) $f = 200$ Hz, $v_{u,rms}/\bar{v}_u$ varies from 0.04 to 0.11.



Marker	Modulation frequency f [Hz]	Modulation level $v_{u,rms}/\bar{v}_u$ [-]
∇	20	0.04 \rightarrow 0.28
\square	40	0.04 \rightarrow 0.28
*	50	0.04 \rightarrow 0.35
\star	60	0.04 \rightarrow 0.28
\circ	80	0.04 \rightarrow 0.28
$+$	100	0.04 \rightarrow 0.21
\times	150	0.02 \rightarrow 0.11
\triangle	200	0.02 \rightarrow 0.11

Figure 6.17 : Plot of the r.m.s value of line-of-sight integrated density fluctuations ($\langle \rho' \rangle L$)_{rms} as a function of perturbations in flame front position $r_{i,rms}$. All the measurements are carried out at the vertical position $y = 15$ mm. The modulation frequency f varies from 20 to 200 Hz. Flame-2-1. Tube-1.

Measurements are carried out for flames with different heights but the same equivalence ratio. Figure 6.18(a) plots the r.m.s value of ($\langle \rho' \rangle L$)_{rms} as a function of $r_{i,rms}$ for Flame-1, Flame-2-2 and Flame-3. These data collapse on the same single line for Flame-1 and Flame-2-1. Data for Flame-3 lie above this

line indicating a higher proportionality coefficient. This is induced by the larger thermal power of Flame-3. In experiments conducted with Flame-3, ambient air surrounding the quartz tube is very hot and a natural convection flow takes place. These hot gases may also contribute to additional density perturbations which cannot be neglected in this case. Measurements are also conducted with flames featuring the same height but different equivalence ratio. Data in Fig. 6.18(b) fall again on the same line because changes in the mean density of the burned gases within the equivalence ratio band explored $\phi = 0.85$ to 1.20 are very small.

Measurements are also conducted for flames confined by tubes with different diameters (see Tab. 6.1). Flame front oscillations deduced from LIV technique still correlate well with data obtained from ICCD images. Plots of r.m.s values of the two signals for the different measurement locations and modulation amplitudes investigated are presented in Fig. 6.19. They show that the proportional link does not depend on the confinement.

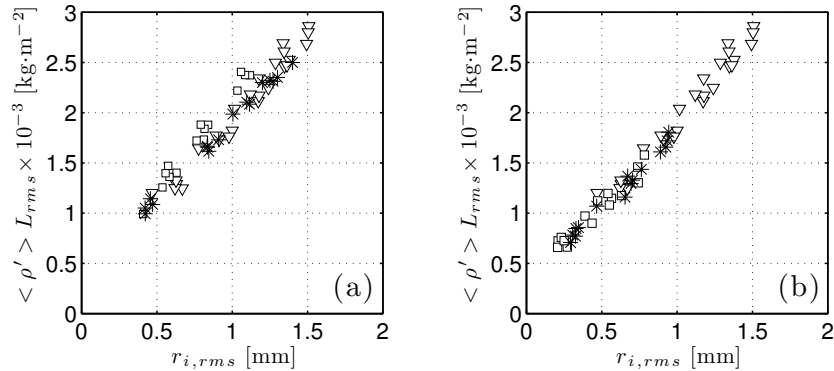


Figure 6.18 : Plot of the r.m.s value of line-of-sight integrated density fluctuations $(\langle \rho' \rangle L)_{rms}$ as a function of perturbations in the flame front position $r_{i,rms}$. The modulation frequency is kept constant 100 Hz. Flame-2-1. Tube-1.

Graph	Investigation	Marker	Flame	Modulation level $v_{u,rms}/\bar{v}_u$ [-]
(a)	Flame height	*	Flame-1	0.07 \rightarrow 0.28
		∇	Flame-2-1	0.07 \rightarrow 0.21
		\square	Flame-3	0.04 \rightarrow 0.11
(b)	Equivalence ratio	∇	Flame-2-1	0.07 \rightarrow 0.21
		\square	Flame-2-2	0.04 \rightarrow 0.11
		*	Flame-2-3	0.04 \rightarrow 0.11

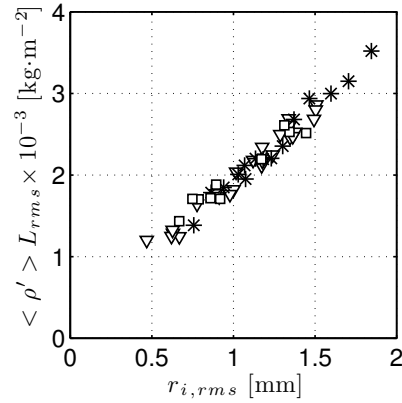


Figure 6.19 : Plot of r.m.s value of line-of-sight integrated density fluctuations $\langle \rho' \rangle L_{rms}$ as a function of perturbations in flame front position $r_{i,rms}$. Flame-2-1 modulated at $f = 100$ Hz. Markers ∇ , $*$ and \square indicate results for different confinement tubes Tube-1, Tube-2 and Tube-3 respectively.

6.5 Conclusion

It was shown that integrated density fluctuations measured by LIV along the optical path passing through pulsated flames can be used to estimate perturbations of the flame front position when density perturbations in the burned gases and fresh mixture can be neglected. An experimental validation was carried out on laminar premixed flames confined by cylindrical tubes with different diameters modulated by harmonic flowrate perturbations at different frequencies and amplitudes. Results from LIV were compared to those deduced from the ICCD images records. A linear relationship was been found between the data recorded with the two diagnostics in all investigated cases. This proportional link does not depend on the diameter of flame confinement tube, flame height, equivalence ratio, modulation frequency and modulation level.

Chapter 7

Determination of line-of-sight integrated heat release rate disturbances

A Laser Interferometric Vibrometer (LIV) is used in this chapter to determine time resolved density fluctuations. It is shown that density fluctuations in the flame region are mainly due to heat release rate perturbations. LIV is then used to estimate these heat release rate disturbances. The technique is validated in the case of pulsated laminar premixed flames. Measurements are compared to line-of-sight integrated chemiluminescence emission data collected with a CCD camera. A good agreement is obtained for harmonic flow modulations at different forcing frequencies and perturbation levels for flames operating at different flow conditions. This work validates the principle of this alternative technique for detecting heat release rate perturbations.

7.1 Introduction

When flames are wrinkled due for example to self-sustained oscillations or when they are submitted to flow modulations, this produces perturbations in the heat release rate which are accompanied by large density fluctuations in the reaction zone constituting important sound sources that radiate combustion noise. It is possible to link these perturbations by the following approximation (Candel et al. 2009):

$$\frac{\partial \rho'}{\partial t} = \frac{1}{c^2} \frac{\partial p'}{\partial t} - \frac{\gamma - 1}{c^2} \dot{q}' \quad (7.1)$$

where the density, pressure, speed of sound, specific heat capacities ratio and heat release rate per unit volume are represented by ρ , p , c , γ and \dot{q} , respectively. Mean and fluctuating components are denoted by the superscripts ($\bar{\quad}$) and

('). This equation is a simplified version for density fluctuations comprising acoustic and entropic contributions which are dominated in reactive flows by heat release rate disturbances (Dowling 1995; Candel et al. 2009). The first contribution from acoustic disturbances can be generally neglected compared to those induced by heat release rate disturbances and this enables to link the heat release rate fluctuations directly to density perturbations:

$$\frac{\partial \rho'}{\partial t} = -\frac{\gamma - 1}{c^2} \dot{q}' \quad (7.2)$$

This type of approximation was for example already used in some simulations of combustion noise emission (Ihme et al. 2009). It constitutes an interesting alternative to access to heat release rate fluctuations. Experimental validations have however not been envisaged yet.

Laser Interferometry Vibrometry has already been envisaged to determine density and density fluctuations in turbulent non reacting flows (Mayrhofer and Woisetschläger 2001; Woisetschläger et al. 2003; Hampel and Woisetschläger 2006; Köberl et al. 2010) as well as in perturbed reacting flows (Giuliani et al. 2007; Giuliani et al. 2010b). As demonstrated in Chapter 5, this technique yields a line-of-sight integrated measurement of the refractive index n which is linked to density ρ . Results obtained in Chapters 5 and 6 showed that this technique enables measurements of line-of-sight integrated density fluctuations $\langle \rho' \rangle_L$. These measurements are used here to estimate line-of-sight integrated heat release rate disturbances $\langle q' \rangle_L$ using Eq. (7.2). This type of investigation has already been carried out on a laminar premixed M-shape flame at EM2C by Giuliani et al. (2010a). Results were obtained on a qualitative basis by recording the evolution of the global chemiluminescence emission with a photomultiplier. Local measurements are conducted in this study and quantitative comparison will be made.

The experimental configuration is presented in Section 2. It includes a CCD camera to estimate line-of-sight integrated heat release rate disturbances from chemiluminescence emission. Comparisons between measurements gathered with the LIV and the CCD camera are presented in Section 3. Correlations are successively established between line-of-sight integrated chemiluminescence emission disturbances measured by the CCD camera and the signal from the LIV system for different conical flames submitted to flow modulations at different frequencies and forcing levels. Conclusions are made in the final section.

7.2 Experimental configuration

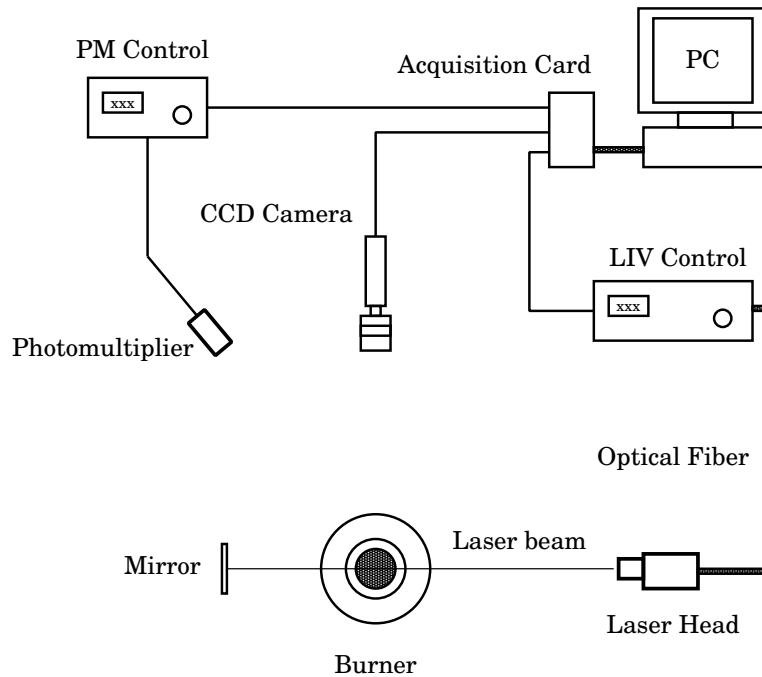


Figure 7.1 : Arrangement of the experimental setup.

The experimental setup is presented in Fig. 7.1. It is the same as in Chapter 6 with an additional CCD camera to record snapshots of the perturbed flames during the modulation cycle. Experiments are conducted with the axisymmetric burner presented in Chapter 1. A quartz tube is also placed on the top of the burner to confine the flame. The flow operating conditions explored are the same as in Chapter 6 (see Tab. 6.2) with different flame confinement tubes (see Tab. 6.1). Figure 7.2 shows the snapshots of the steady configuration Flame-2-1 within the small, intermediate and large tubes. As the radius of the tube decreases, the burned gases are more rapidly in contact with the quartz. This is used to eliminate the motion of the interface between the burned gases and ambient air. The burned gases surrounding the flame are in contact with the quartz tube over the entire flame length in the left image. Measurements are mainly conducted with this small tube diameter.

Snapshots of the pulsated flames are recorded by a CCD camera equipped with an electronic shutter to control the exposure time fixed to $1/4000$ s. As indicated in Chapter 1, this camera operates with a fixed sampling rate of 50 frames per second. The modulation frequency is here tuned close but not exactly to

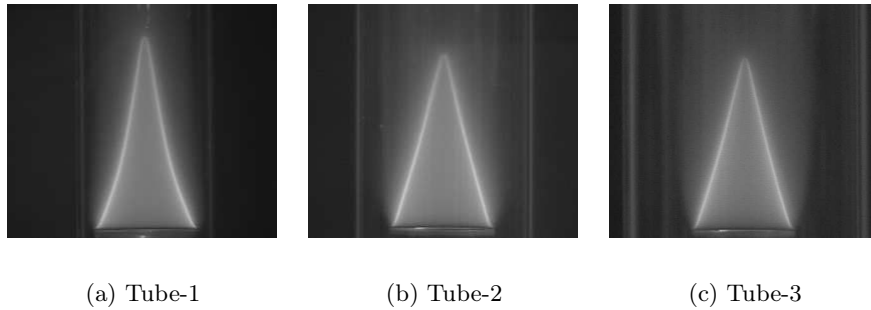


Figure 7.2 : *Steady flames confined by tubes with different diameters. Flame-2-1.*

a multiple of 50 Hz to obtain a stroboscopic effect. This method enables for example to record 20 phases per period for a flame modulated with a frequency 100.05 Hz. The focus of the camera is well adjusted to the size of the flame to maximize resolution on the CCD pixel array. Images are digitized with a matrix of 768×494 square pixels. The CCD is equipped with square pixels corresponding to an aspect ratio of unity. The micrometric displacement table is used to rescale the flame images with the method presented in Chapter 6 yielding 1 mm for 9.64 pixels in both directions. More than 400 images are recorded for each operating condition enabling to sort the images and reconstruct the evolution of flame motion at each phase in the modulation cycle. Due to the short exposure time, the SNR in the snapshots is improved by accumulating 4 images at the same phase to increase the contrast.

For well premixed flames in the absence of mixture composition inhomogeneities, perturbations in the chemiluminescence intensity I of free radicals OH^* , C_2^* or CH^* present in the flame front are proportional to heat release rate disturbances (Price et al. 1969; Schuller et al. 2002b):

$$\dot{Q} = kI \quad (7.3)$$

where k is constant for a given equivalence ratio ϕ and experimental setup. In this chapter, the photomultiplier PM and the CCD camera are both used to record the chemiluminescence intensity from the flame. The PM featuring a large solid angle yields a signal integrated over the entire field of view, while the camera gives a line-of-sight integrated information. Each pixel from the color image of the CCD camera is converted to a double precision number measuring the total light intensity cumulated on the pixel. The summation of the values of all pixels in the image yields the global light intensity I_{CCD} measured by the camera. This quantity can be compared to the light intensity I_{PM} recorded by

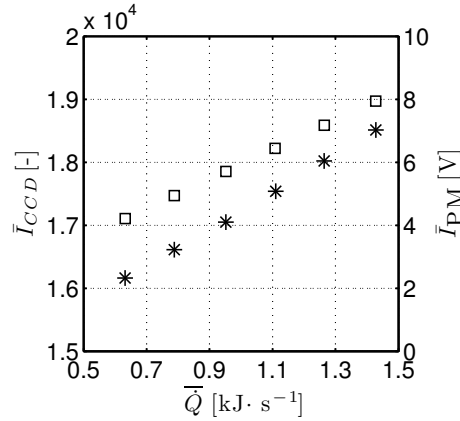


Figure 7.3 : Plot of summation of light intensity \bar{I} of all pixels recorded by CCD camera (marker \square) and the photomultiplier signal (marker $*$) versus heat release rate \bar{Q} . These data were obtained from the flames with the same equivalence ratio $\phi = 1.00$ by increasing the flowrate.

the PM. By modifying the mean flow velocity at the burner outlet, it is possible to examine the evolutions of the signals I_{PM} and I_{CCD} as a function of the heat release rate calculated by $\bar{Q} = \rho_u \bar{v}_u A \Delta q$, where ρ_u denotes the density of the fresh mixture, $A = \pi D^2/4$ is the surface area of the burner nozzle outlet, Δq represents the heat value per unit mass of mixture and \bar{v}_u is the flow velocity determined from the massflow controller indications. Results for stoichiometric flames are plotted in Fig. 7.3. The coefficient k_{CCD} and k_{PM} appearing in

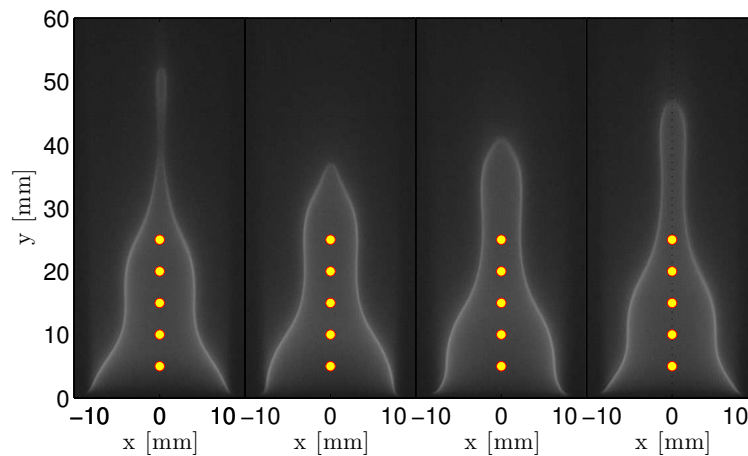


Figure 7.4 : 4 Snapshots of a conical flame modulated at a frequency $f = 100.05$ Hz. Flame-2-3. Tube-1. The five yellow disks in these images correspond to measurement locations.

Eq. (7.3) can then be determined and used to obtain quantitative estimates of heat release rate from the PM and CCD camera signals.

Laser Interferometry Vibrometer (LIV) is used to detect line-of-sight integrated density perturbations in these flames. Measurements are carried out at five different heights above the burner outlet from $y = 5$ mm to 25 mm separated by 5 mm increments along the burner axis. These locations are indicated in Fig. 7.4 by 5 spots.

The signals from the LIV and PM are sampled at a frequency of 8192 Hz during 10 seconds. Flame images recorded with the CCD camera are done in separate experiments. The PM signal is then used as a reference to synchronize the signals from the LIV and CCD camera. The output signal from LIV is converted to line-of-sight integrated density fluctuations using Eq. (5.8). This signal contains noise at low frequency. A high-pass zero-phase shift filter with a cut-off frequency equal to $f/2$, where f is the modulation frequency, is then used to filter the data.

Line-of-sight integrated heat release rate perturbations $\langle \dot{q}' \rangle_L$ estimated from the CCD images can be calculated using:

$$\langle \dot{q}' \rangle_L = \frac{k_{\text{CCD}} I'_d}{A_d} \quad (7.4)$$

where, I'_d is the intensity fluctuation of the signal integrated over the pixels located within a selected zone characterized by a surface area A_d . For the 5

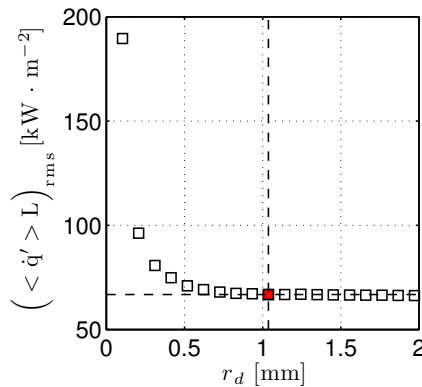


Figure 7.5 : Plot of the r.m.s value of the line-of-sight integrated heat release rate signal $(\langle \dot{q}' \rangle_L)_{\text{rms}}$ versus the diameter of the yellow disk presented in Fig. 7.4. The red marker indicates the diameter used in this work. Flame-2-1 modulated at 100.05 Hz with a modulation level $v_{u,\text{rms}}/\bar{v}_u = 0.07$.

spots presented in Fig. 7.4, a matrix of $n \times n$ square pixels located around the measurement position are used to represent the surface of the laser beam from LIV crossing the flame. The modulus and phase of $\langle \dot{q}' \rangle_L$ obtained with this method depend on the diameter of the spot r_d (or the dimension n of the matrix). Tests are done on Flame-2-1 at $f = 100.05$ Hz with different modulation levels. It is found that variation of the phase induced by the value of n lies within $\pm\pi/10$. But the modulus largely depends on n as shown in Fig. 7.5. A number $n = 21$ is here used to take into account the finite width of the laser beam which has a diameter of 2 mm.

7.3 Results and discussion

Heat release rate perturbations determined from the PM and CCD signals are cross-correlated to find the phase difference between these measurements and synchronize all the diagnostics. One example is shown in Fig. 7.6 for Flame-2-1 within Tube-1 modulated at $f = 100.05$ Hz with a moderate perturbation level $v_{u,rms}/\bar{v}_u=0.07$. The corresponding line-of-sight integrated signal $\langle \dot{q}' \rangle_L$ determined with the CCD images together with the line-of-sight integrated density fluctuations $\langle \rho' \rangle_L$ are plotted in Fig. 7.7. Both signals feature a periodic motion, but it is more interesting to compare the time evolution of the rate of change of $\langle \rho' \rangle_L$ and the signal $\langle \dot{q}' \rangle_L$ represented in Fig. 7.8. Signals are rescaled in these figures to obtain comparable oscillations levels. The two results always match well except for measurements near the vertical position $y = 5$ mm, where a small phase difference appears. In the vicinity of the burner outlet the flame is not perfectly confined. A fresh stream of air between the burned gases and the quartz tube may cause the slight deviation observed.

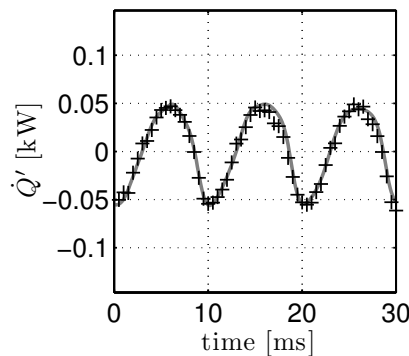


Figure 7.6 : Time history comparison between heat release rate perturbations \dot{Q}' determined with the PM (continuous line) and with the CCD camera (markers). Flame-2-1. Tube-1. Modulation: $f = 100.05$ Hz, $v_{u,rms}/\bar{v}_u = 0.07$.

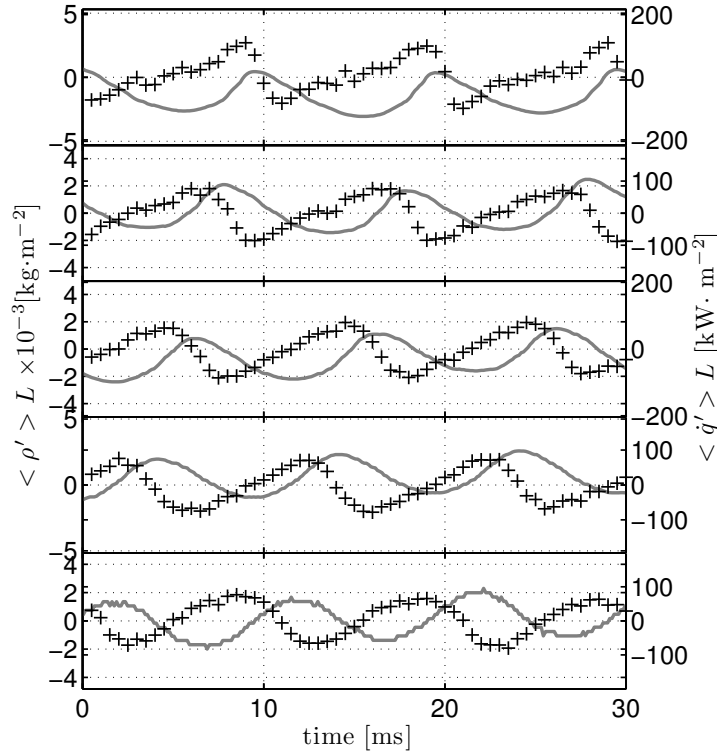


Figure 7.7 : Time history comparison between line-of-sight integrated density perturbations $\langle \rho' \rangle L$ (continuous line) and line-of-sight integrated heat release rate $\langle \dot{q}' \rangle L$ (markers +) estimated from CCD images. The five measurements are obtained at the locations indicated in Fig. 7.4.

Increasing the modulation amplitude, the shapes of the four signals \dot{Q}' , $\langle \dot{q}' \rangle L$, $\langle \rho' \rangle L$ and $d(\langle \rho' \rangle L)/dt$ feature larger differences with pure harmonic responses. A spectral analysis not presented here shows that the main oscillation peak is still clearly associated with the modulation frequency for all cases investigated. A good correlation between the signals $\langle \dot{q}' \rangle L$ and $d(\langle \rho' \rangle L)/dt$ can still be noted for a higher forcing amplitude $v_{urms}/\bar{v}_u=0.14$ in Fig. 7.9. Fig. 7.10 shows however that the correlation between the two signals at higher positions slightly deteriorates near the flame tip when the modulation level reaches 0.21. This may again be caused by the intermittent presence of unburned and burned gases at this location during the modulation cycle which is not well captured in the images. Comparisons of the integrated heat release rate perturbations $\langle \dot{q}' \rangle L$ calculated with different spot diameters r_d also show non-negligible phase differences. The estimation made for $\langle \dot{q}' \rangle L$ with a spot of radius $r_d = 1$ mm may not indicate the correct value in this region

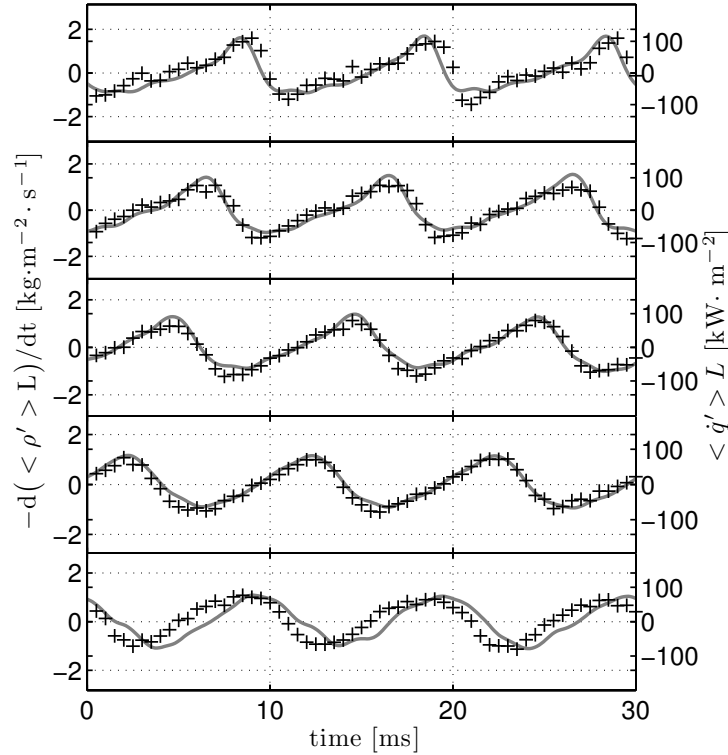


Figure 7.8 : Time history comparison between rate of change of line-of-sight integrated density perturbations $-d(\langle \rho' \rangle L)/dt$ and line-of-sight integrated heat release rate disturbances $\langle \dot{q}' \rangle L$ (markers) estimated from CCD images. The five conditions correspond to those shown in Fig. 7.7.

with intermediate heat release rate signal. This may also be another reason explaining this deterioration.

Changing the modulation frequency alters the shape of the two signals $\langle \dot{q}' \rangle L$ and $d(\langle \rho' \rangle L)/dt$. However, there is still a good agreement between the two signals for frequencies varying from 20.05 Hz to 300.05 Hz and small modulation levels as shown by the results plotted in Fig. 7.11 at two frequencies $f = 150.05$ Hz and 200.05 Hz.

Figures 7.8 to 7.10 show that the amplitudes of the signals $\langle \dot{q}' \rangle L$ and $d(\langle \rho' \rangle L)/dt$ increase with the modulation level. The link between these signals $\langle \dot{q}' \rangle L$ and $d(\langle \rho' \rangle L)/dt$ can be examined by plotting the r.m.s values of the two signals for the different measurement locations and different modulation amplitudes investigated. Results presented in Fig. 7.12(a) for the modulation frequency $f = 100.05$ Hz clearly demonstrates the linear link be-

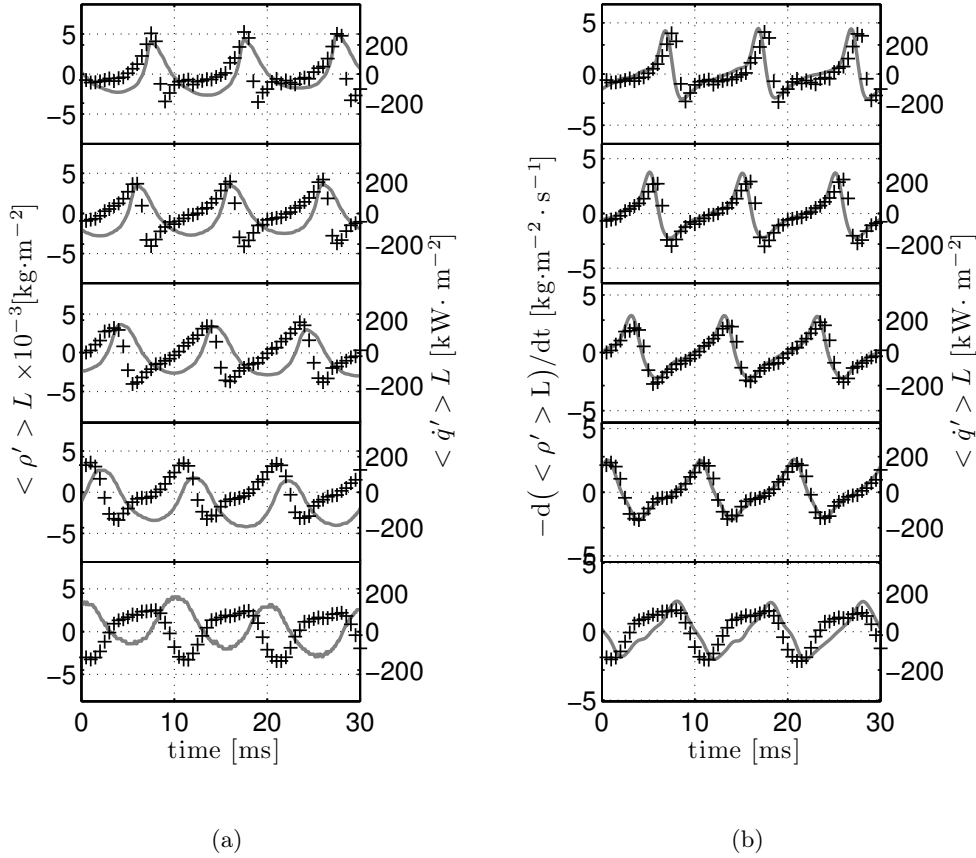


Figure 7.9 : Results deduced from LIV and CCD images measured at five vertical positions, from bottom to top: $y=5$ mm to 25 mm by steps of 5 mm. Flame-2-1. Tube-1. Modulation: $f = 100.05$ Hz, $v_{u,rms}/\bar{v}_u = 0.14$. (a) Comparison between $\langle \rho' \rangle L$ (continuous line) versus $\langle \dot{q}' \rangle L$ (markers +). (b) Comparison between $-\text{d}(\langle \rho' \rangle L) / \text{dt}$ (continuous line) and $\langle \dot{q}' \rangle L$ (markers +).

tween these two signals. Data collapse on a single line which is not function of the measurement position within the flame. The same result is found for a forcing frequency at $f = 150.05$ Hz in Fig. 7.12(b). By plotting all results measured at the vertical position $y = 15$ mm for the different modulation frequencies explored from 20.05 Hz to 200.05 Hz as a function of the modulation level $v_{u,rms}/\bar{v}_u$ in Fig. 7.13, one finds that all data collapse on the same line except for $f = 50.05$ Hz. It was shown in Chapter 5 that in this case the LIV signal features a poor SNR ratio.

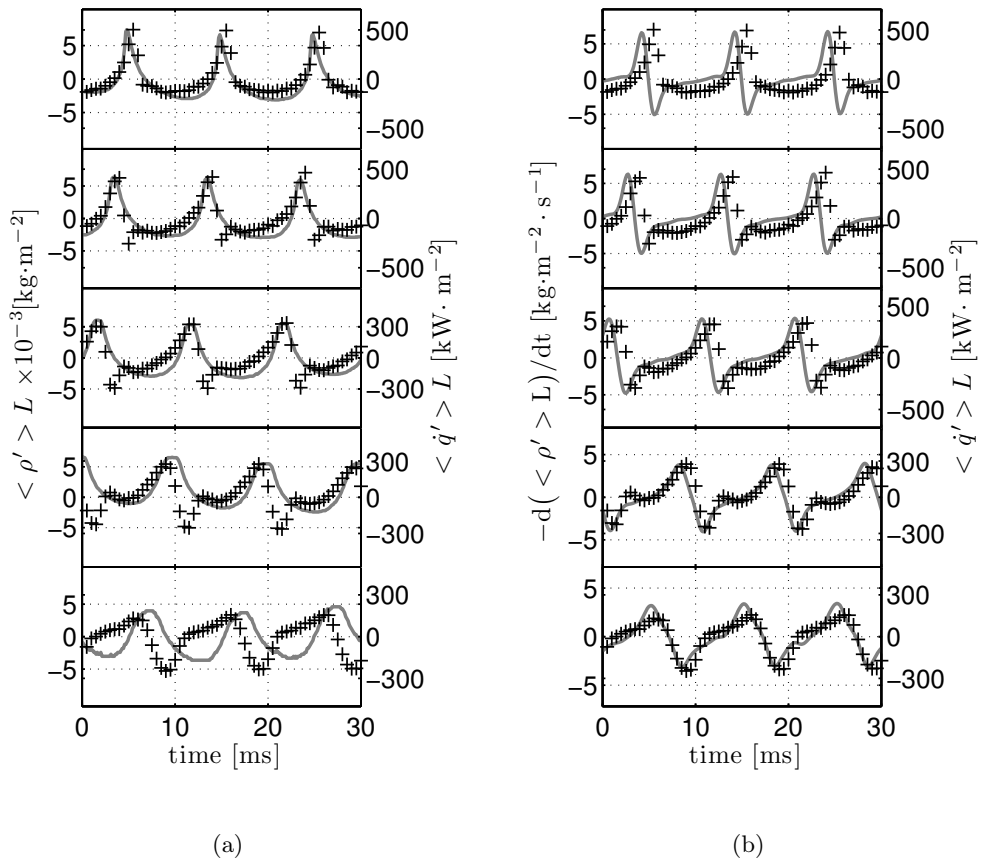


Figure 7.10 : Results deduced from LIV and CCD images measured at five vertical positions, from bottom to top: $y=5$ mm to 25 mm by steps of 5 mm. Flame-2-1. Tube-1. Modulation: $f = 100.05$ Hz, $v_{u,rms}/\bar{v}_u = 0.21$. (a) Comparison between $\langle \rho' \rangle L$ (continuous line) versus $\langle \dot{q}' \rangle L$ (markers +). (b) Comparison between $-d(\langle \rho' \rangle L)/dt$ (continuous line) and $\langle \dot{q}' \rangle L$ (markers +).

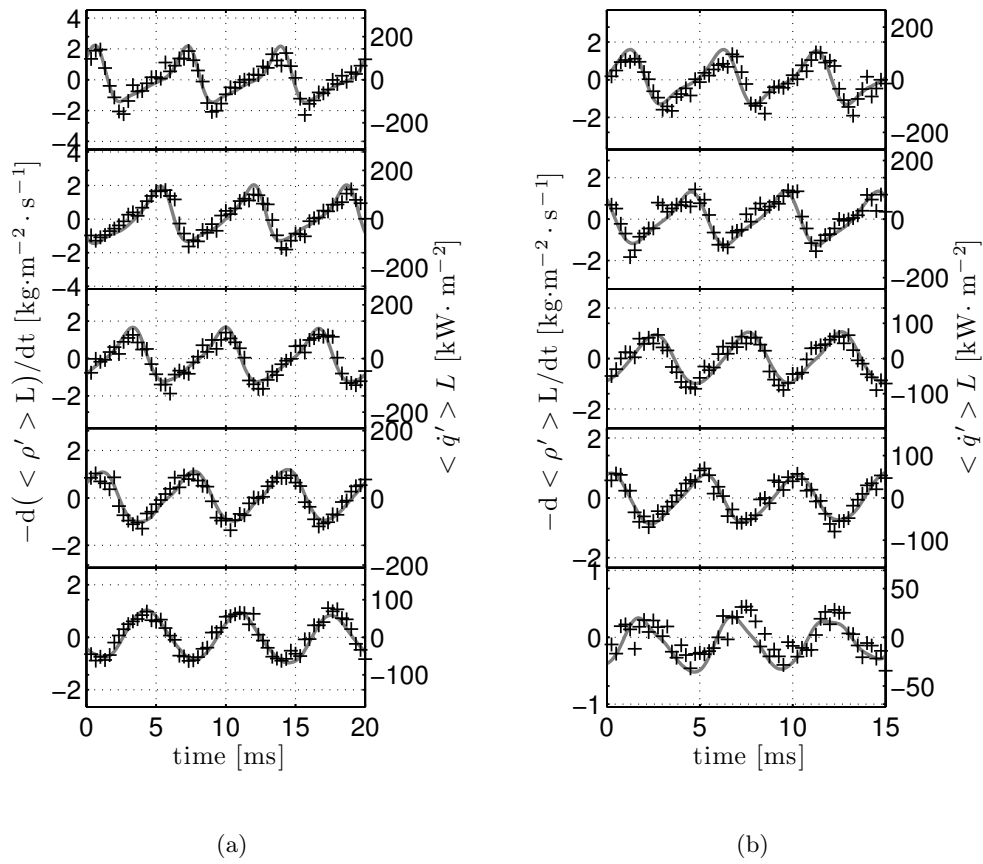


Figure 7.11 : Comparison between $-d(\langle \rho' \rangle L) / dt$ (continuous line) and $\langle \dot{q}' \rangle L$ (markers +) at five vertical positions, from bottom to top: $y=5$ to 25 mm by steps of 5 mm. Flame-1. Tube-1. (a) Modulation: $f = 150.05$ Hz, $v_{u,rms}/\bar{v}_u = 0.07$. (b) Modulation: $f = 200.05$ Hz, $v_{u,rms}/\bar{v}_u = 0.07$.

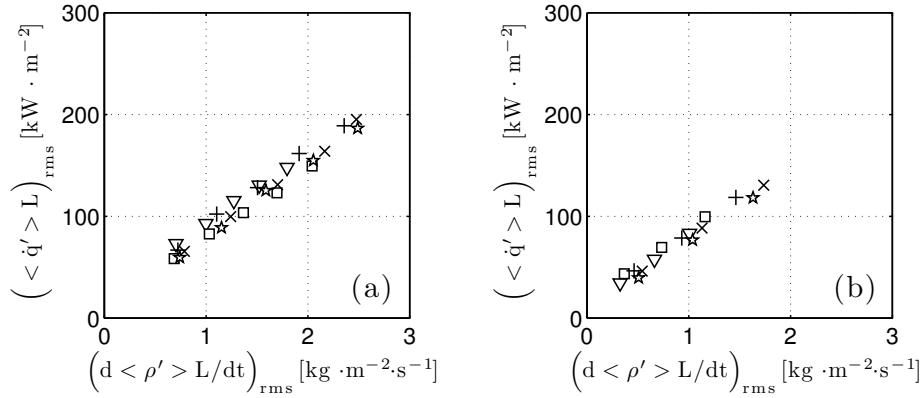


Figure 7.12 : Plot of the r.m.s value of $\langle \dot{q}' \rangle L$ as a function of $d \langle \rho' \rangle L / dt$. Markers ∇ , \square , $+$, \star and \times are used to indicate results measured from $y = 5$ to 25 mm by steps of 5 mm. Flame-2-1. Tube-1. (a) $f = 100.05$ Hz, $v_{u,rms}/\bar{v}_u$ varies from 0.07 to 0.21. (b) $f = 150.05$ Hz, $v_{u,rms}/\bar{v}_u$ varies from 0.04 to 0.11.

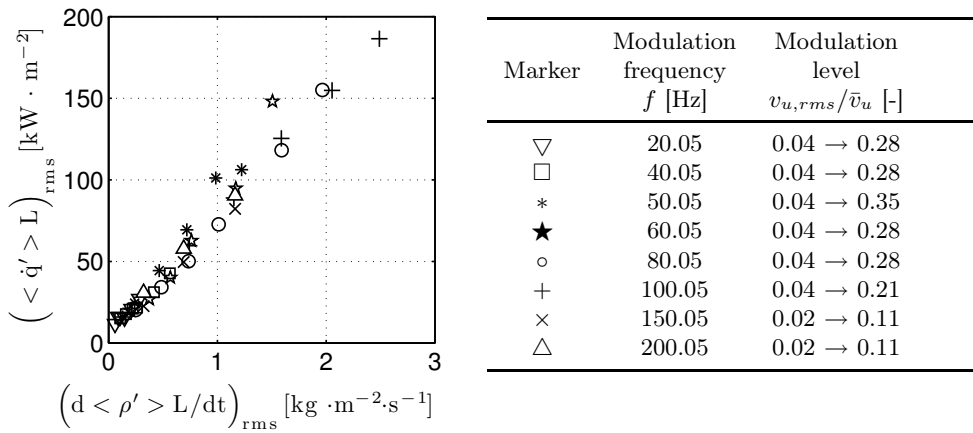


Figure 7.13 : Plot of the r.m.s value of $\langle \dot{q}' \rangle L$ as a function of $d \langle \rho' \rangle L / dt$. All measurements correspond to the vertical position $y = 15$ mm. Flame-2-1. Tube-1. The modulation frequency f varies from 20.05 Hz to 200.05 Hz.

It is now worth examining flames with different flow operating conditions confined by the same small tube (Tube-1). This is done for:

- (i) Flames featuring the same equivalence ratio but different flame heights. This comprises Flame-1, Flame-2-1 and Flame-3.
- (ii) Flames featuring the same height but different equivalence ratios. This includes Flame-2-1, Flame-2-2 and Flame-2-3.

The same experiments are conducted for different modulation frequencies and forcing levels. Results for these configurations are similar to those obtained for

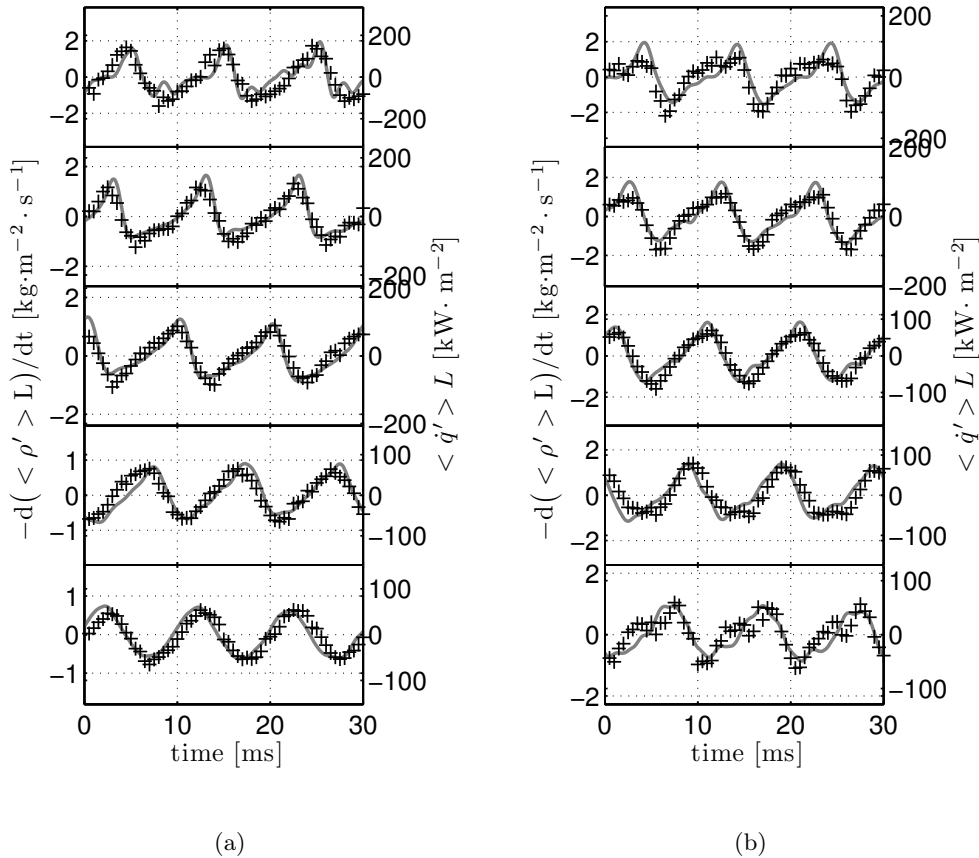


Figure 7.14 : Comparison between $-d(\langle \rho' \rangle L)/dt$ (continuous line) and $\langle \dot{q}' \rangle L$ (markers +) at five vertical positions, from bottom to top: $y=5$ to 25 mm by steps of 5 mm. Flame-1. Tube-1. (a) Flame-1. Tube-1. Modulation: $f = 100.05$ Hz, $v_{u,rms}/\bar{v}_u = 0.07$. (b) Flame-3. Tube-1. Modulation: $f = 100.05$ Hz, $v_{u,rms}/\bar{v}_u = 0.07$.

Flame-2-1 as shown in Figs. 7.14 and 7.15. Plots of the r.m.s values of $\langle \dot{q}' \rangle L$ and $d(\langle \rho' \rangle L)/dt$ are presented in Figs. 7.16(a) and 7.16(b) for these flames. All results collapse again on the same line for these flames featuring different heights and equivalence ratios.

Measurements are finally conducted with Flame-2-1 confined by different quartz tube diameters Tube-2 and Tube-3. For the intermediate diameter Tube-2, the correlation between the two signals $\langle \dot{q}' \rangle L$ and $d(\langle \rho' \rangle L)/dt$ deteriorates as shown by Fig. 7.17(a) except near the middle height of the flame where the burned gases are in contact with the quartz tube. For the flame confined by

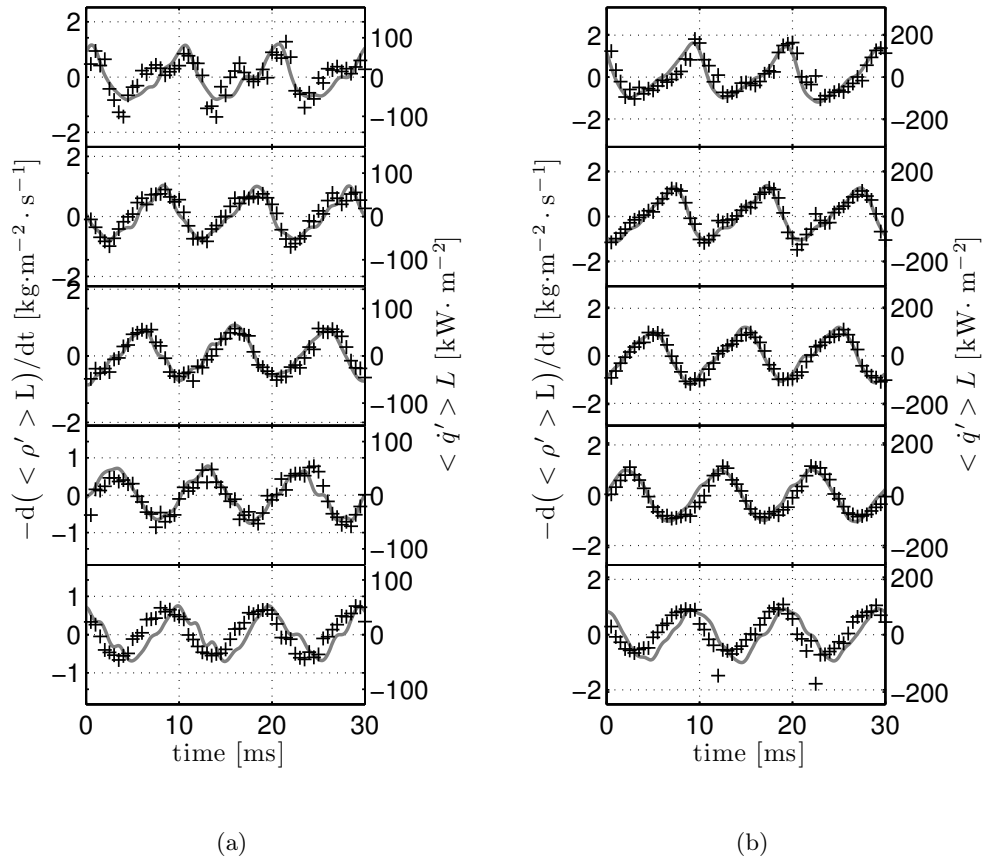


Figure 7.15 : Comparison between $-d(\langle \rho' \rangle L)/dt$ (continuous line) and $\langle \dot{q}' \rangle L$ (markers +) at five vertical positions, from bottom to top: $y=5$ to 25 mm by steps of 5 mm. Flame-1. Tube-1. (a) Flame-2-2. Tube-1. Modulation: $f = 100.05$ Hz, $v_{u,rms}/\bar{v}_u = 0.07$. (b) Flame-2-3. Tube-1. Modulation: $f = 100.05$ Hz, $v_{u,rms}/\bar{v}_u = 0.07$.

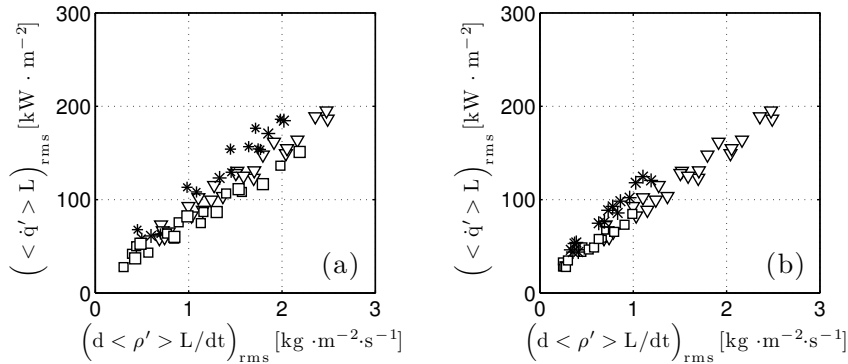


Figure 7.16 : Plot of the r.m.s value of $\langle \dot{q}' \rangle L$ as a function of $d \langle \rho' \rangle L / dt$. The modulation frequency is kept constant 100.05 Hz.

Graph	Investigation	Marker	Flame	Modulation level $v_{u,rms}/\bar{v}_u$ [-]
(a)	Flame height	*	Flame-1	0.07 \rightarrow 0.28
		∇	Flame-2-1	0.07 \rightarrow 0.21
		\square	Flame-3	0.04 \rightarrow 0.11
(b)	Equivalence ratio	∇	Flame-2-1	0.07 \rightarrow 0.21
		\square	Flame-2-2	0.04 \rightarrow 0.11
		*	Flame-2-3	0.04 \rightarrow 0.11

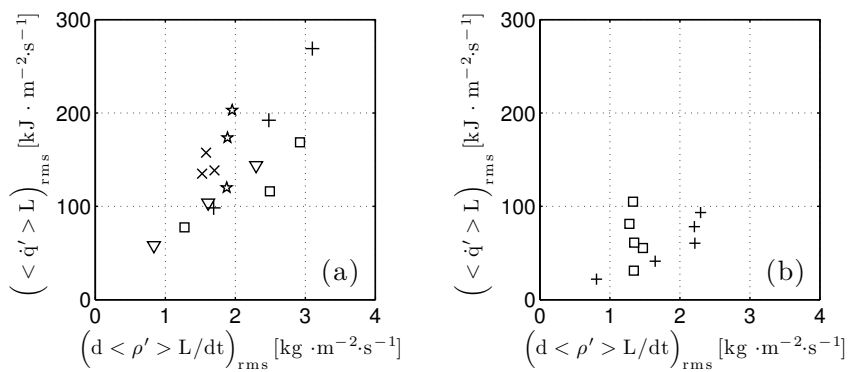


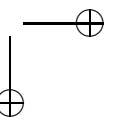
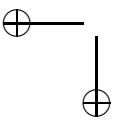
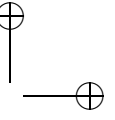
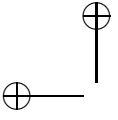
Figure 7.17 : Plot of the r.m.s value of $\langle \dot{q}' \rangle L$ as a function of $d \langle \rho' \rangle L / dt$. Markers ∇ , \square , $+$, \star and \times are used to indicate results measured from $y = 5$ to 25 mm by steps of 5 mm. Flame-2-1. The modulation frequency is kept constant 100.05 Hz. (a) Results with Tube-2. (b) Results with Tube-3.

the largest tube diameter Tube-3, the quartz lies always far from the burned gases and results are always distorted as shown in Fig. 7.17(b).

7.4 Conclusion

The work presented in this chapter provided a possibility to estimate heat release rate disturbances by measuring density fluctuations in laminar premixed flames submitted to flowrate modulations. This led to line-of-sight integrated measurements of density fluctuations along the optical path passing through the flame determined with a Laser Interferometric Vibrometer. Experimental validations were carried out on a generic configuration with laminar premixed conical flames submitted to harmonic flow modulations. Estimates of heat release rate fluctuations deduced from LIV were compared with data obtained from the chemiluminescence emission of the flame. A good correlation was found between the two techniques at different forcing frequencies and modulation amplitudes for the different flames envisaged in this work. A proportional relation between the two signals was found that does not depend on the measurement position and modulation frequency, but it features a slight dependence on the flow operating conditions mainly due to the poor performance of the technique based on chemiluminescence emission for rich flames.

It was demonstrated in previous chapters that LIV enables to detect density perturbations in non reacting and reacting flows. Based on a displacement system and a tomography reconstruction, spatial resolved data can be obtained with LIV for axisymmetric and harmonically modulated flows. When density perturbations in the fresh mixture and burned gases were neglected, LIV was successfully used to reconstruct the flame front motion of the laminar premixed conical flames submitted to flowrate modulations. Compared to the acoustic method developed, the technique based on LIV enables to yield time resolved data at a very high repetition rate. Quantitative measurement can be achieved for the confined flames. Moreover, this technique was successfully validated for lean, stoichiometric and rich flames. It is in principle not limited to perfectly premixed combustion modes. Future work are directly targeted to partially premixed and diffusion flames.



Conclusion

The work presented in this document focused on the development of two diagnostics for the determination of heat release rate disturbances in unsteady flames.

The first technique presented is based on the determination of the travel time of ultrasonic waves crossing through unsteady flames. Disturbances in the sound travel time were linked to perturbations of the width of the burned gases crossed by ultrasonic waves. This information was used to reconstruct internal and externally induced heat release rate perturbations in laminar conical flames. Validations of this technique were carried out in two configurations.

The acoustic method was first used to detect small heat release rate disturbances resulting from a buoyancy flow instability of the flame plume in laminar premixed conical flames fed by a steady flow. An analytical relation was derived linking sound travel time and heat release rate disturbances using the fact that low frequency fluctuations of the burned gases volume are in this case proportional to a characteristic length of the burned gases width determined with this technique. An experimental validation of the proposed technique was conducted on a generic configuration with a tweeter to produce the ultrasonic waves and two microphones to record the incident and transmitted signals through the hot plume of different laminar premixed conical flames. Time resolved measurements obtained with this acoustic method were compared with data obtained from records of the chemiluminescence emission of the flames. A good agreement was obtained for the different cases explored demonstrating that the transmission of ultrasonic waves can effectively be used to estimate very small heat release rate disturbances.

This analysis was then extended to determine heat release rate in laminar conical flames submitted to external flow perturbations. An expression for the transfer function between heat release rate and sound travel time disturbances was derived. This relation depends on the flow operating conditions, flame shape and modulation frequency. Comparisons between predictions and measurements were then conducted for harmonic flow disturbances. The linearity of

the response of sound travel time fluctuations induced by heat release rate disturbances was demonstrated experimentally when the flame was modulated at different forcing frequencies and when the perturbation level was not too large. At higher modulation levels deviations from linearity were found. Predictions of the transfer function also showed a good agreement with experimental data for lean and stoichiometric premixed flames. For fuel rich operating conditions, results are more scattered.

This new method provides an alternative to estimate heat release rate perturbations when the optical access to the combustion zone is limited. It can be used to detect time resolved heat release rate fluctuations based on a relatively inexpensive material. The pulse compression technique used to generate the ultrasonic trains of chirp signals enables to detect tiny fluctuations of the sound travel time with a relatively high signal to noise ratio. This type of detection technique is in principle not restricted to unconfined flames, since it is possible to eliminate effects of multiple reflections with chirps that are identified individually, although this problem was not examined in the present work. Another possible advantage of the proposed ultrasonic technique is that it is not influenced by the mean pressure and it can be applied in non optically thin reacting flows. Absorption of the chemiluminescence or fluorescence signals is one limitation for the use of optical techniques at high pressure since these signals may be strongly altered along the optical path.

Several issues remain however to be addressed. This acoustic method was validated yet for lean and stoichiometric laminar premixed pulsated flames when the shape of the flame is known. Future work should focus on determination of heat release rate disturbances without a priori knowledge of the flame shape. This important limitation can be circumvented by different strategies that will be the object of future developments. The next objective is to develop a technique enabling quantitative estimates of heat release rate fluctuations for other flame geometries. Effects of turbulence must also be envisaged because they are responsible of scattering, attenuation and frequency shift in the transmitted signal. These problems can probably be minimized by an appropriate choice of the operating signal frequency bandwidth and an optimization of the pulse compression technique. The material for sound generation and measurement should also be improved. The ultrasonic actuator and detector efficiencies should be improved to produce high frequency sound waves with amplitudes larger than the turbulent background pressure fluctuation level. These devices should also withstand high temperatures for use in confined configurations. Solutions to examine heat release rate perturbations in non perfectly premixed and diffusion flames must be sought. This last difficulty is challenging since there is no time resolved measurement technique available yet with a simple link between the

signal output and heat release rate. One possible candidate was explored in the present work.

The second technique developed uses a Laser Interferometric Vibrometer (LIV). This diagnostic enables to determine line-of-sight integrated optical path disturbances and is widely used in industry to measure surface vibrations up to very high frequencies. In a setup with a fixed geometrical path, this enables to determine line-of-sight integrated perturbations of refractive index integrated along the optical path of a laser beam crossing a non uniform flow. This technique was used in this work to detect line-of-sight integrated density fluctuations along a laser beam crossing a flame and which is reflected by an external mirror. It was shown that density perturbations within the flow are mainly linked to heat release rate disturbances for confined laminar flames. In unconfined flames, the interface between the hot plume of burned gases and fresh ambient air generate additional density disturbances that must be taken into account in the interpretation of the signal measured by LIV. For confined flames where the burned gases are in contact with the combustion chamber wall, density disturbances are mainly caused by heat release rate perturbations and the signal is easier to interpret. This property was first used to estimate the motion of flame front wrinkles in laminar premixed conical flames submitted to flow modulations when density perturbations in the burned gases and the fresh mixture can be neglected. An experimental validation was carried out on pulsated laminar premixed confined flames at different working conditions. The flame front oscillations determined with LIV were compared to measurements obtained with flame snapshots taken during the modulation cycle. Excellent correlations were found between the results from the two diagnostics in all investigated cases. The signal determined by LIV is proportional to the flame width in agreement with theoretical predictions. Measurements also confirm that this link does not depend on the diameter of flame confinement tube, flame height, equivalence ratio, modulation frequency and modulation level.

It was then shown that it is also possible to measure heat release rate disturbances when the flame is confined. The flame is in this case stabilized at the interfaces between fresh reactants and hot combustion products as in many practical combustion systems. This led to line-of-sight integrated measurements of heat release rate disturbances along the optical path. These experimental validations were carried out with premixed conical flames confined by a quartz tube and submitted to harmonic flow modulations. Estimates of heat release rate fluctuations deduced from LIV were compared with data obtained from the chemiluminescence emission of the flame. A good agreement was found between measurements obtained with the two techniques at different forcing frequencies and small to moderate perturbation amplitudes. A proportional

relation between the two signals was found that does not depend on the measurement position and modulation frequency, but it is slightly dependent on flame operating conditions. Results for fuel rich flames feature slight deviations between measurements. One possible origin of the differences observed may be attributed to the difficulty to interpret the chemiluminescence emission signal for rich flames. This problem has to be further investigated in future work.

The main advantages of this optical technique are that it is relatively simple to implement and it yields quantitative time resolved data which are in principle not limited to perfectly premixed combustion modes. The link between density and heat release rate perturbations was established without any assumption on the type of combustion mode, although it was only validated yet for unsteady laminar premixed flames. Validations for partially premixed and diffusion flames are more difficult to handle since there is no reference technique to easily determined heat release rate fluctuations in these combustion modes. As chemiluminescence emission, this technique only yields a line-of-sight integrated information. It is however possible to obtain time resolved local data by using two laser beams crossing at different angles (Giuliani et al. 2010b; Köberl et al. 2010), although this technique was not tested yet to measure heat release rate perturbations. It was also shown that the performance of the LIV system used in this work drops at very low frequencies. This problem can be circumvented by adding a Bragg cell in the path of the object beam from LIV. This solution enables to easily eliminate low frequency background noise if measurements at these frequencies are requested. Future work will focus on partially premixed, non premixed and turbulent flames. Time resolved data can easily be handled with this type of technique due to the very high operating frequency bandwidth of LIV. One difficulty is the large deflection of the laser beam near the flame front due to the large density gradients in this region causing a deflection of the optical beam. This deflection may be a problem for turbulent flames in regions where the flame front is strongly distorted by turbulence. This may cause a too large deviation of the optical laser beam that does not reach the sensor head. The material and experimental setup can also be improved by different means. Spatial resolution can be improved by reducing the diameter of the laser beam with different optics or by modifying its operating wavelength. Selection of the laser wavelength and laser power may also be adapted if certain chemical species may alter the signal due to absorption.

Appendix A

Examination of effects of ultrasonic waves on flames

High frequency acoustic waves barely interact with flames. This is validated in this appendix. Experiments are conducted on a stoichiometric laminar premixed conical flame in the absence and presence of harmonic flow modulation. The response of the flame to high frequency acoustic waves produced by an ultrasonic emitter located at one side of the flame is investigated. The analysis is conducted in the frequency domain where the light intensity from the flame is measured with a photodiode.

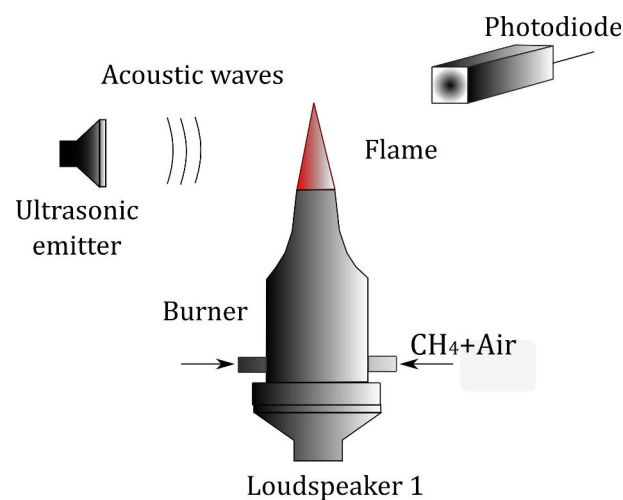


Figure A.1 : *Schematic of the experimental setup.*

A.1 Experimental configuration

The experimental configuration is presented in Fig. A.1. Tests are carried out on a laminar premixed conical flame stabilized on the axisymmetric burner presented in Chapter 1. The ultrasonic emitter is placed at one side of the flame with a distance around 10 cm. Harmonic waveforms at different frequencies varying from 10 to 50 kHz with steps of 10 kHz are used to drive the ultrasonic emitter. The sound level is kept constant for all frequencies explored with a peak-to-peak amplitude equal to 10 Pa at the emitter location. A photomultiplier (PM) is placed next to the flame to record the light intensity from the flame. The response of the flame is then examined based on the power spectra of the signals from the PM. The flow velocity of the methane-air mixture is fixed to $\bar{v}_u = 1.5 \text{ m}\cdot\text{s}^{-1}$ and equivalence ratio is set to $\phi = 1.00$. Two cases are investigated: (a) a laminar premixed conical unconfined flame featuring a “flickering” phenomenon driven by buoyancy forces and (b) a laminar premixed conical flame partially confined by a quartz tube and submitted to flow velocity modulation.

A.2 Results and discussion

In these experiments, the light intensity signals are sampled using following settings:

- (i) High frequency resolution is necessary for the analysis of the response at very low frequency, typically below 100 Hz. The signals measured by PM are thus sampled at a frequency $f_s = 1024 \text{ Hz}$ over 32 seconds. The resolution is then given by $\Delta f = 0.25 \text{ Hz}$.
- (ii) High sampling rate is necessary for the analysis at high frequency. Records are therefore sampled at a higher frequency $f_s = 2^{20} \text{ Hz}$ over a period of 1 s. The resolution is $\Delta f = 125 \text{ Hz}$.

Results when the flame is unconfined and in the absence of external perturbations are first examined. The flame features a “flickering” motion induced by the buoyancy forces. This motion is characterized by oscillation of the flame tip with a frequency around 16 Hz. The power spectrum presented in Fig. A.2 shows that the flame features also frequency of about 16 Hz which corresponds to the location of the largest peak. Measurements when the ultrasonic emitter is turned on and off do not change indicating that the high frequency acoustic waves impinging on the flame have no effect. Examination of this spectrum over a large frequency bandwidth presented in Fig. A.3 shows that there is no additional effect induced by the acoustic waves at high frequency. The same conclusions can be drawn for the response of a partially confined flame with a

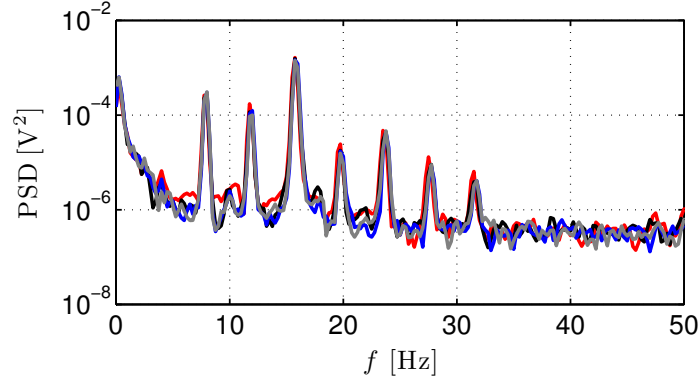


Figure A.2 : Power spectral density of the PM signal examined at low frequency for the unconfined flame. The flame pulsates at a frequency around 16 Hz which is indicated by the largest peak in the figure. The red line denotes results when the ultrasonic emitter is turned off. Measurements are also presented when the emitter is turned on. The driving frequencies f_d of the emitter are: 20 kHz (black line), 30 kHz (blue line) and 40 kHz (gray line).

quartz tube placed on the top of the flame when the flame is modulated by a harmonic excitation at 100 Hz. Results presented in Figs. A.4 and A.5 are not modified when the ultrasonic emitter is turned on.

A ratio is used to represent the difference between the peak value in the spectrum at the buoyancy frequency (or at the modulation frequency) when the emitter is turned off ($PSD_0(f)$) and when the emitter is switched on ($PSD(f)$). It is defined by:

$$\Lambda(f) = \frac{|PSD(f) - PSD_0(f)|}{PSD_0(f)} \quad (A.1)$$

where the frequency f in this expression is replaced by the “flickering” frequency f_b for the unconfined flame or the modulation frequency f_m for the partially confined flame. The results are shown in Fig. A.6 for different driving frequencies f_d of the ultrasonic emitter. One finds $\Lambda(f_b) < 0.15$ in Fig. A.6(a) and $\Lambda(f_m) < 0.05$ in Fig. A.6(b) showing that the high frequency acoustic waves generated by the ultrasonic transducer do not disturb the low frequency response of the flame to internal flow instabilities or externally imposed flow modulations.

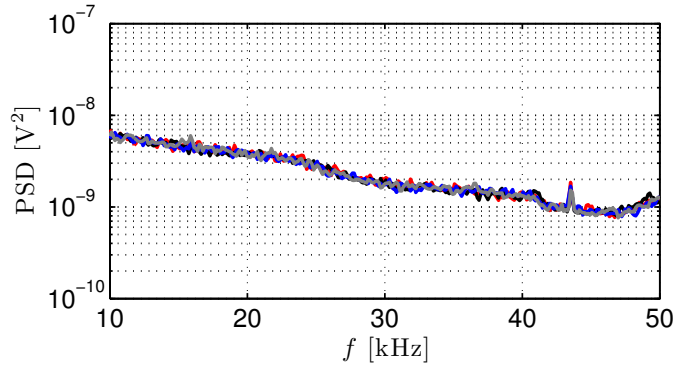


Figure A.3 : Power spectral density of the PM signal examined between 10 to 50 kHz. Operating and forcing conditions are the same as those indicated in Fig. A.2.

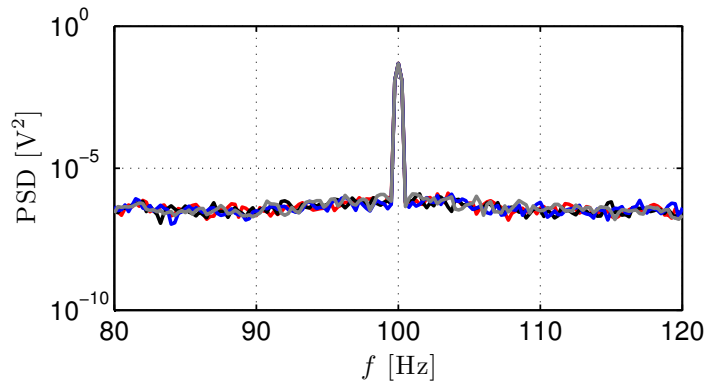


Figure A.4 : Power spectral density of the PM signal examined at low frequency for the partially confined flame modified at 100 Hz and an amplitude $v_{u,rms}/\bar{v}_u = 0.21$. The red line denotes results when the ultrasonic emitter is turned off. Measurements are also presented when the emitter is turned on. The driving frequencies f_d of the emitter are: 20 kHz (black line), 30 kHz (blue line) and 40 kHz (gray line).

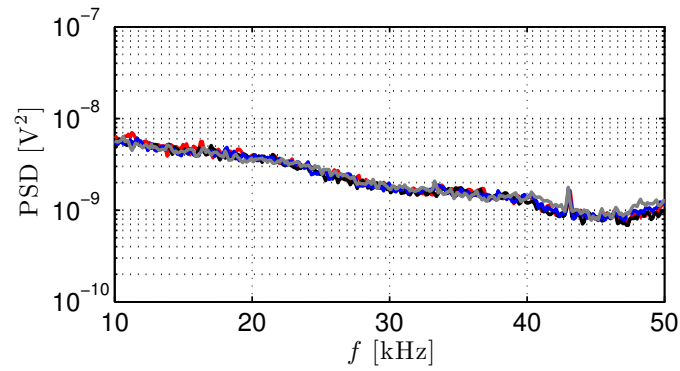


Figure A.5 : Power spectral density of the PM signal examined between 10 to 50 kHz. Operating and forcing conditions are the same as those indicated in Fig. A.4.

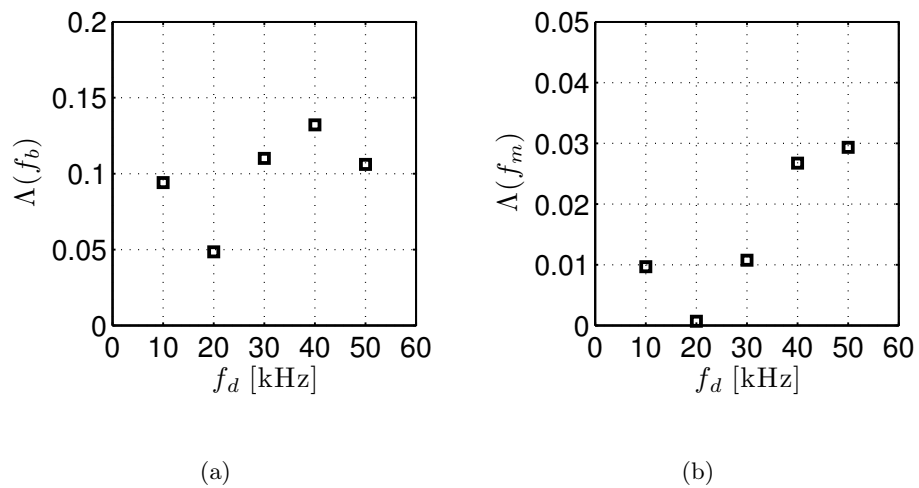


Figure A.6 : Plot of $\Lambda(f_b)$ (left figure) and $\Lambda(f_m)$ (right figure) as a function of driving frequency f_d of the ultrasonic waves.

A.3 Conclusion

High frequency waves barely disturb the low frequency response of laminar conical flames perturbed by internal flow instabilities or externally imposed flow modulations. The response of these flames impinged by ultrasonic waves produced by an emitter placed close to the flame has been investigated using an analysis of the power spectrum of the light intensity signal recorded by a photomultiplier. It has been validated that high frequency waves between [10 50] kHz have no effect on the flame dynamics envisaged in this work.

References

- Ahmadi, M., M. S. Avval, T. Yousefi, M. Goharkhah, B. Nasr, and M. Ashjaee (2011). Temperature measurement of a premixed radially symmetric methane flame jet using the Mach-Zehnder Interferometry. *Opt. Lasers Eng.* 49(7), 859–865.
- Akay, M. (Ed.) (1997). *Time Frequency and Wavelets in Biomedical Signal Processing*. Wiley-IEEE Press, New York.
- Andreeva, T. and W. Durgin (2004). Experimental investigation of ultrasound propagation in turbulent, diffractive media. *J. Acoust. Soc. Am.* 115(4), 1532–1536.
- Andreeva, T. and W. Durgin (2011). Determination of correlation functions of turbulent velocity and sound speed fluctuations by means of ultrasonic technique. *Exp. Fluids* 51(6), 1765–1771.
- Ayoola, B., R. Balachandran, J. Frank, E. Mastorakos, and C. Kaminski (2006). Spatially resolved heat release rate measurements in turbulent premixed flames. *Combust. Flame* 144(1-2), 1–16.
- Baerg, W. and W. Schwarz (1966). Measurements of the scattering of sound from turbulence. *J. Acoust. Soc. Am.* 39(6), 1125–1132.
- Baillot, F., A. Bourehla, and D. Durox (1996). The characteristics method and cusped flame fronts. *Combust. Sci. and Tech.* 112(1), 327–350.
- Baillot, F., D. Durox, S. Ducruix, G. Searby, and L. Boyer (1999). Parametric response of a conical flame to acoustic waves. *Combust. Sci. and Tech.* 142(1-6), 91–109.
- Baillot, F., D. Durox, and R. Prud’homme (1992). Experimental and theoretical study of a premixed vibrating flame. *Combust. Flame* 88(2), 149–168.
- Balachandran, R., B. Ayoola, C. Kaminski, A. Dowling, and E. Mastorakos (2005a). Experimental investigation of the nonlinear response of turbulent premixed flames to imposed inlet velocity oscillations. *Combust. Flame* 143(1-2), 37–55.
- Balachandran, R., A. P. Dowling, and E. Mastorakos (2005b, April). Response of turbulent premixed flames subjected to inlet velocity and

- equivalence ratio perturbations. Louvain-la-Neuve. European Combustion Meeting.
- Birbaud, A., D. Durox, and S. Candel (2006). Upstream flow dynamics of a laminar premixed conical flame submitted to acoustic modulations. *Combust. Flame* 146(3), 541–552.
- Blanc-Benon, P., D. Juvé, and G. Comte-Bellot (1991). Occurrence of caustics for high-frequency acoustic waves propagating through turbulent fields. *Theor. Comp. Fluid Dyn.* 2(5-6), 271–278.
- Boashash, B. (Ed.) (2003). *Time frequency signal analysis and processing: a comprehensive reference*. Elsevier Science, London.
- Bourehla, A. and F. Baillet (1998). Appearance and stability of a laminar conical premixed flame subjected to an acoustic perturbation. *Combust. Flame* 114(3-4), 303–318.
- Boxx, I., M. Stöhr, C. Carter, and W. Meier (2009). Sustained multi-kHz flamefront and 3-component velocity-field measurements for the study of turbulent flames. *Appl. Phys. B-Lasers Opt.* 95(1), 23–29.
- Boyce, M. P., Ph.D., and P.E. (2006). *Gas Turbine Engineering Handbook, Third Edition*. Gulf Professional Publishing, Boston.
- Bragg, S. L. (1963). Combustion noise. *J. Inst. Fuel* 36(6), 12–16.
- Brandwood, D. (2003). *Fourier Transforms in Radar and Signal Processing*. Artech House Publishers, London.
- Callender, B., E. Gutmark, and S. Martens (2005). Far-field acoustic investigation into chevron nozzle mechanisms and trends. *AIAA journal* 43(1), 87–95.
- Candel, S. (2002). Combustion dynamics and control: Progress and challenges. *Proc. Combust. Inst.* 29(1), 1–28.
- Candel, S., D. Durox, S. Ducruix, A.-L. Birbaud, N. Noiray, and T. Schuller (2009). Flame dynamics and combustion noise: progress and challenges. *Int. J. Aeroacoustics* 8(1), 1–56.
- Candel, S., D. Durox, and T. Schuller (2004). Flame interactions as a source of noise and combustion instabilities. Number 2004-2928. In AIAA paper.
- Chernov, L. A. (1960). *Wave propagation in a random medium*. McGraw-Hill, New York.
- Cho, J. (2009). Analysis of low-frequency wave scattering by turbulent premixed flame. *J. Fluid Mech.* 634, 137–164.
- Clavin, P. (1985). Dynamic behavior of premixed flame fronts in laminar and turbulent flows. *Prog. Energ. Combust. Sci.* 11(1), 1–59.

REFERENCES

157

- Cohen, L. (1994). *Time Frequency Analysis: Theory and Applications*. Prentice Hall, New Jersey.
- Contreras, H. and F. Lund (1990). Ultrasound as a probe of turbulence. II. Temperature inhomogeneities. *Phys. Lett. A* 149(2-3), 127–130.
- Cook, C. E. and M. Bernfield (1993). *Radar Signals: An Introduction to Theory and Application*. Artech House Publishers, London.
- Crow, S. and F. Champagne (1971). Orderly structure in jet turbulence. *J. Fluid Mech.* 48, 547–591.
- Docquier, N., S. Belhafaoui, F. Lacas, N. Darabiha, and C. Rolon (2000). Experimental and numerical study of chemiluminescence in methane/air high-pressure flames for active control applications. *Proc. Combust. Inst.* 28(2), 1765–1774.
- Donbar, J., J. Driscoll, and C. Carter (2000). Reaction zone structure in turbulent nonpremixed jet flames—from CH-OH PLIF images. *Combust. Flame* 122(1-2), 1–19.
- Dowling, A. P. (1995). The calculation of thermoacoustic oscillations. *J. Sound Vib.* 180(4), 557–581.
- Duchaine, P. (2010). *Experimental analysis of the dynamics of gaseous and two-phase counterflow flames submitted to upstream modulations*. Ph. D. thesis, Ecole Centrale Paris.
- Ducruix, S., D. Durox, and S. Candel (2000). Theoretical and experimental determinations of the transfer function of a laminar premixed flame. *Proc. Combust. Inst.* 28(1), 765–773.
- Ducruix, S., T. Schuller, D. Durox, and S. Candel (2003). Combustion dynamics and instabilities: Elementary coupling and driving mechanisms. *J. Propuls. Power* 19(5), 722–734.
- Durox, D., F. Baillot, P. Scoufflaire, and R. Prud’homme (1990). Some effects of gravity on the behaviour of premixed flames. *Combust. Flame* 82(1), 66–74.
- Durox, D., F. Baillot, G. Searby, and L. Boyer (1997a). On the shape of flames under strong acoustic forcing: a mean flow controlled by an oscillating flow. *J. Fluid Mech.* 350, 295–310.
- Durox, D. and S. Ducruix (2000). Concerning the location of the schlieren limit in premixed flames. *Combust. Flame* 120(4), 595–598.
- Durox, D., S. Ducruix, and F. Baillot (1998). Strong acoustic forcing on conical premixed flames. *Proc. Combust. Inst.* 27(1), 883–889.
- Durox, D., T. Yuan, and E. Villermaux (1997b). The effect of buoyancy on flickering in diffusion flames. *Combust. Sci. and Tech.* 124(1-6), 277–294.

- Elicer-Cortes, J. C., R. Contreras, D. Boyer, M. Pavageau, and R. H. Hernandez (2004). Temperature spectra from a turbulent thermal plume by ultrasound scattering. *Exp. Therm. Fluid Sci.* 28(8), 803–813.
- Elicer-Cortes, J. C., A. Navia, D. Boyer, M. Pavageau, and R. Hernandez (2006). Experimental determination of preferred instability modes in a mechanically excited thermal plume by ultrasound scattering. *Exp. Therm. Fluid Sci.* 30(4), 355–365.
- Fabrikant, A. (1983). Sound scattering by vortex flows. *Sov. Phys. Acoust.* 29, 152–154.
- Fayoux, A., K. Zähringer, O. Gicquel, and J. Rolon (2005). Experimental and numerical determination of heat release in counterflow premixed laminar flames. *Proc. Combust. Inst.* 30(1), 251–257.
- Fleifil, M., A. M. Annaswamy, Z. A. Ghoneim, and A. F. Ghoniem (1996). Response of a laminar premixed flame to flow oscillations: A kinematic model and thermoacoustic instability results. *Combust. Flame* 106(4), 487–510.
- Fouad, E.-D. (2011). Coherent anti-stokes raman scattering: Spectroscopy and microscopy. *Vib. Spectrosc.* 55(1), 1–37.
- Gabriel, D. (Ed.) (2006). *Combustion Processes in Propulsion: Control, Noise and Pulse Detonation*. Elsevier Inc., New York.
- Gardiner, W., Y. Hidaka, and T. Tanzawa (1981). Refractivity of combustion gases. *Combust. Flame* 40(0), 213–219.
- Gaydon, A. G. (1957). *The spectroscopy of flames*. Wiley, New York.
- Giuliani, F., A. Lang, T. Leitgeb, J. Woisetschlager, and F. Heitmeir (2007, April). Using dual laser vibrometry to monitor the stability of gas turbine combustion. Proceedings of European Combustion Meeting 2007.
- Giuliani, F., T. Leitgeb, D. Durox, and T. Schuller (2010a, September). Analyse des variations de densité dans une flamme de référence soumise à une excitation acoustique. Congrès Francophone de Techniques Laser.
- Giuliani, F., T. Leitgeb, A. Lang, and J. Woisetschlager (2010b). Mapping the density fluctuations in a pulsed air-methane flame using laser-vibrometry. *J. Eng. Gas Turbines Power* 132(3), 031603 (8 pages).
- Graebner, J. E., B. P. Barber, P. L. Gammel, D. S. Greywall, and S. Gopani (2000). Dynamic visualization of subangstrom high-frequency surface vibrations. *Appl. Phys. B-Lasers Opt.* 78(2), 1338954 (3 pages).
- Gren, P., K. Tatar, J. Granström, N.-E. Molin, and E. V. Jansson (2006). Laser vibrometry measurements of vibration and sound fields of a bowed violin. *Meas. Sci. Technol.* 17(4), 635–644.

REFERENCES

159

- Hampel, B. and J. Woisetschläger (2006). Frequency- and space-resolved measurement of local density fluctuations in air by laser vibrometry. *Meas. Sci. Technol.* *17*(10), 2835–2842.
- Hardalupas, Y. and M. Orain (2004). Local measurements of the time-dependent heat release rate and equivalence ratio using chemiluminescent emission from a flame. *Combust. Flame* *139*(3), 188–207.
- Hathout, J., M. Fleifil, A. Annaswamy, and A. Ghoniem (2000). Heat-release actuation for control of mixture-inhomogeneity-driven combustion instability. *Proc. Combust. Inst.* *28*(1), 721–730.
- Higgins, B., M. Q. McQuay, F. Lacas, and S. Candel (2001). An experimental study on the effect of pressure and strain rate on CH chemiluminescence of premixed fuel-lean methane/air flames. *Fuel* *80*(11), 1583–1591.
- Higuera, F. (2009). Aerodynamics of a slender axisymmetric bunsen flame with large gas expansion. *Combust. Flame* *156*(5), 1063–1067.
- Howe, M. S. (1998). *Acoustic of Fluid-Structure Interactions*. Cambridge University Press, London.
- Hurle, I. R., R. B. Price, T. M. Sugden, and A. Thomas (1968). Sound Emission from Open Turbulent Premixed Flames. *Proc. Roy. Soc. London Ser. A* *303*, 409–427.
- Hussain, Z. M., A. Z. Sadik, and P. O’Shea (2011). *Digital Signal Processing: An Introduction with MATLAB and Applications*. Springer, Berlin.
- Ibarreta, A. F. and C.-J. Sung (2005). Flame temperature and location measurements of sooting premixed bunsen flames by rainbow schlieren deflectionometry. *Appl. Opt.* *44*(17), 3565–3575.
- Ihme, M., H. Pitsch, and D. Bodony (2009). Radiation of noise in turbulent non-premixed flames. *Proc. Combust. Inst.* *32*(1), 1545–1553.
- Ikeda, Y., J. Kojima, and H. Hashimoto (2002). Local chemiluminescence spectra measurements in a high-pressure laminar methane/air premixed flame. *Proc. Combust. Inst.* *29*(2), 1495–1501.
- Iooss, B., P. Blanc-Benon, and C. Lhuillier (2000). Statistical moments of travel times at second order in isotropic and anisotropic random media. *Waves in Random Media* *10*(3), 381–394.
- Iooss, B., C. Lhuillier, and H. Jeanneau (2002). Numerical simulation of transit-time ultrasonic flowmeters: uncertainties due to flow profile and fluid turbulence. *Ultrasonics* *40*(9), 1009–1015.
- Iqbal, N. and M. H. Salley (2004). *Fire Dynamics Tools (FDTs) Quantitative Fire Hazard Analysis Methods for the U.S. Nuclear Regulatory Commission Fire Protection Inspection Program (NUREG-1805, Final Report)*,

- Chapter Estimating burning characteristics of liquid pool fire, heat release rate, burning duration and flame height. NRC publications, Washington, DC.
- Janssens, M. L. (1991). Measuring rate of heat release by oxygen consumption. *Fire Technol.* 27, 234–249.
- Jeffries, J. B., D. R. Crosley, I. J. Wysong, and G. P. Smith (1991). Laser-induced fluorescence detection of HCO in a low-pressure flame. *Proc. Combust. Inst.* 23(1), 1847–1854.
- Kiameh, P. (2002). *Power Generation Handbook : Selection, Applications, Operation, Maintenance*, Chapter Gas turbine combustor. McGraw-Hill Professional.
- Kim, K., J. Lee, B. Quay, and D. Santavicca (2010). Response of partially premixed flames to acoustic velocity and equivalence ratio perturbations. *Combust. Flame* 157(9), 1731–1744.
- Kizirnis, S. W., R. J. Brecha, B. N. Ganguly, L. P. Goss, , and R. Gupta (1984). Hydroxyl (OH) distributions and temperature profiles in a premixed propane flame obtained by laser deflection techniques. *Appl. Opt.* 23, 3873–3880.
- Klauder, J., A. C. Price, S. Darlington, and W. J. Albersheim (1960). The theory and design of chirp radars. *Bell Sys. Tech. J.* 39(4), 745–808.
- Knikker, R., D. Veynante, and C. Meneveau (2002). A priori testing of a similarity model for large eddy simulations of turbulent premixed combustion. *Proc. Combust. Inst.* 29(2), 2105–2111.
- Köberl, S., F. Fontaneto, F. Giuliani, and J. Woisetschläger (2010). Frequency-resolved interferometric measurement of local density fluctuations for turbulent combustion analysis. *Meas. Sci. Technol.* 21(3), 035302 (10 pages).
- Kojima, J., Y. Ikeda, and T. Nakajima (2000). Spatially resolved measurement of OH*, CH*, and C2* chemiluminescence in the reaction zone of laminar methane/air premixed flames. *Proc. Combust. Inst.* 28(2), 1757–1764.
- Kojima, J. and Q.-V. Nguyen (2005). Quantitative analysis of spectral interference of spontaneous Raman scattering in high-pressure fuel-rich H₂–air combustion. *J. Quant. Spectrosc. Ra.* 94(3-4), 439–466.
- Kokkonen, K. and M. Kaivola (2008). Scanning heterodyne laser interferometer for phase-sensitive absolute-amplitude measurements of surface vibrations. *Appl. Phys. B-Lasers Opt.* 92, 063502 (3 pages).
- Kornilov, V. (2006). *Experimental research of acoustically perturbed bunsen flames*. Ph. D. thesis, Eindhoven University of Technology.

REFERENCES

161

- Kornilov, V., K. Schreel, and L. de Goey (2007). Experimental assessment of the acoustic response of laminar premixed bunsen flames. *Proc. Combust. Inst.* 31(1), 1239–1246.
- Kostiuk, L. and R. Cheng (1994). Imaging of premixed flames in microgravity. *Exp. Fluids* 18(1-2), 59–68.
- Kostiuk, L. W. and R. K. Cheng (1995). The coupling of conical wrinkled laminar flames with gravity. *Combust. Flame* 103(1-2), 27–40.
- Kuo, K. K.-y. (2005). *Principles of Combustion*. Wiley-Interscience, New Jersey.
- Lauer, M. and T. Sattelmayer (2010). On the adequacy of chemiluminescence as a measure for heat release in turbulent flames with mixture gradients. *J. Eng. Gas Turb. Power* 132, 061502 (8 pages).
- Lauer, M., M. Zellhuber, C. Aul, and T. Sattelmayer (2011, June). Determination of the Heat Release Distribution in Turbulent Flames by a Model Based Correction of OH* Chemiluminescence. In *Proceedings of the ASME Turbo Expo 2011*, Number GT2011-45105, Vancouver.
- Ledder, G. and A. Kapila (1991). The response of premixed flames to pressure perturbations. *Combust. Sci. Tech.* 76(1-3), 21–44.
- Lefebvre, A. H. and D. R. Ballal (2010). *Gas turbine combustion: alternative fuels and emissions*. CRC Press, New York.
- Leyko, M., F. Nicoud, and T. Poinsot (2009). Comparison of direct and indirect combustion noise mechanisms in a model combustor. *AIAA journal* 47(11), 2709–2716.
- Lieuwen, T. (2001). Theoretical investigation of unsteady flow interactions with a premixed planar flame. *J. Fluid Mech.* 435, 289–303.
- Lieuwen, T., R. Rajaram, Y. Neumeier, and S. Nair (2002). Measurements of incoherent acoustic wave scattering from turbulent premixed flames. *Proc. Combust. Inst.* 29(2), 1809–1815.
- Lieuwen, T. C. and V. Yang (Eds.) (2005). *Combustion instabilities in gas turbines, Operational experience, Fundamental mechanisms, and Modeling*, Volume 210 of *Progress in Astronautics and Aeronautics*. AIAA, Inc.
- Lintneris, G. and I. Rafferty (2008). Flame size, heat release, and smoke points in materials flammability. *Fire Safety J.* 43(6), 442–450.
- Magre, P. and P. Bouchardy (2000). Nitrogen and hydrogen coherent anti-stokes raman scattering thermometry in a supersonic reactive mixing layer. *Proc. Combust. Inst.* 28(1), 697–703.
- Mahafza, B. R. and A. Z. Elsherbeni (2004). *Matlab Simulations for Radar Systems Design*. Chapman and Hall, New York.

- Mahan, J. and A. Karchemer (1991). *Aeroacoustics of Flight Vehicles: Theory and Practice. Volume 1: Noise Sources*, Volume 1, Chapter Combustion and Core Noise, pp. 483–517. WRDC Technical Report 90-3052.
- Marble, F. and S. Candel (1977). Acoustic disturbance from gas non-uniformities convected through a nozzle. *J. Sound Vib.* 55(2), 225–243.
- Mayrhofer, N. and J. Woisetschläger (2001). Frequency analysis of turbulent compressible flows by laser vibrometry. *Exp. Fluids* 31(2), 153–161.
- McIntosh, A. C. (1991). Pressure disturbances of different length scales interacting with conventional flames. *Combust. Sci. Tech.* 75(4-6), 287–309.
- McIntosh, A. C. and S. A. Wilce (1991). High frequency pressure wave interaction with premixed flames. *Combust. Sci. and Tech.* 79(1-3), 141–155.
- Menkirch, W. (1981). *Fluid Dynamics: Methods in Experimental Physics Part A*, Volume 18, Chapter Density sensitive flow visualization. Academic Press, New York.
- Merrill, S. (2008). *Radar Handbook, 3rd Edition*. McGraw-Hill, New York.
- Miles, R., W. Lempert, and J. Forkey (2001). Laser rayleigh scattering. *Meas. Sci. Technol.* 12(5), 33–51.
- Mirgorodskiĭ, V., V. Gerasimov, and S. Peshin (2008). Correlation of acoustic signals at summary delays. *Acoust. Phys.* 54(6), 869–873.
- Najm, H. N., P. H. Paul, C. J. Mueller, and P. S. Wyckoff (1998). On the adequacy of certain experimental observables as measurements of flame burning rate. *Combust. Flame* 113(3), 312–332.
- Nguyen, Q.-V. and P. H. Paul (1996). The time evolution of a vortex-flame interaction observed via planar imaging of CH and OH. *Proc. Combust. Inst.* 26(1), 357–364.
- Nori, V. N. and J. M. Seitzman (2009). CH* chemiluminescence modeling for combustion diagnostics. *Proc. Combust. Inst.* 32(1), 895–903.
- Oljaca, M., A. Glezer, M. Baffico, and F. Lund (1998). Ultrasound scattering by a swirling jet. *Phys. Fluids* 10(4), 886–898.
- Olsson, E. and K. Tatar (2006). Sound field determination and projection effects using laser vibrometry. *Meas. Sci. Technol.* 17(10), 2843–2851.
- Oppenheim, V. and R. Schafer (1975). *Digital signal processing*. Prentice-Hall.
- Ötügen, M. V. (1997). Uncertainty estimates of turbulent temperature in rayleigh scattering measurements. *Exp. Therm. Fluid Sci.* 15(1), 25–31.
- Palies, P., D. Durox, T. Schuller, and S. Candel (2010). The combined dynamics of swirler and turbulent premixed swirling flames. *Combust. Flame* 157(9), 1698–1717.

REFERENCES

163

- Paul, P. and H. Najm (1998). Planar laser-induced fluorescence imaging of flame heat release rate. *Proc. Combust. Inst.* 27(1), 43–50.
- Peters, N. (2000). *Turbulent Combustion*. Cambridge University Press, London.
- Peters, N. and G. Ludford (1983). The effect of pressure variations on premixed flames. *Combust. Sci. Tech.* 34(1-6), 331–344.
- Petersen, R. E. and H. W. Emmons (1961). Stability of laminar flames. *Phys. Fluids* 4(4), 456–464.
- Poinsot, T. and D. Veynante (2005). *Theoretical and Numerical Combustion*. R.T. Edwards, Inc.
- Poinsot, T. J., A. C. Trouve, D. P. Veynante, S. M. Candel, and E. J. Esposito (1987). Vortex-driven acoustically coupled combustion instabilities. *J. Fluid Mech.* 177, 265–292.
- Poulain, C., N. Mazellier, P. Gervais, Y. Gagne, and C. Baudet (2004). Spectral vorticity and lagrangian velocity measurements in turbulent jets. *Flow Turbul. Combust.* 72(2-4), 245–271.
- Price, R., I. Hurle, and T. Sugden (1969). Optical studies of the generation of noise in turbulent flames. *Proc. Combust. Inst.* 12(1), 1093–1102.
- Qi, J., W. Wong, C. Leung, and D. Yuen (2008). Temperature field measurement of a premixed butane/air slot laminar flame jet with mach-zehnder interferometry. *Appl. Therm. Eng.* 28(14-15), 1806–1812.
- Radkevich, D. B., A. P. Severov, and V. V. Vraitsev (1987). Ultrasonic flowmeter for testing units of large hydroelectric and pumped-storage stations. *Power Tech. Eng.* 21(9), 559–563.
- Rausch, A., A. Fischer, H. Konle, A. Gaertlein, S. Nitsch, K. Knobloch, F. Bake, and I. Röhle (2011). Measurements of Density Pulsations in the Outlet Nozzle of a Combustion Chamber by Rayleigh-Scattering Searching Entropy Waves. *J. Eng. Gas Turb. Power* 133(3), 031601 (9 pages).
- Reuss, D. (1983). Temperature measurements in a radially symmetric flame using holographic interferometry. *Combust. Flame* 49(1-3), 207–219.
- Richecoeur, F., S. Ducruix, P. Scoufflaire, and S. Candel (2009). Effect of temperature fluctuations on high frequency acoustic coupling. *Proc. Combust. Inst.* 32(2), 1663–1670.
- Rorabaugh, C. B. (2011). *Notes on Digital Signal Processing: Practical Recipes for Design, Analysis and Implementation*. Pearson Education, Inc.
- Sadanandan, R., M. Stöhr, and W. Meier (2008). Simultaneous OH-PLIF and PIV measurements in a gas turbine model combustor. *Appl. Phys. B-Lasers Opt.* 90(3-4), 609–618.

- Samaniengo, J., F. Egolfopoulos, and C. Bowman (1995). CO₂* chemiluminescence in premixed flames. *Combust. Sci. and Tech.* 109(1-6), 183–203.
- Schott, W. (2010). Developments in homodyne interferometry. *Key Eng. Mat; Measurement Technology and Intelligent Instruments IX*, 84–88.
- Schuller, T., S. Ducruix, D. Durox, and S. Candel (2002a). Modeling tools for the prediction of premixed flame transfer functions. *Proc. Combust. Inst.* 29(1), 107–113.
- Schuller, T., D. Durox, and S. Candel (2002b). Dynamics of and noise radiated by a perturbed impinging premixed jet flame. *Combust. Flame* 128(1-2), 88–110.
- Schuller, T., D. Durox, and S. Candel (2003). A unified model for the prediction of laminar flame transfer functions: comparisons between conical and v-flame dynamics. *Combust. Flame* 134(1-2), 21–34.
- Searby, G. (2008). *Instability Phenomena during Flame Propagation. Section 5.1 in Combustion phenomena : selected mechanisms of flame formation, propagation, and extinction (ed. J.Jozef et V.Bernard)*. CRC Press, New York.
- Selle, L., L. Benoit, T. Poinso, F. Nicoud, and W. Krebs (2006). Joint use of compressible large-eddy simulation and helmholtz solvers for the analysis of rotating modes in an industrial swirled burner. *Combustion and Flame* 145(1-2), 194–205.
- Settles, G. (2001). *Schlieren and Shadowgraph Techniques: Visualizing Phenomena in Transparent Media*. Springer, Berlin.
- Shakher, C. and A. K. Nirala (1999). A review on refractive index and temperature profile measurements using laser-based interferometric techniques. *Opt. Lasers Eng.* 31(6), 455–491.
- Shung, K. (2005). *Diagnostic Ultrasound: Imaging and Blood Flow Measurements*. CRC Press, New York.
- Sinibaldi, J. O., C. J. Mueller, and J. F. Driscoll (1998). Local flame propagation speeds along wrinkled, unsteady, stretched premixed flames. *Proc. Combust. Inst.* 27(1), 827–832.
- Smith, M. J. T. (2004). *Aircraft Noise (Cambridge Aerospace Series)*. Cambridge University Press, London.
- Stergiopoulos, S. (Ed.) (2000). *Advanced signal processing handbook : theory and implementation for radar, sonar, and medical imaging real-time systems*. CRC Press, New York.
- Stöhr, M., I. Boxx, C. Carter, and W. Meier (2011). Dynamics of lean blowout of a swirl-stabilized flame in a gas turbine model combustor. *Proc. Combust. Inst.* 33(2), 2953–2960.

REFERENCES

165

- Strahle, W. C. (1978). Combustion noise. *Prog. Energ. Combust. Sci.* 4(3), 157–176.
- Sugimoto, T. and Y. Matsui (1982). An experimental study on the dynamic behavior of premixed laminar flames. *Proc. Combust. Inst.* 19(1), 245–250.
- Tanahashi, M., S. Taka, M. Shimura, and T. Miyauchi (2008). CH double-pulsed PLIF measurement in turbulent premixed flame. *Exp. Fluids* 45(2), 323–332.
- Thrane, N., J. Wismer, H. Konstantin-Hansen, and S. Gade (1985). Practical use of the "Hilbert transform". Technical report, Bruel and Kjaer.
- Vagelopoulos, C. M. and J. H. Frank (2005). An experimental and numerical study on the adequacy of CH as a flame marker in premixed methane flames. *Proc. Combust. Inst.* 30(1), 241–249.
- Walsh, K. T., J. Fielding, and M. B. Long (2000, Apr). Effect of light-collection geometry on reconstruction errors in abel inversions. *Opt. Lett.* 25(7), 457–459.
- Wangher, A., G. Searby, and J. Quinard (2008). Experimental investigation of the unsteady response of premixed flame fronts to acoustic pressure waves. *Combust. Flame* 154(1-2), 310–318.
- Wilson, M. (1990). Envelope of correlation used with deconvolution and reconvolution to remove the direct arrival in a multipath environment. Technical Report 17, Naval oceanographic and atmospheric research laboratory.
- Woisetschlager, J., H. Lank, B. Hampel, E. Gottlich, and F. Heitmeir (2003, March). Influence of blade passing on the stator wake in a transonic turbine stage investigated by particle image velocimetry and laser vibrometry. Volume 217, Prague, pp. 1167–1174. Proceedings 5th European Conference on Turbomachinery.
- Xiao, X., C. W. Choi, and I. K. Puri (2000). Temperature measurements in steady two-dimensional partially premixed flames using laser interferometric holography. *Combust. Flame* 120(3), 318–332.
- Xiao, X. and I. K. Puri (2001). Systematic approach based on holographic interferometry measurements to characterize the flame structure of partially premixed flames. *Appl. Opt.* 40(6), 731–740.
- Yu, K. H., A. Trouve, and J. W. Daily (1991). Low-frequency pressure oscillations in a model ramjet combustor. *J. Fluid Mech.* 232, 47–72.
- Zhang, D.-Y. and H.-C. Zhou (2007). Temperature measurement by holographic interferometry for non-premixed ethylene-air flame with a series of state relationships. *Fuel* 86(10-11), 1552–1559.

